ULTRA-LOW PLATINUM AND PLATINUM-FREE FUEL CELLS

A Dissertation

by

MONICA HWANG

Submitted to the Office of Graduate and Professional Studies of
Texas A&M University
in partial fulfillment of the requirements for the degree of

DOCTOR OF PHILOSOPHY

Chair of Committee,	Yossef A. Elabd
Committee Members,	Jodie L. Lutkenhaus
	Micah J. Green
	Jaime C. Grunlan
Head of Department,	M. Nazmul Karim

May 2019

Major Subject: Chemical Engineering

ABSTRACT

Fuel cells are attractive alternative energy sources due to their low-to-moderate operating temperature, zero greenhouse emission, and wide range of applications including automobiles and stationary power sources. However, they have key commercialization disadvantages. Proton exchange membrane fuel cells (PEMFCs) produce high power density but require expensive rare noble metal catalysts (*e.g.*, platinum), which impedes PEMFC commercialization. Alkaline fuel cells (AFCs) are unstable and dangerous due to the use of caustic liquid electrolyte; therefore, solid-state membranes are necessary to promote safe, commercial AFCs. In this study, alternative electrode fabrication techniques and alternative hydrocarbon-based polymers as membranes and ionomers were explored to reduce the overall fuel cell cost for PEMFCs and AFCs.

Ultra-low platinum electrodes fabricated *via* electrospinning/electrospraying (E/E) produced higher PEMFC power density than conventional electrodes and provided insight in the ionomer impact on catalyst particle aggregates. To commercially fabricate E/E electrodes, a needleless electrospinning apparatus was developed in our laboratory. Needleless electrospinning produced proton-conducting nanofibers with higher mechanical and ion transport properties at a higher production rate than needle electrospinning due to multiple higher local polymer concentration sites at the electrospinning surface. Needleless electrospun nanofibers with catalyst particles were employed as ultra-low platinum loading fuel cell electrodes and demonstrated similar power densities as E/E electrodes. These results demonstrate the possibility of producing ultra-low platinum loading E/E electrodes at high production rates.

Commercially available pentablock terpolymers (PTPs) were used as membranes and ionomers in PEMFCs and AFCs. Sulfonated PTPs as membranes and ionomers demonstrated higher conductivity properties and reasonable power densities compared to the commercial fluorinated polymer (Nafion). Brominated and quaternized PTPs with methylpyrrolidinium cations were also developed as solid-state anion exchange membranes and demonstrated promising power densities and durability in AFC applications. Low-platinum E/E electrodes of electrospun PTP nanofibers and electrosprayed catalyst particles demonstrated better platinum utilization than conventional electrodes. The combination of commercial fabrication of ultra-low platinum E/E electrodes and commercially available low-cost ion exchange membranes and ionomers offer an affordable, sustainable, clean energy solution.

DEDICATION

For the people who began this journey with me but were unable to walk with me to the end

For my father who never gave up on me in following my dreams

For my mentor who always encouraged me in pursuing knowledge

ACKNOWLEDGEMENTS

First and foremost, I thank my adviser, Professor Yossef A. Elabd, who was like a firefly on this unfamiliar path. Your endless words of encouragement and steady guidance were the pockets of light along this road that allowed me to persevere and complete this degree in a positive and confident manner. I thank Melissa C. Santos for her mentorship and friendship inside and outside of lab. Without her, the struggles would have been infinitely harder. I thank Rui Sun and Tzu-Ling Chen for keeping me sane with comforting cooking conversations. Their continuous warmth and reassurance dispelled the words of self-doubt in my mind.

I thank all past and present members of the Elabd research group for their feedback on my work. I thank the members of my dissertation committee for taking the time to meet and review my work. I thank Carl Willis and Stacy Shingleton from Kraton Performance Polymers, Inc. for their knowledge and synthesis of the materials for my work. I thank Tom C. Stephens from the Microscopy Imaging Center for training me on the scanning electron microscope.

Lastly, I thank my mother (Hao Chu Hsu), my brother (Wesley Hwang), and my friends (Chris Du, Steven Hang, Richard Hsieh, Brian Hu, Kenny R. Huang, Brenda Jeng, Sami Koo, Matthew Kweon, Tiffany Y. Liu, Edward J. Ruan, and Sally Z. Wang) who came on this journey with me and never stopped supporting me, and to Donovan C. Le, the love of my life, I thank him for his unfaltering love, patience, and support throughout this journey, for I could not imagine the beginning or end without him.

CONTRIBUTORS AND FUNDING SOURCES

Contributors

This work was supervised by a dissertation committee consisting of Professor Yossef A. Elabd, Professor Jodie L. Lutkenhaus, and Professor Micah J. Green of the Department of Chemical Engineering, and Professor Jaime C. Grunlan of the Department of Mechanical Engineering.

The needleless electrospinning apparatus in Chapter 3 was developed with Muizz O. Karenson (Elabd Research Group). The sulfonated pentablock terpolymers in Chapter 5 and pentablock terpolymer precursors in Chapters 6 and 7 were provided by Kraton Performance Polymers, Inc. The brominated and quaternized pentablock terpolymers in Chapters 6 and 7 were prepared by Rui Sun (Elabd Research Group). The electrospinning/electrospraying experiments in Chapter 7 were conducted by Nathan J. Mara (Elabd Research Group).

All other work conducted for the dissertation was completed by the student independently.

Funding Sources

Graduate study was financially supported in part by National Science Foundation under Award Numbers CMMI-1661822 and CBET-1703645 and Kraton Performance Polymers, Inc. Its contents are solely the responsibility of the authors and do not necessarily represent the official views of the National Science Foundation.

The FE-SEM acquisition was supported by the NSF grant DBI-0116835, the VP for Research Office, and the TX Eng. Exp. Station.

TABLE OF CONTENTS

Page

Page

LIST OF FIGURES

Page

Page

Page

Page

Page

Page

LIST OF TABLES

CHAPTER I

INTRODUCTION

Global environmental issues, such as climate change and air pollution, continue to negatively impact the planet due to increasing carbon dioxide emissions. Recent reports by the U.S. Environmental Protection Agency have shown that transportation (*i.e.,* internal combustion engine vehicles) is the second largest contributor for carbon dioxide emissions.[1] To impede the increasing number of internal combustion engine vehicles, renewable energy technology researchers have identified fuel cells as attractive alternative energy sources due to their zero greenhouse emission and promising wide range of applications including automobiles (*e.g.,* Toyota Mirai, Honda Clarity, and Hyundai NEXO) and stationary power sources (*e.g.,* Bloom Energy Energy Saver and Ballard Power ElectraGen Back-Up). Fuel cells are electrochemical devices that directly convert reactant fuel (*e.g.*, hydrogen) into electricity and water as products. Several different types of fuel cells have been explored and developed, including proton exchange membrane, alkaline, phosphoric acid, molten carbonate, and solid oxide. For low-to-moderate operating temperatures (< 200 °C), proton exchange membrane fuel cells (PEMFCs) and alkaline fuel cells (AFCs) are most commonly explored and suitable for vehicle applications.[2] However, both types of fuel cells have key disadvantages that need to be addressed before global fuel cell vehicle commercialization can be achieved to replace internal combustion engine vehicles, and subsequently reduce carbon dioxide emissions.

1.1 Proton Exchange Membrane Fuel Cells

A proton exchange membrane fuel cell (PEMFC), shown in Figure 1.1, converts hydrogen fuel into electricity and water through a series of electrochemical reactions. The electrodes (*i.e.*, anode and cathode) and membrane of the fuel cell constitutes the membrane electrode assembly (MEA), which is the primary driving force in the fuel cell. At the anode, hydrogen oxidizes on platinum and dissociates into protons and electrons (1.1.1). Protons travel through the PEM and electrons are externally carried as electricity. At the cathode, protons and electrons reduce oxygen on platinum to produce water as the only byproduct (CO_2 free) (1.1.2). The half-cell and overall reactions are shown here:

Anode: $2H_2 \rightarrow 4H^+ + 4e^-$ (1.1.1)

Cathode: $O_2 + 4H^+ + 4e^- \rightarrow 2H_2O$ (1.1.2)

Overall: $2H_2 + O_2 \rightarrow 2H_2O$ (1.1.3)

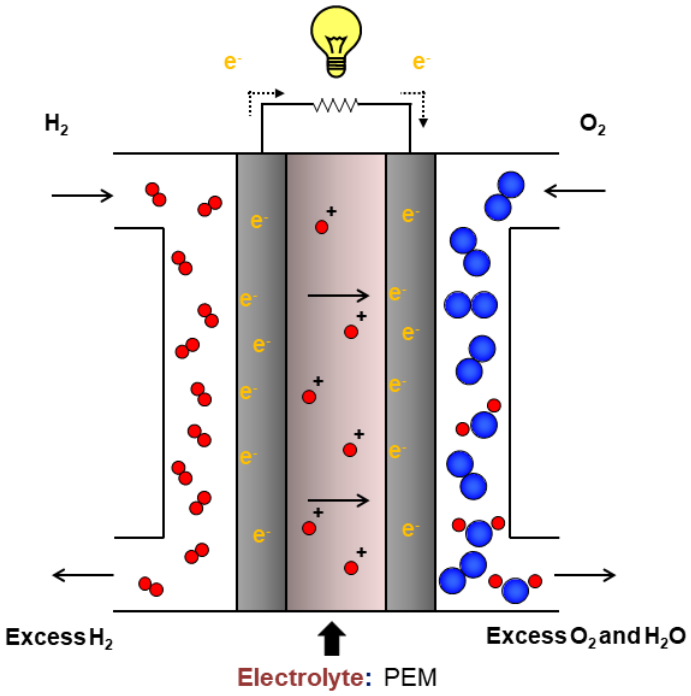

Figure 1.1 Schematic of the proton exchange membrane fuel cell (PEMFC).

PEMFCs can produce high power densities, but require expensive materials that limit their commercialization due to cost. Figure 1.2 shows the fuel cell cost breakdown, revealing that catalyst and membranes constitute 26 – 41% and 9 –17% of the fuel cell cost, depending on the number of fuel cells produced.[3]

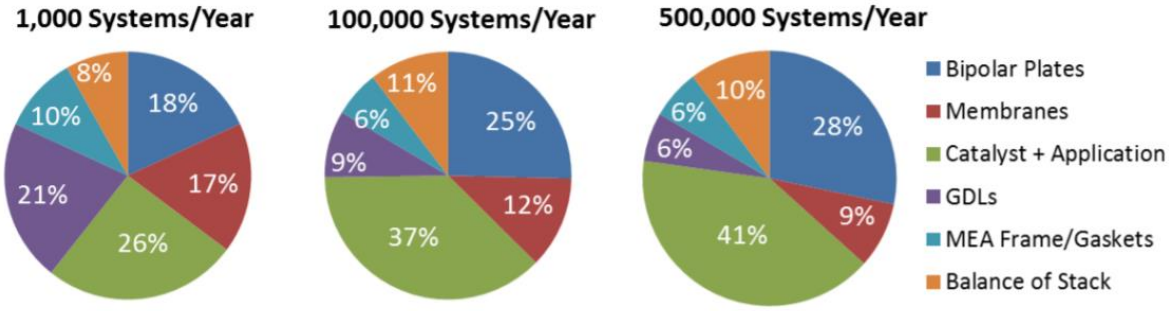

Figure 1.2 Fuel cell stack cost breakdown at 1,000, 100,000, and 500,000 systems per year. Figure reprinted from ref. [[3]].

In order for a fuel cell to operate efficiently, both the activity of the electrochemical reactions and the charge transport (*i.e.*, electron/ion conductivity) must be high to achieve high power density. The catalyst promotes the electrochemical reactions and electron transport within the fuel cell electrodes and the polymer ionomers and membranes promote ion transport within the fuel cell electrodes and membrane separator, respectively. Therefore, rare noble metal catalysts, such as platinum, and commercial perfluorinated sulfonic acid polymers, such as Nafion, are two of the most important and expensive materials in a fuel cell. In order to reduce the cost of the fuel cell, alternative catalyst layer deposition techniques and alternative polymers as ionomers and membranes have been explored by investigating the impact of the catalyst, ionomer, and membrane in reaction kinetics and charge and mass transport within the fuel cell.

1.1.1 Alternative Catalyst Layer Deposition Techniques

Platinum (Pt) is most commonly used in fuel cells as a catalyst to increase the reaction rate of the cathode reaction (*i.e.,* oxygen reduction reaction (ORR)), which is inherently slow in acidic environment (*i.e.,* in PEMFCs). However, current conventional methods of applying the catalyst layer as a fuel cell electrode requires an exorbitant amount of catalyst (typical Pt loadings ~0.4-0.5 mg_{Pt} cm^{-2}) due to poor platinum utilization. Numerous studies have investigated different aspects of the PEMFC (*e.g.,* novel catalysts,[4-5] various operating conditions,[6-8] alternative membranes[9-11]) to improve fuel cell power density at lower Pt loadings (< 0.1 mg_{Pt} cm^{-2}) in order to reduce overall fuel cell cost. However, at lower Pt loadings, typically, there is a significant loss in fuel cell power density due the negative impact on the ORR in the electrode or catalyst layer (*i.e.,* increase in charge and mass transport resistances).

ORR within the fuel cell electrode can only occur at triple phase boundaries (pore-catalyst-ionomer interfaces or junctions),[12] as shown in Figure 1.3, where not only a higher number of these junctions are needed, but also a connected network of all three are also required, *i.e.,* pore network for O_2 transport, catalyst (Pt/C) network for electron transport, and ionomer (Nafion) network for proton transport.[13] Increasing the number and connectivity of triple phase boundaries can have a positive impact on the ORR by reducing both charge and mass transport resistances. Typically, the conventional electrode fabrication technique involves depositing a well-dispersed catalyst slurry solution (Nafion ionomer, Pt/C catalyst, and aqueous alcohol solvent) onto a substrate, typically a gas diffusion layer. After the solvent evaporates, the catalyst particles and ionomer create an intricate porous network, known as the catalyst layer, and allows physical contact between catalyst, ionomer, and pores to form multiple triple phase boundaries.

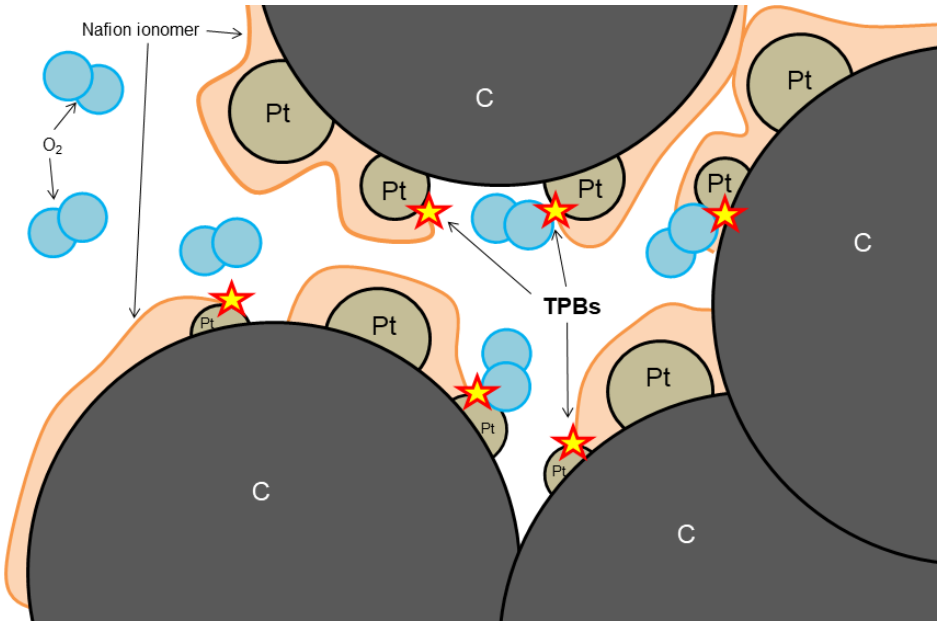

Figure 1.3 Illustration of triple phase boundaries (TPBs; yellow stars) formed due to the porous network of catalyst (Pt/C; brown/gray circles) and ionomer (Nafion; orange), which allows for gas (O_2; blue circles) transport.

The impact of the porous catalyst layer structure on fuel cell performance has been extensively studied with the use of simulation models,[14] different carbon materials,[15] and various solvent compositions.[16-17] Specifically, studies on the effect of the ionomer content in the catalyst layer show that the ionomer content has a simultaneous impact on both the ionomer and pore network.[18-22] Passalacqua *et al.*[19] demonstrated that at low ionomer content, there is a loss of ionomer connectivity and subsequently proton conductivity or transport (*i.e.*, increases charge resistance), which lowers fuel cell performance. At higher ionomer contents, Uchida *et al.*[21] showed that pore volume decreases and blocks O_2 gas from reaching Pt reaction sites (*i.e.*, increases mass transfer resistance), which also lowers fuel cell performance. This finding was later supported by Lee *et al.*,[22] who introduced the concept of the ionomer thin film resistance and reported that at higher ionomer contents, the ionomer thin film thickness increases and prevents O_2 from accessing Pt sites. Therefore, as illustrated in Figure 1.3, there is a balance

between ionomer connectivity and ionomer thin film resistance that limits the maximum power density due to the trade off in resistances in charge transfer (Figure 1.4a) and mass transfer (Figure 1.4b), respectively.

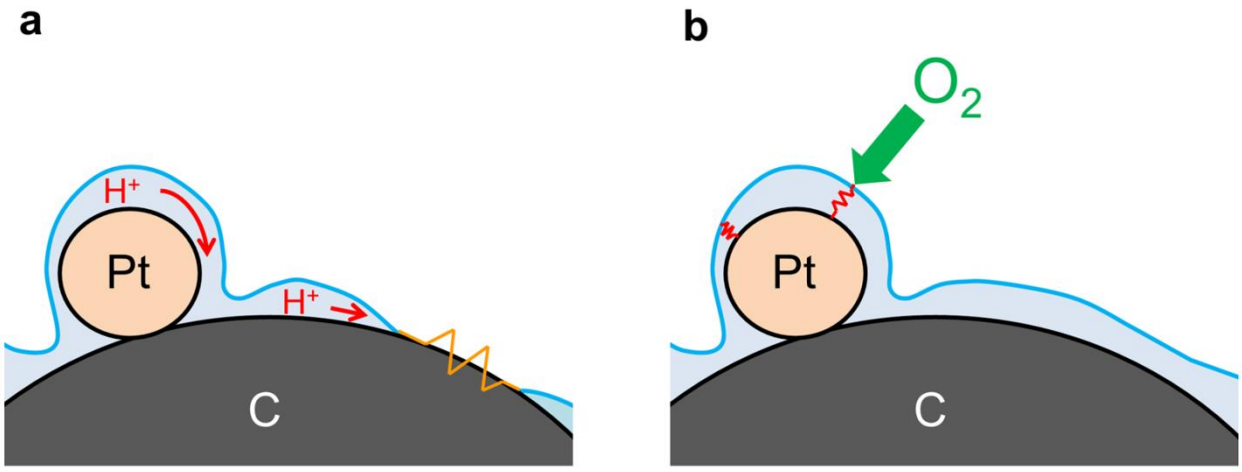

Figure 1.4 Illustration of (a) proton transport resistance due to low Nafion content and (b) mass transport resistance due to Nafion thin film surrounding catalyst particles.

A number of studies have now investigated the role of the Nafion ionomer thin film and its impact on transport resistance and fuel cell performance with both *in situ* and *ex situ* investigations by changing the ionomer content in the catalyst ink solution.[14, 23-36] However, in these studies, the catalyst layer morphology was not constant (*i.e.*, catalyst layer morphology changed with varying ionomer content), regardless of the deposition technique used to apply the catalyst layer. Therefore, it was difficult to design an experiment where catalyst layer morphology and ionomer content (thin film effect) could be investigated exclusively. In other words, to understand the sole ionomer thin film effect on catalyst particles, and subsequently on mass and charge transport, a novel alternative catalyst layer deposition technique must be used.

1.1.2 Alternative Hydrocarbon-based Proton Exchange Membranes

Nafion is a perfluorinated anionic (sulfonic acid) polymer that possesses excellent thermal, mechanical, and chemical stability, along with high water-saturated proton conductivity (*ca.* 0.1 S cm^{-1}). Nafion consists of a poly(tetrafluoroethylene) (PTFE) backbone with sulfonic acid side-chain groups connected *via* perfluorovinylethers, shown in Figure 1.5.

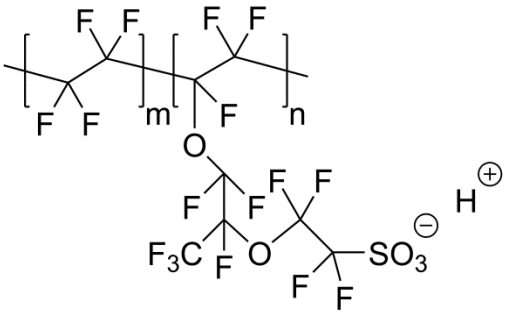

Figure 1.5 Chemical structure of Nafion.

However, Nafion is expensive due to high-cost synthesis and manufacturing processes[37-38] and requires constant humidification (*i.e.,* additional equipment cost) to maintain high proton conductivity.[39-40] The PTFE backbone provides good thermal, mechanical, and chemical stability and the sulfonic acid groups provide high charge density (*i.e.,* high proton conductivity). Proton transport, *i.e.,* conductivity, in Nafion membranes is described by two mechanisms: Grotthuss mechanism and vehicular mechanism, shown in Figure 1.6.[41] Grotthuss, "proton hopping," mechanism occurs when sulfonic acid ion groups and hydronium ions are close enough to allow protons to jump from ion to ion.[42] Vehicular mechanism occurs under fully-hydrated membranes where water becomes a vehicle to shuttle protons.[43] Therefore, water content is critical in the transport of protons in Nafion membranes.

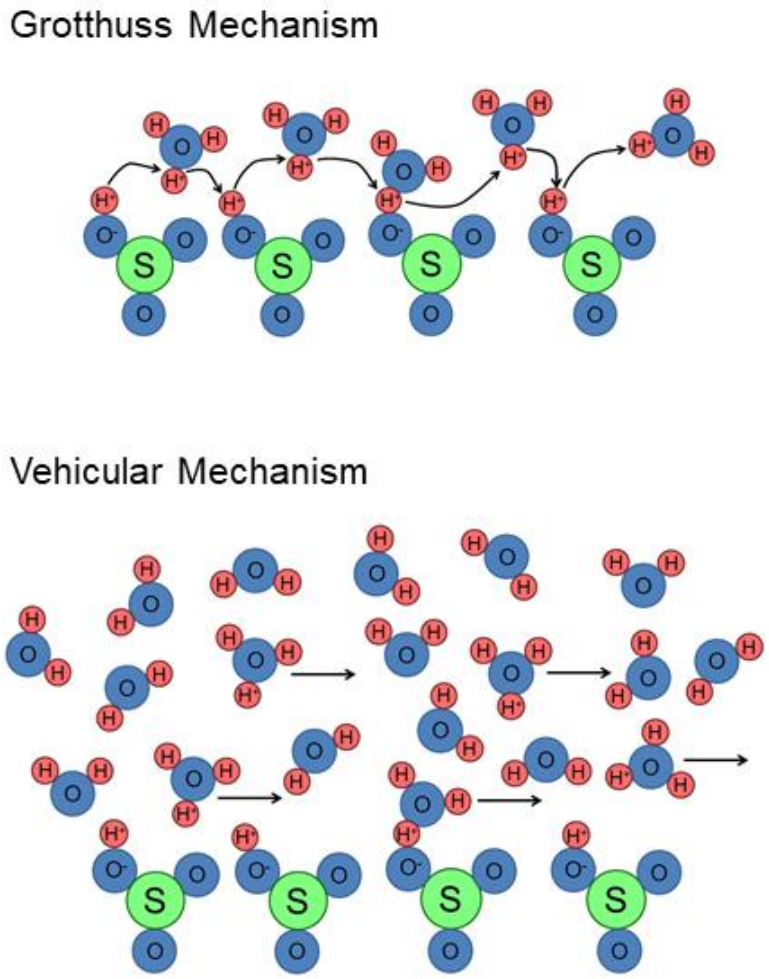

Figure 1.6 Illustration of Grotthuss mechanism (top) and vehicular mechanism (bottom) of proton transport with sulfonic acid groups (green sulfur atoms and blue oxygen atoms) and hydronium ions (blue oxygen atoms and red hydrogen atoms).

Multiple studies have demonstrated that the conductivity of Nafion increases with increasing relative humidity (*i.e.*, increase in water content).[44-46] For example, Cooper *et al.*[44] demonstrated that the proton conductivity of Nafion increased by two orders of magnitude from 20% RH (2.5 x 10^{-3} S cm^{-1}) to 95% RH (1.2 x 10^{-1} S cm^{-1}). Furthermore, Abe *et al.*[47] correlated poor fuel cell performance under low relative humidity to the lack of water transport in the Nafion membrane; therefore, the performance of Nafion membranes are heavily dependent on the water availability

and transport within the fuel cell. However, constant humidification of the fuel cell requires additional equipment, which increases the overall cost of the fuel cell module. Thus, there is significant motivation in developing low-cost, highly proton conductive water-independent membranes.[48] These numerous studies on Nafion provided valuable knowledge of the limitations of Nafion and required improvements for fuel cell applications, creating a base of desired properties for alternative polymer designs.

Hydrocarbon-based polymers are attractive due to their commercial availability and flexibility in molecular design and synthesis.[49] Specifically, polymers with aromatic groups have high thermal stability and good chemical stability in acidic media, making them favorable in PEMFC applications.[38] Therefore, different aromatic hydrocarbon polymer designs have been explored such as poly(ether ketones),[50-54] poly(sulfones),[55-59] and poly(phenylenes)[54, 60] to develop a polymer that has good thermal, mechanical, chemical, and proton transport properties at lower relative humidity. Parnian *et al.*[53] demonstrated that sulfonated poly(ether ether ketone) (SPEEK) can have similar proton conductivity to Nafion under 60% relative humidity, suggesting SPEEK to be a promising proton exchange membrane. Nguyen *et al.*[52] grafted dual sulfonated 3,3-diphenylpropylamine (SDPA) onto poly(arylene ether ketone) (PAEK), which achieved higher fuel cell performance than Nafion, suggesting that PAEK-SDPA is a suitable alternative to the Nafion membrane. Recently, Lee *et al.*[58] synthesized a series of sulfonated poly(ether sulfone) copolymers that performed similarly to Nafion under high relative humidity (80% RH) and surpassed Nafion under low relative humidity (53% RH). These findings demonstrate promising hydrocarbon-based polymer membranes as alternatives to Nafion. Examples of hydrocarbon-based polymers and Nafion and their maximum power densities are shown in Table 1.1.

Table 1.1 Examples of PEMFC performances of sulfonated hydrocarbon polymers as PEMs with state-of-the-art Nafion as comparison.

Max power density (W cm^{-2})	Fuel cell conditions	Polymer	Ref.
1.42[a]	H_2/O_2, 80 °C, 100% RH	Nafion	[61]
1.18	H_2/O_2, 80 °C, 100% RH	SPSSF	[59]
1.16	H_2/O_2, 80 °C, 100% RH	SPAEK	[62]
1.10	H_2/air, 80 °C, 100% RH	sPPm-b-PAES-22	[63]
0.80	H_2/O_2, 80 °C, 100% RH	SPEEK-51	[51]
0.57	H_2/air, 80 °C, 50% RH	COMB-7	[64]
0.56	H_2/O_2, 80 °C, 100% RH	SPAEK-SDPA	[52]
0.46[a]	H_2/O_2, 80 °C, 80% RH	S4PH-35-PS	[58]

[a]Measured under back pressure.

Although some of these hydrocarbon-based polymers demonstrate comparable fuel cell performances to Nafion, perfluorinated sulfonic acid polymers (*e.g.,* Nafion) continues to be the leading commercial state-of-the-art PEM. Therefore, further investigation of hydrocarbon-based polymer designs that can be commercialized or are commercially available are required to find a translational alternative to fluorinated polymers.

1.2 Alkaline Fuel Cells

To address the expensive use of Pt in fuel cells, there is motivation to investigate alkaline fuel cells (AFCs) as an alternative to PEMFCs, due to faster oxygen reduction reaction kinetics in alkaline environments. AFCs can achieve high power densities with non-noble catalysts, such as silver (Ag) and nickel (Ni), which make them an attractive alternative to PEMFCs. An AFC,

shown in Figure 1.6, converts hydrogen fuel into electricity and water through a series of electrochemical reactions. Similar to PEMFCs, electrodes (*i.e.*, anode and cathode) and a liquid electrolyte (typically potassium hydroxide solution) constitute the primary driving force of the fuel cell. At the anode, hydrogen oxidizes with hydroxide ions to produce water and electrons (1.2.1). Electrons are externally carried as electricity, and reduce water and oxygen to produce hydroxide ions at the cathode (1.2.2). Hydroxide ions are then carried through the electrolyte from the cathode to the anode. The half-cell and overall reactions are shown here:

Anode: $2H_2 + 4OH^- \rightarrow 2H_2O + 4e^-$ (1.2.1)

Cathode: $O_2 + 2H_2O + 4e^- \rightarrow 4OH^-$ (1.2.2)

Overall: $2H_2 + O_2 \rightarrow 2H_2O$ (1.2.3)

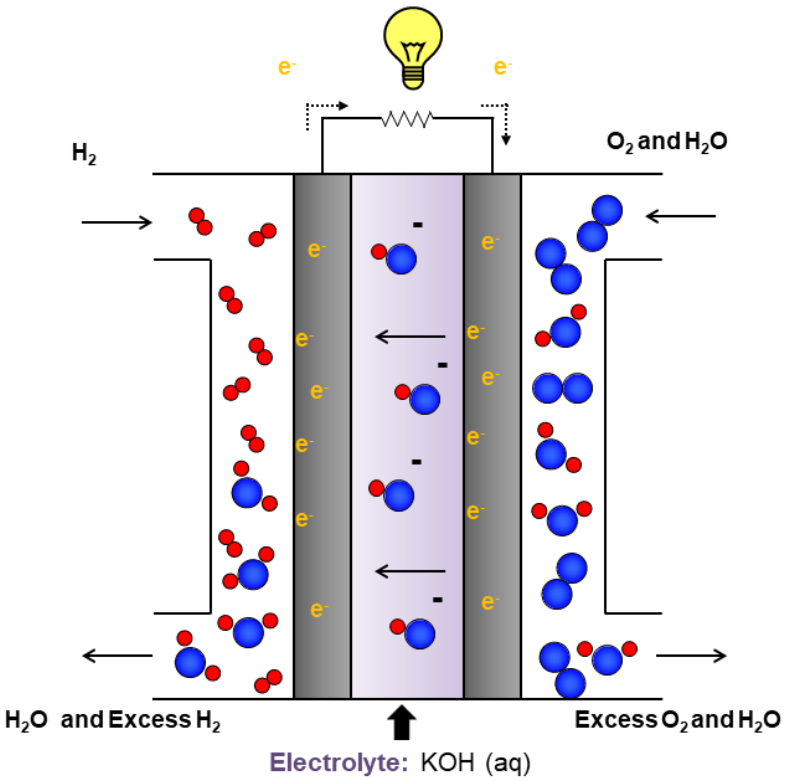

Figure 1.7 Schematic of the alkaline fuel cell (AFC).

However, AFCs are problematic due to the use of caustic liquid electrolytes, which are not stable when exposed to carbon dioxide.[65] Due to the mobile cations (*e.g.*, potassium) in solution, potassium carbonates can precipitate in the form of solid crystals in the presence of carbon dioxide and physically block porous electrodes, inhibiting gas transport and decreasing fuel cell performance and lifetime. By replacing the liquid electrolyte with a solid electrolyte membrane (*i.e.*, no free cations), precipitates will not form. Therefore, solid-state ion conductive membranes (*e.g.*, anion exchange membranes) are desirable to replace the liquid electrolyte.

1.2.1 Anion Exchange Membrane Alkaline Stability

Anion exchange membranes (AEMs) are similar to PEMs in terms of desired properties (*e.g.*, electron insulator and ionic conductor). In addition, AEMs need good mechanical strength (*i.e.*, limited swelling in water), good chemical stability in highly basic environments (*i.e.*, alkaline stability), and high ionic conductivity (*i.e.*, hydroxide ion transport).[66] Recently, several investigators have developed and characterized new polymer materials, such as graft polymers[67-69] and random copolymers,[70-72] as AEMs to meet these requirements, focusing on alkaline stability and conductivity. The development of AEMs has recently centered around different polymer backbones, such as poly(phenylene)[72-75] and poly(ethylene-*co*-tetrafluoroethylene)[67-68, 76] and different cations, such as phosphonium[77-80] and quaternary ammonium,[71-72, 76, 81-82] creating multiple combinations of polymer backbones and cations. Hibbs *et al.*[73] synthesized a poly(phenylene)-based polymer with a quaternary ammonium cation that demonstrated a hydroxide ion conductivity of 50 mS cm^{-1} and no loss in ion-exchange capacity (*i.e.*, ion charge densities) after 4 weeks under 4 M sodium hydroxide solution at 60 °C, suggesting

poly(phenylene)-based polymers could be stable under elevated temperate high alkaline environments. Wang *et al.*[83] demonstrated a stability of < 2% loss in ion-exchange capacity of a radiation-grafted poly(ethylene-*co*-tetrafluoroethylene) quaternary ammonium membrane after exposure to 1 M sodium hydroxide solution for 1 week, suggesting that ETFE-based polymers could be durable in AFC applications. Quaternary ammonium is the most commonly studied cation for designing and developing polymers as AEMs. However, Meek and Elabd[84] demonstrated that polymers with alternative cations, such as imidazolium and pyrrolidinium, have better alkaline stability than the ubiquitous quaternary ammonium cation, suggesting that other cation-based polymers could perform better as AEMs. Therefore, there is significant motivation in investigating the stability and performance of alternative cation-based polymers, changing the paradigm of quaternary ammonium cation-based polymers.

1.2.2 Anion Exchange Membrane Fuel Cell Lifetime Stability

There are multiple studies on the long-term *ex situ* stability of AEMs (*i.e.,* in potassium hydroxide solution), but few reports on the long-term *in situ* stability of AEMs (*i.e.,* in AFCs). A recent review by Dekel[85] summarizes the anion exchange membrane fuel cell (AEMFC) performance stability data in literature since early 2000. Including the most recent publications with AEMFC stability results, there is only a handful of publications (< 20) that investigates and discusses AEMFC performance stability and degradation. These studies are summarized in Table 1.2.

Table 1.2 Summary of AEMFC stability performance. Adapted from ref. [85].

Stability test duration (h)	Decay rate[a] (mV h^{-1})	Total Pt loading (mg_{Pt} cm^{-2})	Ionomer	Membrane	Ref.
24.2	8.3	0.8	AS-4	PVAc/OH	86
26	12.3	0.8	QPMBV	QPMBV-1	87
63	2.5	1.0-1.2	comb-shaped PPO	comb-shaped PPO	74
70	N/A	0.8	ETFE-TMA	ETFE-TMA	88
70	N/A	0.8	ETFE-MPRD	ETFE-MPRD	88
80	N/A	3	NF-PAES	NF-PAES	82
100	1.1	0.5	DAPSF/TAPSF	A901	89
100	1.6	0.8	AS-4	PBI-c-PVBC/OH	90
125	1.3	0.8	QAPPT	QAPPT-OH	91
140	N/A	0.8	SION1	QPPT-35	92
232	0.9	0.8	AS-4	TPPVBN30	93
300	N/A	3	ATM-PP	ATM-PP	82
320	1.2	0.45	Acta I2	N/A	94
360	2	1	cross-linked PVBC-PS	A201	95
400	N/A	0.9	Acta I2	N/A	94
575	0.6	1	QASEBS	DAPSF/TAPSF	96

[a]Measured using the initial (t = 0 h) and final voltage of the stability test

Standard procedures for measuring stability include using a constant voltage procedure (*i.e.*, potentiostatic) over a specified amount of time or sweeping voltage or current density (*i.e.*, polarization curves) at different times points; however, most stability studies use a constant current density procedure (*i.e.*, galvanostatic) and measures the corresponding cell voltage over a specified amount of time. Luo *et al.*[87] synthesized poly((methyl methacrylate)-*co*-(butyl acrylate)-*co*-(vinylbenzyl chloride)) with quaternary ammonium cation at three different vinylbenzyl chloride content and demonstrated that the polymer with the smallest vinylbenzyl chloride content is the most durable under fuel cell operation at 100 mA cm^{-2} for at least 26 h and a voltage decay rate of 12.3 mV h^{-1} due to better mechanical properties (*i.e.*, less water uptake). Peng *et al.*[91] synthesized a poly(*N*-methyl-piperidine-*co*-*p*-terphenyl) with a quaternary ammonium cation in the piperidine group (QAPPT), which had a high conductivity (137 mS cm^{-1}) and low in-plane swelling ratio (9.5%). The QAPPT was used as the membrane and ionomer in the MEA and demonstrated fuel cell operation for 125 h under 200 mA cm^{-2} with a voltage decay rate of 1.3 mV h^{-1}, suggesting that QAPPT is relatively stable under standard fuel cell operating conditions (*e.g.*, 80°C, 100% RH) compared to other literature (see Table 1.2). Gao *et al.*[96] conducted the longest AEMFC stability test of 575 h under fuel cell operation of 100 mA cm^{-2} with a voltage decay rate of 0.6 mV h^{-1} using a combination of a crosslinked biopolymer and terpolymer composite with a quaternary ammonium cation as the membrane and poly(styrene-ethylene/butylene-styrene) (SEBS) with a quaternary ammonium cation as the ionomer, suggesting that SEBS is an effective ionomer in AFC operation. Although these studies demonstrate that the *in operando* stability of AEMs have significantly improved over the last two decades, the stability needs to be further improved to be on par with PEMFCs (1-2 μV h^{-1} at 75 °C and close to 100% RH).[97] Also, most of these AEMFC lifetime stability studies use the

standard quaternary ammonium cation; thus, there is a lack of information and research on the stability of other cations as membranes in AFCs. Moreover, there are few studies investigating the impact of these new cation-based polymer materials as ionomers in AFCs. Therefore, further investigation of these alternative cation-based polymer materials as membranes and ionomers in AFCs are required to determine their future as commercial AEMs and ionomers for AFC applications.

1.3 Outline and Summary

In this study, PEMFCs and AFCs are investigated to reduce the overall cost of fuel cells by reducing the amount of platinum (*i.e.,* improving platinum utilization) in PEMFCs and investigating low-cost commercially available non-fluorinated polymers as membranes and ionomers in PEMFCs and AFCs.

Chapter II employs electrospinning/electrospraying (E/E) as an alternative catalyst layer deposition technique to improve platinum utilization (high power densities at ultra-low platinum loadings) and studying the effect of ionomer content on mass and charge transfer resistances in the catalyst layer. Previous studies utilizing the E/E technique demonstrated promising results for high platinum utilization, but did not explore the fundamentals of transport resistances in the catalyst layer and subsequently optimize the design of future ultra-low platinum electrodes. Chapter III utilizes a needleless electrospinning technique to create Nafion nanofibers with an aim to increase the production rate the E/E technique in Chapter II. The limits in Nafion purity, nanofiber mat properties, and electrospinning operating parameters using this needleless electrospinning technique with Nafion solutions are explored. Chapter IV applies a nanofiber-nanoparticle catalyst layer that consists of Nafion nanofibers fabricated using needleless

electrospinning and catalyst particles deposited using needle electrospraying as fuel cell electrodes. Chapter V prepares a commercially available non-fluorinated sulfonated pentablock terpolymer as a PEM and ionomer and compares its properties and fuel cell performance to the commercial Nafion under different relative humidities. In addition, the effect of ionomer content and solvent content in the electrodes on fuel cell performance is also studied.

To achieve a platinum-free fuel cell, Chapter VI investigates AFCs using pentablock terpolymers (PTPs) with methylpyrrolidinium cations and hydroxide anions as AEMs and ionomers. In addition, the effect of the ionomer content and solvent content in the electrodes and varying fuel cell operating conditions is also examined. Chapter VII implements the E/E technique in Chapter II and the PTP in Chapter VI to create novel PTP nanofiber/catalyst particle E/E electrodes for AFCs.

Chapter VIII concludes with a summary of the contributions of this research towards a commercial, sustainable energy society using ultra-low platinum and platinum-free fuel cells, using novel catalyst layer deposition techniques and unique commercially available non-fluorinated polymers, as well as proposed directions for future work.

CHAPTER II

IMPACT OF IONOMER RESISTANCE IN NANOFIBER-NANOPARTICLE ELECTRODES FOR ULTRA-LOW PLATINUM FUEL CELLS*

2.1 Introduction

A number of studies have investigated the role of the Nafion ionomer thin film and its impact on transport resistance and fuel cell performance with both *in situ* and *ex situ* investigations.[14, 23-36] However, few studies provide insight on the role of transport resistances on fuel cell performance at low Pt loadings.[98-99] Greszler *et al.*[99] investigated the influence of Pt loading on oxygen transport resistance using limiting current density experiments and observed that fuel cell performance loss was significant at low Pt loadings. Owejan *et al.*[98] reported that fuel cells with ultra-low Pt loadings ($\leq$ 0.05 mg_{Pt} cm^{-2}) experienced significant transport losses and subsequently fuel cell performance losses and demonstrated that transport resistance is a strong function of the surface area and dispersion of particles (catalyst layer morphology). Both studies employed carbon as a filler to maintain similar porous catalyst layer morphologies and electrode thicknesses under different Pt loadings in order to investigate the ionomer thin film resistance. However, in these studies, the overall distribution of Pt catalyst differed due to the additional carbon (*i.e.*, catalyst layer morphology was not constant) and therefore it was difficult to design an experiment where catalyst layer morphology and ionomer content (thin film effect) could be investigated independent of one another or exclusively. In other words, an experiment where the catalyst layer morphology is held constant, while ionomer content changes with the goal of

*Reprinted with permission from "Impact of ionomer resistance in nanofiber-nanoparticle electrodes for ultra-low platinum fuel cells" by M. Hwang and Y.A. Elabd, 2019. *International Journal of Hydrogen Energy.* 44, 6245-6256, Copyright 2019 by Elsevier.

exploring the impact of transport resistances on fuel cell performance absent of changes in the catalyst layer morphology at low Pt catalyst loadings. Other studies have investigated alternative catalyst layer deposition techniques, such as pulse electrodeposition,[100] magnetron sputter deposition,[101] electrospraying,[102-103] electrospinning,[104-106] screen printing,[107] and inkjet printing.[108] However, regardless of the deposition technique, changing the ionomer content in the catalyst layer affects not only the amount of ionomer that surrounds the catalyst particles, but also the overall morphology of the catalyst layer.

Recently, in our laboratory, a new simultaneous electrospinning and electrospraying (E/E) process, shown in Figure 2.1, was developed to produce unique nanofiber-nanoparticle electrodes for PEMFCs that resulted in high power densities at ultra-low Pt loadings.[61, 109] The E/E technique allows for fabrication of similar catalyst layer morphology while changing other properties (*e.g.*, ionomer content, fiber composition, *etc.*), which is difficult to achieve with other catalyst layer deposition techniques, as previously explained. The simultaneous execution of electrospraying and electrospinning increases the number and connectivity of triple phase boundaries by creating a connected network of pores, proton conductive Nafion nanofibers, and electron conductive Pt/C nanoparticles, which differs from conventional electrodes. Here, in this work, E/E electrodes, at various Nafion contents in the electrospraying solution, were fabricated to investigate the impact of Nafion content on catalyst layer transport resistances and fuel cell power density at ultra-low Pt loadings (*ca*. 0.05 mg_{Pt} cm^{-2}). Therefore, this study allows for the exclusive investigation of the effect transport resistances on fuel cell performances at different ionomer contents (thin film effect) at a constant catalyst layer morphology, unlike conventional electrodes.

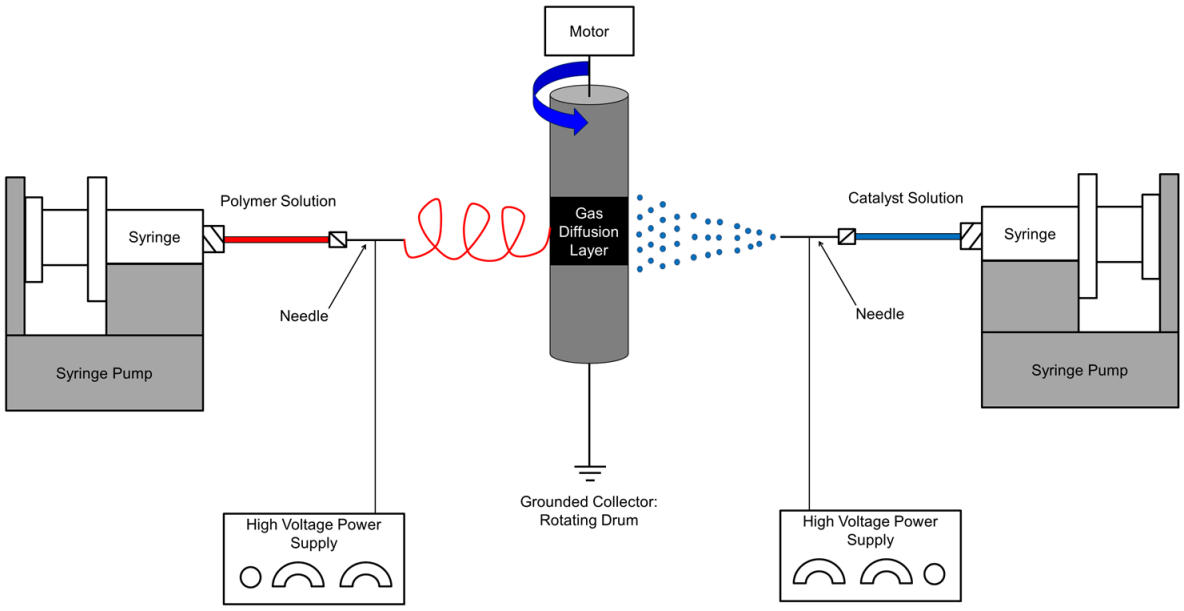

Figure 2.1 Schematic of the electrospinning/electrospraying (E/E) apparatus.

2.2 Experimental Methods

2.2.1 Materials

Isopropanol (IPA; ACS reagent, ≥ 99.5%) and poly(acrylic acid) (PAA; M_V = 450,000 g mol^{-1}) were purchased from Sigma-Aldrich. Carbon (Vulcan XC-72) and 20 wt% platinum on carbon (Pt/C; Vulcan XC-72) were purchased from Premetek Co. 1100 EW Nafion solution (5 wt% in 3/1 v/v isopropanol/water) and Nafion membrane (NR-212, 1100 EW (0.91 meq g^{-1}), 0.002 in (~51 µm) dry thickness) were purchased from Ion Power. Gas diffusion layer (GDL; Sigracet 25BC) was purchased from Fuel Cells Etc. All materials were used as received. Deionized (DI) water with a resistivity of 16 MΩ cm was used as appropriate. Ultra-high purity grade nitrogen was purchased from Brazos Valley Welding Supply. Ultra-high purity grade oxygen and ultra-

zero grade air were purchased from Airgas. Ultra-high purity grade hydrogen was purchased from Praxair. All gases were used for all fuel cell experiments.

2.2.2 Two-Needle Electrospinning/Electrospraying (E/E) Apparatus

A custom-designed E/E apparatus, as illustrated in Figure 2.1, consists of two high-voltage power supplies (PS/EL50R00.8, Glassman High Voltage, Inc. and ES40P-10W/DAM, Gamma High Voltage Research, Inc.), two syringe pumps (NE-1000, New Era Pump Systems), two glass syringes (Pt. No. CG-3070-03, Chemglass Life Sciences), two syringe needles (i.d. = 0.024 in. (0.603 mm), Hamilton), poly(vinyl chloride) tubing (Pt. No. 30600-65 and 30600-66, Cole-Parmer), and a grounded collector (cylindrical drum covered with aluminum foil, o.d. = 4.85 cm) connected to a motor (4IK25GN-SW2, Oriental Motor) to rotate the drum at 135 rpm during the E/E process. Four GDLs (*ca*. 2 cm × 2 cm) were adhered to the drum, where catalyst nanoparticles and polymer nanofibers were electrosprayed and electrospun simultaneously onto the GDLs *via* the E/E process. The needle tip to collector distances, applied voltages, and solution flow rates were 15 and 9 cm, 10 and 12 kV, and 0.3 and 3.3 mL h^{-1} for the electrospinning and electrospraying processes, respectively.

2.2.3 Electrode and Membrane Electrode Assembly (MEA) Fabrication

The electrospraying catalyst ink solution used to fabricate E/E electrodes consisted of a base mixture of 20 mg of Pt/C catalyst, ~1 – 2 mg of bare carbon, 250 mg of DI water, Nafion solution and isopropanol. The particle sizes can vary due to the solids weight percent of the electrospraying solution, thus the solids weight percent was kept constant at 1 wt% for all E/E experiments by adjusting the amount of isopropanol in the mixture. The amount of Nafion

solution was adjusted to achieve different amounts of Nafion content of the solids in the electrospraying ink solution as detailed in Table 2.1. The resulting mixture was sonicated for 3 min at 35% amplitude (Q125, Qsonica) prior to electrospraying. The electrospinning polymer solution used to fabricate E/E electrodes was a 5 wt% 4/1 Nafion/PAA polymer solution, *e.g.*, 25 mg of PAA, 2000 mg of Nafion solution, and 485 mg of 3/1 v/v isopropanol/water solution. The solution was stirred under ambient temperature for at least 12 h to ensure complete dissolution of PAA prior to electrospinning. The catalyst ink solution and the polymer solution were used in the electrospraying and electrospinning processes, respectively, to fabricate E/E electrodes as described in the previous section, and the Pt loading was controlled by the duration of the E/E process. Conventional (control) electrodes were prepared by mixing 100 mg of Pt/C catalyst, 550 mg of DI water, 1000 mg of Nafion solution, and 1350 mg of isopropanol, which corresponds to 2/1 w/w (Pt/C)/Nafion in 3/1 v/v isopropanol/water. The mixture was sonicated for 3 min at 35% amplitude and subsequently brushed onto the GDL with an ox hair brush (0689-00025, Gordon Brush Mfg. Co., Inc.). This process was repeated to achieve the target Pt loading of 0.10 mg_{Pt} cm^{-2}. Membrane electrode assemblies (MEAs) were fabricated by placing the Nafion NR-212 membrane in between two catalyst-coated GDLs (anode and cathode) and heat pressing (3851-0, Carver) for 5 min at 275 °F (135 °C) and 3200 psi (22 MPa). Two MEAs with six different Nafion contents were fabricated for a total of twelve E/E MEAs in this study.

2.2.4 Electrode Characterization

The morphology of the E/E electrodes was investigated with scanning electron microscopy (SEM; FEI Quanta 600 FE-SEM, 10 kV for X 5000 magnifications images and 20 kV for X 100000 magnification images) using a working distance of 10 mm. Samples were sputter coated

(Cressington 208 HR) with platinum/palladium (6 nm thickness) prior to SEM analysis. For each image, the diameters of 20 nanofibers and 20 nanoparticles were randomly selected and measured using ImageJ software for each electrode sample.

The Pt loading was measured with thermal gravimetric analysis (TGA; Q50, TA Instrument). A small portion of the electrode (*ca*. 4–6 mg) was heated in the TGA from ambient temperature to 900 °C at 10 °C min^{-1} in air at 60 mL min^{-1}. Since all components in the E/E electrode degrade below 800 °C with the exception of Pt, the Pt loading was determined by dividing the residual weight at 850 °C by the original area of the TGA sample. The average Pt loading for each E/E experiment was determined using 2–4 samples.

2.2.5 Fuel Cell Tests and Cyclic Voltammetry (CV)

Each MEA (1.21 cm^2 area) was placed between two serpentine flow field graphite plates (1 cm^2 flow area) separated by two 0.152 mm thick PTFE/fiberglass gaskets (Cat. No. 33, Scribner Associates, Inc.). The entire fuel cell assembly consisted of an MEA, two gaskets, and two flow plates placed between copper current collectors followed by endplates all held together by bolts with 100 lb in (11.3 N m) of applied torque. Fuel cell performance of each MEA was evaluated with a fuel cell test station (850C, Scribner Associates, Inc.). Fuel cell tests were conducted under ambient pressure with saturated (100% RH) anode and cathode flow rates of 0.43 L min^{-1} hydrogen and 1.02 L min^{-1} oxygen or air, respectively. The stoichiometry of the anode and cathode flow rates used for the fuel cell testing is approximately 1:2 for hydrogen/oxygen and 1:2 for hydrogen/air. The cathode gas, anode gas, and cell temperatures were all maintained at 80 °C. Fuel cell performance was recorded after a new MEA was fully activated. The activation process consists of operating the MEA at 0.7 V for 1 h, followed by 0.6 V, 0.4 V, and 0.2 V for

30 min at each voltage, and ending with two cycles of 0.6 V and 0.4 V for 30 min at each voltage. Polarization curves (cell voltage *versus* current density) were collected from open circuit voltage (OCV) to 0.2 V at increments of 0.05 V min^{-1} to determine that no further increase in current density at a constant voltage was observed, thus the MEA was at steady state. After the MEA was fully activated and reached steady state, five polarization curves were taken to determine the average maximum power density. The average error between polarization curves was < 3% and < 5% for the hydrogen/oxygen and hydrogen/air experiments, respectively.

Cyclic voltammetry (CV) was performed on a fully activated MEA with a potentiostat (Solartron SI 1287A, Corrware Software) at 20 mV s^{-1} from 0.01 V to 1 V *versus* NHE under ambient pressure. In this two-electrode configuration, the anode serves as both the counter and reference electrodes. The fuel cell anode and cathode were supplied with 0.04 L min^{-1} hydrogen and 0.02 L min^{-1} nitrogen, respectively. Temperatures of the cathode gas, anode gas, and cell were maintained at 30 °C. The Pt catalyst was assumed to have an average site density of 210 µC cm^{-2}.[110] The electrochemical surface area (ECSA) was determined from the hydrogen adsorption area from 0.12 to 0.30 V of the CV data. Five cycles were taken to determine the average ECSA for each MEA. Linear sweep voltammetry was performed at 2 mV s^{-1} from OCV to 0.8 V *versus* NHE to determine if the MEA had any defects that resulted from internal shorts or significant hydrogen crossover.

2.2.6 Electrochemical Impedance Spectroscopy (EIS)

Electrochemical impedance spectroscopy (EIS; Solartron SI 1260A) was performed on a fully activated MEA from 1 MHz to 1 Hz at -0.4 V versus OCV (*ca.* 0.49 - 0.55 V *versus* NHE) under ambient pressure. In this two-electrode configuration, the anode serves as both the counter and

reference electrodes. The fuel cell anode and cathode were supplied with 0.43 L min^{-1} hydrogen and 1.02 L min^{-1} oxygen, respectively. Temperatures of the cathode gas, anode gas, and cell were all maintained at 80 °C. The EIS data was analyzed using a common equivalent circuit model that consisted of a resistor (resistance of the solid electrolyte membrane) in series with a parallel circuit of a constant phase element and a second resistor (resistance of the catalyst layer) that is typically used to describe a porous electrode.[111] The catalyst layer resistance values reported here are the polarization resistances.

2.3 Results and Discussion

Fuel cell experiments with E/E catalyst layer electrodes with different Nafion contents (Table 2.1) were conducted to investigate the effect of the Nafion content on catalyst layer resistances and subsequently on fuel cell performance at a fixed catalyst layer morphology. SEM images of the E/E catalyst layers are shown in Figure 2.2a–f, where each image corresponds to different amounts of Nafion (wt% solids) in the electrospraying solution. The E/E catalyst layers show a highly porous network of randomly arranged nanofibers and particle aggregates, which promotes facile gas transport to Pt sites for reactions to occur. The particle-fiber-pore junction points (*i.e.*, triple phase boundary points) also provide intimate interactions for electron transport, proton transport, and ORR without loss of oxygen gas transport due to the highly porous network as shown in previous studies.[61, 109] Figure 2.3 shows the average fiber diameters and particle diameters of the images shown in Figure 2.2a–f. The average fiber diameters range from 137 ± 48 nm to 183 ± 64 nm and the average particle diameters range from 1.27 ± 0.71 μm to 1.59 ± 1.34 μm, indicating that the nanofiber sizes and particle aggregate sizes are similar for all E/E experiments regardless of the amount of Nafion content in the electrospraying solution. The fiber

diameter size distributions and particle aggregate size distributions are also similar for all E/E experiments. This result highlights the ability of the E/E process to create catalyst layers with similar overall morphology at different catalyst-to-ionomer ratios or ionomer contents. Thus, the impact of transport resistances due to the ionomer surrounding catalyst particles can be solely investigated without other parameters changing simultaneously.

Table 2.1 Nafion content of the solids in 1 wt% electrospraying solution.

Nafion content in solids (wt %)	**Nafion solution (mg)**	**Isopropanol (mg)**
0	0	1857
19	101	2338
32	200	2704
48	395	3425
65	805	5043
79	1601	8222

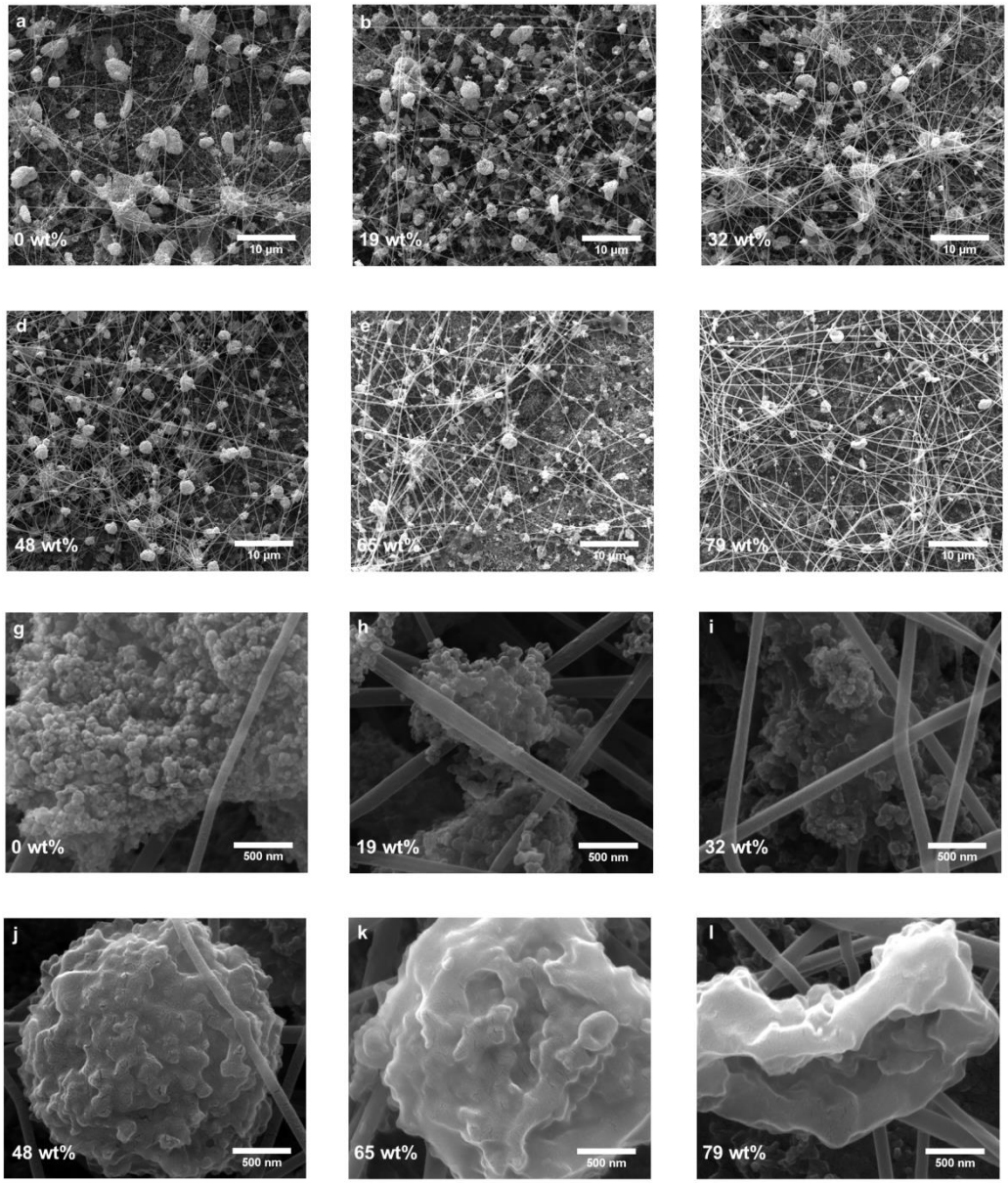

Figure 2.2 SEM images of E/E electrode with various Nafion contents in electrospraying solution: (a,g) 0 wt%, (b,h) 19 wt%, (c,i) 32 wt%, (d,j) 48 wt%, (e,k) 65 wt%, and (f,l) 79 wt%. (a-f) X 5000 magnification, scale bar = 10 μm; (g-l) X 30000 magnification, scale bar = 500 nm.

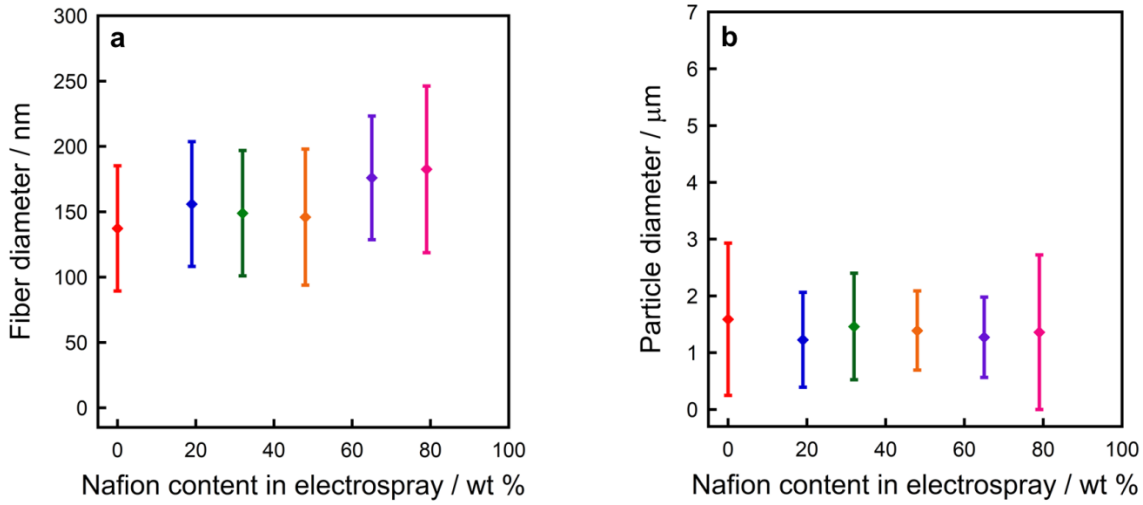

Figure 2.3 (a) Fiber diameters and (b) particle diameters in the E/E catalyst layers as a function of Nafion content in the electrospray.

Figure 2.2g–l (higher magnification of the catalyst layers; specifically focusing on the catalyst particles) shows that there are distinct visual differences at a local level in the appearance of the particle aggregates at varying amounts of Nafion in the electrospraying solution. From Figure 2.2g to Figure 2.2i, *i.e.*, from no Nafion to a small amount of Nafion in the electrospraying solution (0 to 32 wt% Nafion), there is an appearance of polymer that adheres between Pt/C particles. From Figure 2.2j, at 48 wt% Nafion, the Nafion ionomer completely surrounds the particles and creates a thin film around the aggregate. Figures 2.2k and 2.2l (65 wt% and 79 wt% Nafion), the Nafion film is thicker and separate Pt/C particles can no longer be distinguished within the aggregates. Therefore, by increasing the amount of Nafion in the electrospraying solution, the particle aggregates begin to change appearance, but maintain relatively similar particle aggregate sizes and overall catalyst layer morphology, while the Nafion ionomer thin film that surrounds the aggregate becomes more visible and thicker. Thus, these results indicate that the amount of Nafion content in the electrospraying solution did not influence the

macroscale morphology of the catalyst layer, but influenced the microscale appearance and composition around the catalyst aggregate particles. This allows for the exclusive study of the ionomer resistance on fuel cell performance without altering the overall catalyst layer morphology.

Figure 2.4 shows fuel cell performances (polarization and power curves; hydrogen/oxygen and hydrogen/air at ambient pressure at 80 °C) for E/E electrodes at 0.05 mg_{Pt} cm^{-2} total loading (produced with 48 wt% Nafion of the solids in the electrospraying solution) and for conventional painted electrodes (control) at 0.1 mg_{Pt} cm^{-2} total loading. Under hydrogen/oxygen, the maximum power density for the E/E electrodes (567 mW cm^{-2}) is similar to that of conventional electrodes (561 mW cm^{-2}) with only 50% of the Pt loading compared to the conventional electrodes. Under hydrogen/air, the maximum power density for the E/E electrodes (262 mW cm^{-2}) is also similar to that of conventional electrodes (250 mW cm^{-2}). These results further emphasize the influence of morphology in ultra-low Pt loading catalyst layers on fuel cell performance as demonstrated in previous studies.[61, 109]

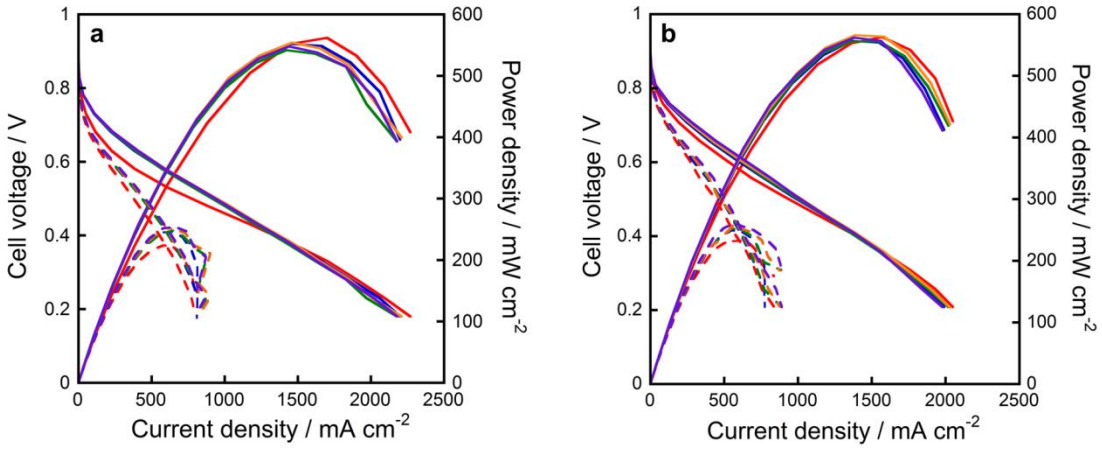

Figure 2.4 Fuel cell performance and polarization curves of MEAs with (a) E/E electrodes with 0.05 mg_{Pt} cm^{-2} and (b) conventional electrodes with 0.1 mg_{Pt} cm^{-2} under hydrogen/oxygen (solid) and hydrogen/air (dashed).

As shown in Figure 2.5a, the maximum power density for E/E electrodes varies with the amount of Nafion content in the electrospraying ink solution. Under hydrogen/oxygen, from 0 to 32 wt% Nafion content of the solids in the electrospraying solution, there is minimal difference in the maximum power density, which ranges between 415 mW cm^{-2} and 455 mW cm^{-2}. However, at 48 wt% Nafion content of the solids in the electrospraying solution, the power density increases to 567 mW cm^{-2}, which is a 36% gain in power output. From 48 to 65 wt% Nafion content of the solids in the electrospraying solution, the power density slightly decreases to 521 mW cm^{-2}, which corresponds to 8% loss in power output. From 65 wt% to 79 wt% Nafion content of the solids in the electrospraying solution, the power density continues to decrease to 412 mW cm^{-2}, which is an additional 21% loss in power output. This trend is similar for fuel cell performances under hydrogen/air as well. From 0 to 32 wt% Nafion content in the electrospraying solution, there is minimal difference in the maximum power density, which ranges between 170 mW cm^{-2} and 180 mW cm^{-2}. However, at 48 wt% Nafion content of the solids in the electrospraying solution, the power density increases to 262 mW cm^{-2}, which is a 53% gain in power output. From 48 to 65 wt% Nafion content of the solids in the electrospraying solution, the power density decreases to 204 mW cm^{-2}, which corresponds to 22% loss in power output. From 65 wt% to 79 wt% Nafion of the solids in the electrospraying solution, the power density continues to decrease to 142 mW cm^{-2}, which is an additional 30% loss in power output. These results suggest that low Nafion content (0 to 32 wt% of solids in the electrospraying solution), where the Nafion ionomer has no or little presence as shown in the left inset SEM image in Figure 2.5a, there is no or minimal effect on fuel cell performance; therefore, proton conductivity between the particle aggregates may be constant. This is supported by the SEM images shown previously in Figure 2.2g–i, where the Nafion ionomer does not completely cover

the aggregate until 48 wt% as shown in Figure 2.2j. The increase in power density from 32 wt% to 48 wt% Nafion content can be explained by the Nafion ionomer coverage around the particle aggregate which promotes proton conductivity to the triple phase boundaries. As illustrated by Figure 1.4a, the lack of proton pathways will introduce charge transfer resistance, which is evident in the low Nafion content (0 to 32 wt%) electrodes, where not all of the particle aggregates are visibly connected to the ionomer as shown in the left inset SEM image in Figure 2.5a (0 wt% Nafion content in the electrospraying solution). However, at 48 wt% Nafion content of the solids in the electrospraying solution, as shown by the middle inset SEM image of Figure 2.5a, there is enough ionomer content that allows each catalyst aggregate to effectively transport protons at each reaction site, as illustrated in Figure 1.4b, which reduces the charge transfer resistance and improves the power density. In addition, the amount of ionomer that surrounds the entire catalyst particle aggregate, as illustrated in Figure 1.4b, is low enough to allow gas to diffuse through, and therefore mass transfer resistance is also minimized. Thus, at 48 wt% Nafion content, the highest maximum power density is achieved by diminishing the charge and mass transfer resistances. At higher Nafion content (65 wt% to 79 wt% of the solids in the electrospraying solution), the power density steadily decreases. As seen previously in Figure 2.2e–f, with higher Nafion content, the particle aggregates cannot be visually seen due to the dense ionomer coverage, which increases mass transport resistance. As previously illustrated in Figure 1.4b, mass transport resistance can occur when the solid ionomer blocks reactant gas from reaching Pt reaction sites. This resistance is visually demonstrated by the right inset SEM image in Figure 2.5a (79 wt% Nafion content of the solids in the electrospraying solution), where the Nafion ionomer completely covers the aggregate and individual particles are no longer distinguishable. Therefore, the solid ionomer becomes a physical barrier for gas diffusion and

prevents reactant gas from reaching Pt reaction sites, which effectively decreases the power density.

Electrochemical impedance spectroscopy is a widely used technique to investigate the inner processes of fuel cells, such as electrode degradation,[112] proton transfer,[113] reaction kinetics on thin film fuel cell electrodes,[31] and catalyst layer resistances for PEMFCs;[114-116] specifically ionic conductivities[117-119] and oxygen transport resistances.[32] Springer *et al.*[114] first proposed and experimentally verified one of the earlier circuit models to describe PEMFCs under operation, and identified and correlated different frequency regimes with different transport processes along the polarization curve. Since then, multiple studies have proposed more complex models to study and identify specific transport processes within the catalyst layer.[33, 116, 119-120] To further explore the impact of Nafion ionomer on fuel cell performance, the catalyst layer resistance was measured with electrical impedance spectroscopy under hydrogen/oxygen at ambient pressure at 80 °C at -0.4 V versus OCV (*ca*. 0.49–0.55 V *versus* NHE), which is at a slightly lower voltage compared to the voltage where the maximum power density was observed. As shown in Figure 2.6b, the average catalyst layer resistance is relatively steady between 320 and 350 mΩ cm^2 from 0 to 32 wt% Nafion content of the solids in the electrospraying solution, indicating that at low Nafion content, where proton transport resistance is expected to be high in conventional electrodes due to the poor proton connection between particles and ionomer (as shown in Figure 2.2h and illustrated in the left inset in Figure 2.5b), there is little to no effect on fuel cell performance for E/E electrodes because protons can be transferred through the Nafion in the nanofibers, regardless of the amount of Nafion ionomer in the electrospraying solution. From 32 wt% to 48 wt% Nafion content of the solids in the electrospraying solution, there is a decrease in the average catalyst layer resistance from 320 to 240 mΩ cm^2, which suggests that the

continuous thin film formation around catalyst particle aggregates (as shown in Figure 2.2k further improves proton transport and increases the triple phase boundary. From 48 wt% to 79 wt% Nafion content of the solids in the electrospraying solution, the average catalyst layer resistance increases from 240 to 490 mΩ cm^2, which may be attributed to the increase in mass transport resistance as the thin film that surrounds the Pt/C aggregate increases in thickness (as shown in Figure 2.2l and illustrated in the right inset in Figure 2.5b). This result suggests that at higher ionomer content in E/E electrodes, mass transport resistance is more dominant than proton transport resistance. Overall, these results show that there is a balance between proton transport and mass transport in E/E electrodes that can be observed by changing the Nafion ionomer content in the electrospray in order to optimize fuel cell performance.

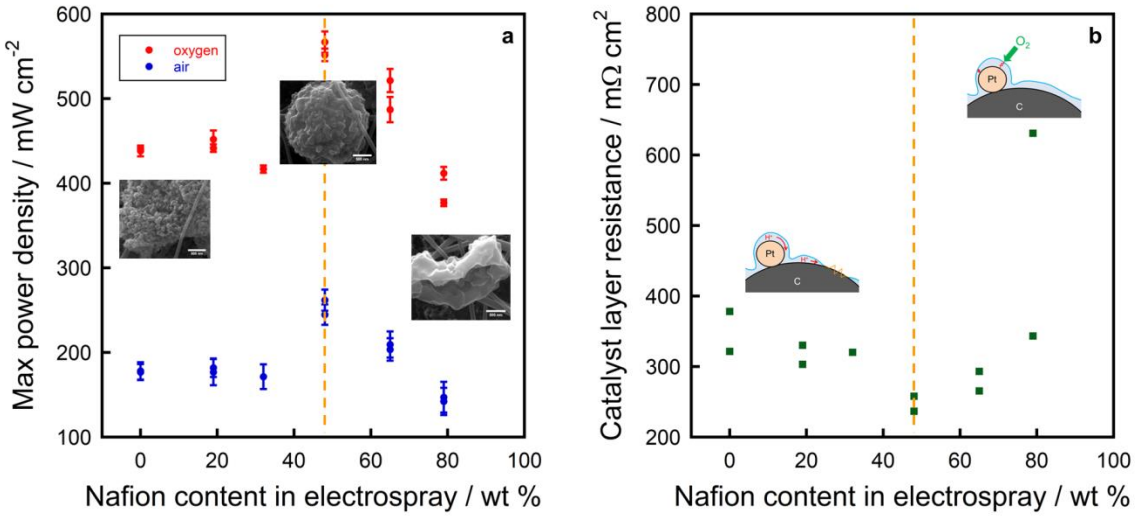

Figure 2.5 (a) Maximum power density under oxygen (red) and air (blue) versus Nafion content in electrospray for E/E MEAs with insets representing high magnification SEM images of catalyst aggregate particles at given Nafion contents: 0 wt%, 48 wt%, and 79 wt% (left to right)) and (b) catalyst layer resistance versus Nafion content in electrospray for E/E MEAs with illustrations of proton transport resistance (left) and mass transport resistance (right). The highest value for maximum power density and minimum resistance is indicated by the dashed vertical line (orange) in (a) and (b), respectively.

Table 2.2 summarizes these results: maximum power density, catalyst layer resistance, average electrode Pt loading, and electrochemical surface area (ECSA). The ECSA is a measure of the adsorption or desorption of hydrogen onto the Pt sites; therefore, it is also dependent on the porous structure, electron conductivity, and proton conductivity. From the SEM images, the morphology is similar for all E/E experiments, as stated previously. Therefore, the only difference is the connectivity and thickness of the proton conducting ionomer network surrounding the catalyst particle aggregates, which subsequently depends on the ionomer content in the electrospraying solution. The ECSA steadily increases from 21.9 $m^2\ g_{Pt}^{-1}$ to 42.9 $m^2\ g_{Pt}^{-1}$ for 0 to 32 wt% Nafion content of the solids in the electrospraying solution, rapidly increases to 99.0 $m^2\ g_{Pt}^{-1}$ at 48 wt% Nafion content, and then decreases to 69.6 $m^2\ g_{Pt}^{-1}$ and 22.3 $m^2\ g_{Pt}^{-1}$ for 65 wt% Nafion content and 79 wt% Nafion content, respectively. The increase in the ECSA may be attributed to the increase in proton transport, which allows for more Pt particles to be accessible, thereby increasing the ECSA. Overall, this trend is similar to the trends observed for power density (Figure 2.5a) and catalyst layer resistance (Figure 2.5b). Specifically, at higher Nafion content (from 48 wt% to 79 wt% of solids in the electrospraying solution), the decreasing trend in the ECSA values suggests that the solid ionomer is effectively blocking hydrogen gas from reaching the Pt sites and thereby reducing the amount of available Pt surface area for the reaction to occur.

Table 2.2 Pt loading, electrochemical surface area, maximum power density, and catalyst layer resistance for E/E electrodes with different Nafion contents in electrospraying solution.

Nafion content in solids (wt%)	Pt loading (mg_{Pt} cm^{-2})	Max power density[a] (mW cm^{-2})	Max power density[a,c] (kW g_{Pt}^{-1})	Catalyst layer resistance[a] ($m\Omega$ cm^2)	ECSA[b] (m^2 g_{Pt}^{-1})
0	0.052	438.2 ± 6.3	4.21 ± 0.06	321.4	21.9 ± 3.1
19	0.041	452.0 ± 10.3	5.51 ± 0.13	303.2	39.2 ± 5.4
32	0.049	416.8 ± 4.3	4.25 ± 0.04	320.4	42.9 ± 5.9
48	0.049	566.8 ± 12.6	5.78 ± 0.13	236.8	99.0 ± 17.2
65	0.042	521.4 ± 13.8	6.21 ± 0.16	265.5	69.6 ± 7.7
79	0.043	411.8 ± 7.6	4.79 ± 0.09	631.0	22.3 ± 2.2

[a]Measured at 1/2 mol/mol H_2/O_2 at 80 °C, ambient pressure.
[b]Measured at 2/1 mol/mol H_2/N_2 at 30 °C, ambient pressure.
[c]Calculated using the total Pt loading in the MEA.

The optimum ionomer content for conventional catalyst layers in fuel cell electrodes has been thoroughly investigated and reported to be approximately 30 wt%.[19, 21, 121] To compare the optimum total ionomer content in the E/E electrodes to that of conventional electrodes, the total Nafion content in the E/E electrodes, including the Nafion from the nanofibers, was calculated. As shown in Figure 2.6, the current density at 0.6 V *versus* NHE under hydrogen/air for the E/E MEAs from this study is compared to the results from Qi *et al.*[122] for conventional MEAs. The conventional MEAs show a maximum current density at 30 wt% Nafion content in the electrodes. However, for E/E MEAs, the maximum current density was observed at 62 wt% Nafion, which is a 93% increase from the optimum Nafion content compared to conventional electrodes. Interestingly, one study has shown that the optimum Nafion content changes with Pt loading, and at low Pt loading (0.1 mg_{Pt} cm^{-2}), the optimum Nafion content is 50 wt%,[123] which suggests that at ultra-low Pt loadings (< 0.1 mg_{Pt} cm^{-2}), the optimum ionomer content may differ from that at a conventional loading (*ca*. 0.4 mg_{Pt} cm^{-2}). Therefore, by utilizing the E/E technique, electrode catalyst layers with ultra-low Pt loadings and different ionomer contents can be

investigated to optimize and understand the role of the ionomer thin film resistance on fuel cell performance, while maintaining a constant catalyst layer morphology.

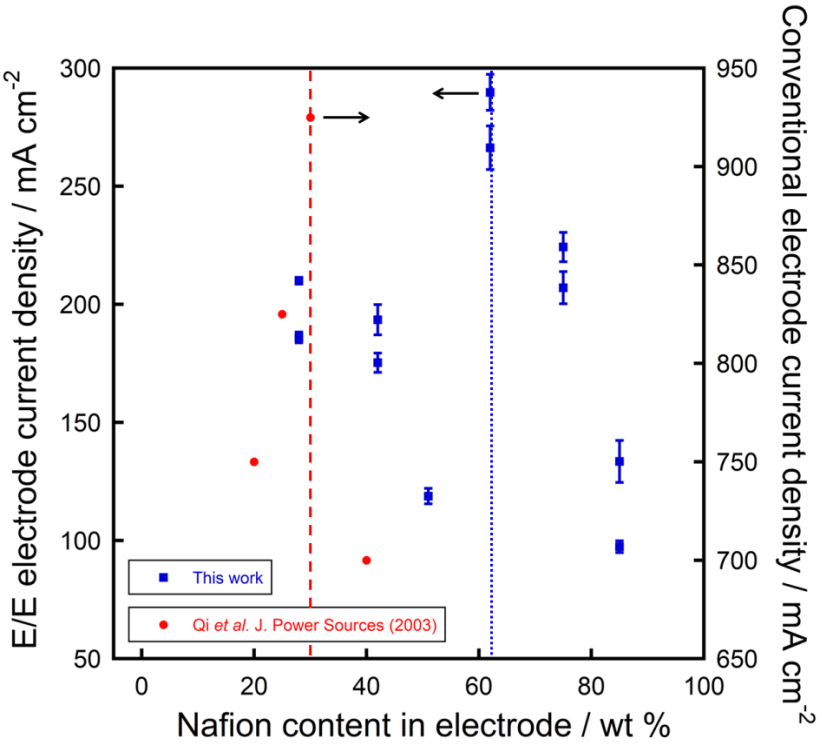

Figure 2.6 E/E electrode current density (blue) and conventional electrode current density (red) versus total Nafion content in the electrode. The optimum total Nafion content is indicated by the dotted (blue) and the dashed (red) vertical lines for the E/E electrode and the conventional electrode, respectively.

In this study, the fuel cell performance of E/E electrodes were similar to conventional electrodes (control), but the total Pt loading were not similar. Figure 2.7 shows fuel cell performance of the E/E electrodes with similar overall Pt loading compared to the control (0.1 mg_{Pt} cm^{-2}). Under hydrogen/oxygen, the average maximum power density for these E/E electrodes (690 mW cm^{-2}) was observed to be 23% higher than control electrodes (561 mW cm^{-2}) at similar total Pt loadings. Similarly, under hydrogen/air, the average maximum power density

for the E/E electrodes (372 mW cm^{-2}) was observed to be 49% higher than that for the control electrodes (250 mW cm^{-2}). Overall, compared to conventional electrodes, the enhanced morphology the E/E electrodes (increased triple phase boundaries) results in similar fuel cell performance at lower Pt loadings or higher fuel cell performance at similar Pt loadings.

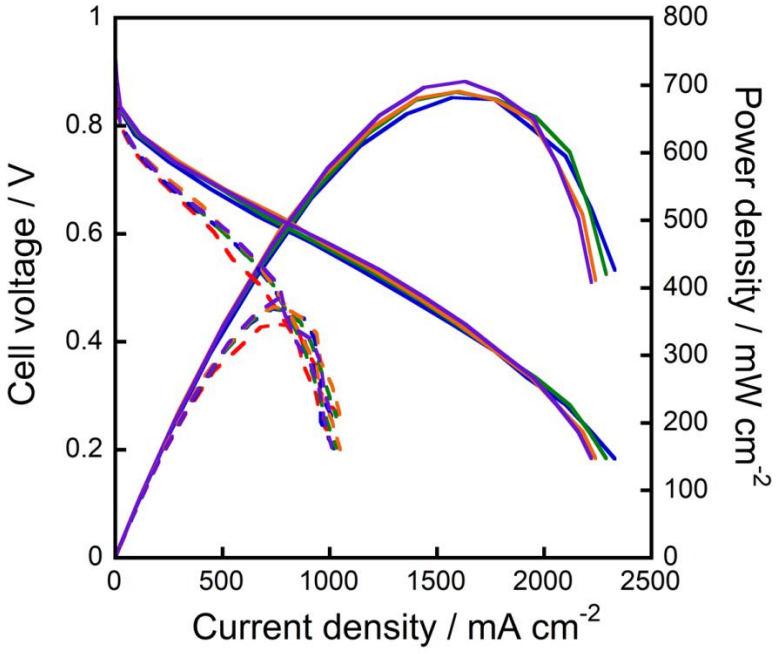

Figure 2.7 Fuel cell performance and polarization curves of MEAs with E/E electrodes with 0.1 mg_{Pt} cm^{-2} under hydrogen/oxygen (solid) and hydrogen/air (dashed).

2.4. Conclusions

In this study, the simultaneous E/E technique provides a platform to produce electrodes with similar overall morphology at various ionomer contents, which allows for the exclusive exploration of the impact of the ionomer thin film on catalyst layer resistances and subsequently fuel cell performances. As ionomer content increased, the catalyst layer resistance decreased and then increased, which was attributed to charge transfer resistance at low ionomer content and

mass transport resistance at high ionomer content. However, unlike conventional electrodes, at low ionomer content, a connected proton conducting network still exists in E/E electrodes due to the presence of Nafion nanofibers, and at high ionomer content, a highly porous network still exists in E/E electrodes due to the nanofiber-nanoparticle network. Therefore, the catalyst layer resistances observed are exclusive to the Nafion thin film surrounding the catalyst aggregate particles and not the overall connected pore-ionomer-catalyst morphology. Overall, for E/E electrodes, a maximum in power density and minimum in catalyst layer resistance was observed at 62 wt% Nafion, which differs from conventional electrodes (30 wt%). Furthermore, E/E electrodes had a similar power density compared to conventional electrodes at half the Pt loading (0.05 mg_{Pt} cm^{-2}) and higher power density at similar Pt loading (0.1 mg_{Pt} cm^{-2}).

CHAPTER III

HIGH PRODUCTION RATE OF HIGH PURITY, HIGH FIDELITY NAFION NANOFIBERS *VIA* NEEDLELESS ELECTROSPINNING

3.1 Introduction

Nafion is commercially available in several forms, including extruded and solution cast films, dispersions in aqueous alcohol solvents, and pellets. In addition to these forms, Nafion in nanofiber form has been reported and has shown to possess enhanced properties (*e.g.,* proton conductivity) and subsequently enhances device performance.[104, 124-147] One example includes Snyder and Elabd[143] who reported on Nafion nanofibers that naturally form in fuel cell electrodes due to heat and pressure and subsequently improves fuel cell performance. Another example includes Dong *et al.*[140] who reported on the super proton conductivity (> 1 S cm^{-1}) of a single high-purity Nafion nanofiber (400 nm diameter), which is an order of magnitude higher than a bulk Nafion film (*ca.* 0.1 S cm^{-1}). Also, Wang *et al.*[124-125] reported on Nafion nanofiber fuel cell electrodes and their subsequent excellent high fuel cell power densities at ultra-low platinum loadings (*i.e.,* excellent platinum utilization of 0.076 g kW^{-1}). Additionally, Ballengee and Pintauro[133] reported on Nafion nanofiber composite membranes and their subsequent enhanced durability under humidity cycling for fuel cells.

To date, most reports on Nafion nanofibers resulted from the fibers being produced *via* single needle electrospinning.[104, 124-142, 144-150] Needle electrospinning is the most common technique to produce polymer fibers with nanometer sized diameters (*ca.* 10-1,000 nm). This involves applying a high-voltage electric field to a polymer solution that is ejected out of a metal needle. Above a critical voltage, electrostatic forces overcome surface tension to form a polymer jet that

is elongated and whipped continuously onto a grounded collector as a randomly interconnected fibrous mat. Electrospinning parameters, such as voltage, distance, and flow rate can affect how fibers form (*i.e.,* uniformity of the fibers), while polymer solution properties, such as viscosity (*i.e.,* polymer chain entanglement) and conductivity (*i.e.,* electrostatic driving forces), can determine whether a polymer solution can be electrospun to form fibers at all.

Currently, no studies have demonstrated electrospinning of pure Nafion nanofibers, but rather successful electrospinning of Nafion requires the addition of a secondary polymer, such as poly(ethylene oxide) , poly(acrylic acid), poly(vinyl pyrrolidone), poly(vinyl alcohol), and poly(vinylidene fluoride), to the polymer solution prior to electrospinning.[140, 144-150] In solution, pure Nafion aggregates into micellar structures, which inhibits polymer chain entanglement and subsequently successful electrospinning.[151] The addition of a secondary polymer to the Nafion solution has been shown to prevent aggregate formation, increase chain entanglement, and promote the successful electrospinning of Nafion nanofibers.[150] Therefore, it is challenging to electrospin high purity Nafion nanofibers using conventional needle electrospinning, limiting needle electrospinning to narrow solution concentration ranges and requiring the addition of a secondary polymer.

Furthermore, all of the Nafion electrospinning studies reported to date use single needle electrospinning, which results in low nanofiber production rates (0.01-0.1 g h^{-1}).[152-153] Numerous needleless electrospinning techniques have been developed and explored to increase the production rate of polymer nanofibers, such as upward electrospinning,[154] bubble electrospinning,[155-156] and free surface electrospinning,[152, 157] with various polymers, such as poly(vinyl alcohol) and poly(vinyl pyrrolidone). These needleless electrospinning techniques have resulted in production rates up to 5 g h^{-1},[157] which is an order of magnitude higher than

conventional single needle electrospinning, illustrating the potential to mass produce nanofibers. However, almost all needleless electrospinning techniques produce lower fidelity nanofibers compared to needle electrospinning. Recently, Higham *et al.*[158] developed a new needleless electrospinning technique, known as foam electrospinning, that produced similar fidelity nanofibers compared to that of needle electrospinning. In their study, they demonstrated this with two neutral polymers: poly(ethylene oxide) and poly(vinyl alcohol). In this study, we demonstrate the needleless electrospinning of an ionic polymer, Nafion, using a similar technique described by Higham *et al.*[158] The production rate, fidelity, purity, and properties of Nafion nanofibers produced by needleless electrospinning were investigated and compared to Nafion nanofibers produced by conventional needle electrospinning.

3.2 Experimental Methods

3.2.1 Materials

Isopropanol (IPA; ACS reagent, ≤ 99.5%) and poly(acrylic acid) (PAA; M_V = 450,000 g mol^{-1}) were purchased from Sigma-Aldrich. 1100 EW Nafion solution at 5 wt% in a 3/1 v/v of isopropanol/water and 15 wt% in a 3/1 v/v of isopropanol/water were purchased from Ion Power. All materials were used as received. Deionized (DI) water with a resistivity of 16 MΩ cm was used as appropriate. Dry compressed air was provided using an industrial air compressor (IRN50H-0F, Ingersoll Rand Industrial Technologies).

3.2.2 Preparation of Nafion Solutions for Electrospinning

Nafion solution (5 wt%) was added to solid PAA and subsequently stirred under ambient temperature for at least 12 h to ensure complete dissolution. The amount of PAA was adjusted to

produce Nafion/PAA solutions of various compositions in order fabricate Nafion fibers with various Nafion compositions (*e.g.*, 5 g of 5 wt% Nafion solution, 50 mg of PAA for 83 wt% Nafion content of the solids in the electrospinning solution). The 15 wt% Nafion solution was used to produce higher Nafion content (> 92 wt%) nanofibers (*e.g.*, 5 g of 15 wt% Nafion solution and 15 mg of PAA for 98 wt% Nafion content of the solids in the electrospinning solution). 3/1 v/v isopropanol/water was then added to the Nafion/PAA solution to decrease the polymer concentration (*e.g.*, 1280 mg of Nafion/PAA solution and 670 mg of 3/1 v/v isopropanol/water) for smooth electrospinning.

3.2.3 Needle Electrospinning Apparatus

The needle electrospinning apparatus, as illustrated in Figure 3.1a, consists of a high-voltage power supply (PS/EL50R00.8, Glassman High Voltage, Inc.), syringe pump (NE-1000, New Era Pump Systems), glass syringe (Pt. No. CG-3070-03, Chemglass Life Sciences), syringe needle (i.d. = 0.024 in. (0.603 mm), Hamilton), poly(vinyl chloride) tubing (Pt. No. 30600-65, Cole-Parmer), and a grounded collector (9 in x 9 in (23 cm x 23 cm); square cardboard covered with aluminum foil). The flow rate was set to 0.3 mL h^{-1} for all needle electrospinning experiments. A still image of the needle electrospinning process (Taylor cone/fiber spinning from syringe needle tip) is shown in Figure 3.1b.

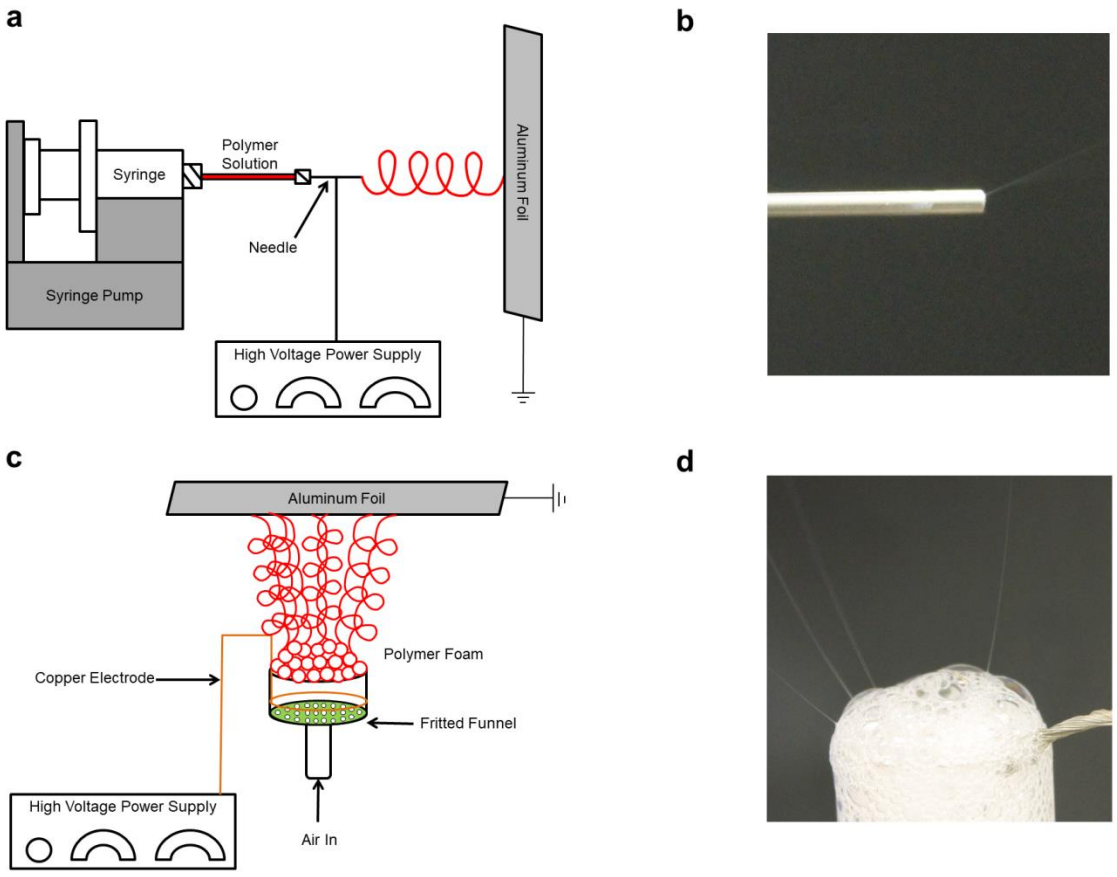

Figure 3.1 Illustration of (a) needle and (c) needleless electrospinning apparatuses and still images of (b) needle and (d) needleless electrospinning processes.

3.2.4 Needleless Electrospinning Apparatus

The needleless electrospinning apparatus, as illustrated in Figure 3.1c, consists of a high-voltage power supply (ES40P-10W/DAM, Gamma High Voltage Research, Inc.), glass fine-fritted funnel (Pt No. CG-1402-04, Chemglass Life Sciences), circular copper electrode (16 gauge wire), and a grounded collector (9 in x 9 in (23 cm x 23 cm); square cardboard covered with aluminum foil). Compressed air with controlled flow rate was passed through the funnel to produce stable polymeric foam at the top surface of the fritted funnel. A still image of the

needless electrospinning process (multiple Taylor cones/fiber spinning from polymeric foam/bubble surfaces) is shown in Figure 3.1d.

3.2.5 Characterization

The morphology of the fiber mats was investigated with scanning electron microscopy (SEM; FEI Quanta 600 FE-SEM, 10 kV for X 30000 magnifications images) using a working distance of 10 mm. Samples were sputter coated (Cressington 208 HR) with platinum/palladium (6 nm thickness) prior to SEM analysis. For each electrospinning experiment, the diameters of 25 nanofibers for each image were randomly selected and measured using ImageJ software, *i.e.*, fiber diameters reported are the average and standard deviation of 25 randomly selected fibers.

The production rate was determined by the amount of material collected after the electrospinning experiments at different time points. Foil circles were punched out using a hollow punch (dia. = 14 mm, Pt. 66004, Mayhew Pro). The average weight of six bare aluminum foil circles (6.6 mg) was used to tare the weight at t = 0 h. The average weight of four to six samples at different time intervals was taken from each electrospinning experiment to determine the weight after the experiment as a function of time.

Mechanical properties of the fiber mats (*ca.* 25 mm (L) x 0.5 mm (W)) were measured with dynamic mechanical analysis (DMA; Q800, TA Instruments) under the given conditions: 22 ± 2 °C, 40 ± 5% RH, preload force of 0.001 N, and a strain ramp rate of 0.1% min^{-1}. Stress-strain profiles were collected for each sample. The Young's modulus was measured from the initial slope of the stress-strain curve.

In-plane ionic conductivity of the fiber mats was measured with electrochemical impedance spectroscopy (EIS; Solartron SI 1260A) in a four-point conductivity cell (BekkTech BT112,

Scribner Associates, Inc.) by sweeping frequencies from 1 MHz to 0.05 Hz with an amplitude of 10 mV at 0 V *versus* OCV under different temperatures ranging from 30 °C to 80 °C at 90% RH and submersed in liquid DI water at room temperatures (*ca.* 25 ± 2 °C). The temperature and relative humidity were controlled by placing the four-point conductivity cell in a bench top environmental chamber (ESPEC). Samples for EIS were prepared by electrospinning on glass substrates (*ca.* 30 mm (L) x 8 mm (W) x 1 mm (T)) for fiber mats. A film was cast on glass substrates and dried for at least 24 h under ambient conditions to compare to the fiber mats. All samples were annealed at 140 °C for 15 min prior to testing the in-plane conductivities. The data was analyzed by determining the high-frequency intercept of the real impedance, *R*, which was measured between the two inner reference electrodes. Conductivity was calculated by using the following equation: $\sigma = L/(AR)$, where *L* is the distance between the two inner electrodes (*ca.* 0.48 mm) and *A* is the cross-sectional area of the sample ($A = Wl$; *W* is the sample width and *l* is the sample thickness). The sample thicknesses, ranging from 20 to 60 μm, were measured with a Marathon digital micrometer (Pt No. CO030025) with ± 2 μm accuracy. Samples were allowed to equilibrate for 2 h at each temperature at 90% RH followed by three to four repeated measurements. The reported values are the average of these measurements. Due to the porosity of the fiber mats, the effective conductivity was calculated using the following equation: $\sigma_c = \sigma A/A_c = \sigma/(1-v)$, where σ is the measured conductivity, A_c is the effective surface area (surface area covered by the fibers), and *v* is the surface area void fraction, or surface porosity, of the fiber mats. Assuming the fiber mats are isotropic, the in-plane surface void area fraction of the fiber mat was used to determine the cross-sectional void area fraction. The average of the in-plane surface void area fractions for two different SEM images was used for the final calculation for each fiber mat.

3.3 Results and Discussion

Figure 3.2 shows scanning electron microscopy images of Nafion nanofibers produced from both the needle electrospinning technique (Figure 3.2a–c) and the needleless electrospinning technique (Figure 3.2d–f) at various Nafion contents of the solids in the electrospinning solution (83 wt%, 88 wt%, and 92 wt%). At 83 wt% and 88 wt% Nafion content, both needle and needleless electrospinning techniques can produce uniform defect-free fibers. However, using the needle electrospinning technique, as the amount of Nafion content of the solids in the Nafion/PAA solution increases from 88 wt% (Figure 3.2b) to 92 wt% (Figure 3.2c), the fibers begin to show defects, such as beads, whereas the needleless electrospinning technique still produces defect-free fibers (Figure 3.2f). This beaded fiber-to-smooth fiber transition has been previously reported by Chen *et al.*[150] with the needle electrospinning technique at 92 wt% Nafion content of the solids in the solution. Therefore, although both electrospinning techniques are using the same polymer solution, at a higher Nafion content solution, the needle electrospinning technique produces a lower quality of nanofibers (*e.g.,* beaded nanofibers), whereas the needleless electrospinning technique fabricates defect-free nanofibers at the same higher Nafion concentrations. These results suggest that the needleless electrospinning technique enhances electrospinning, which may be a result of increasing the polymer concentration locally on the polymer solution thin bubble surfaces (foam).

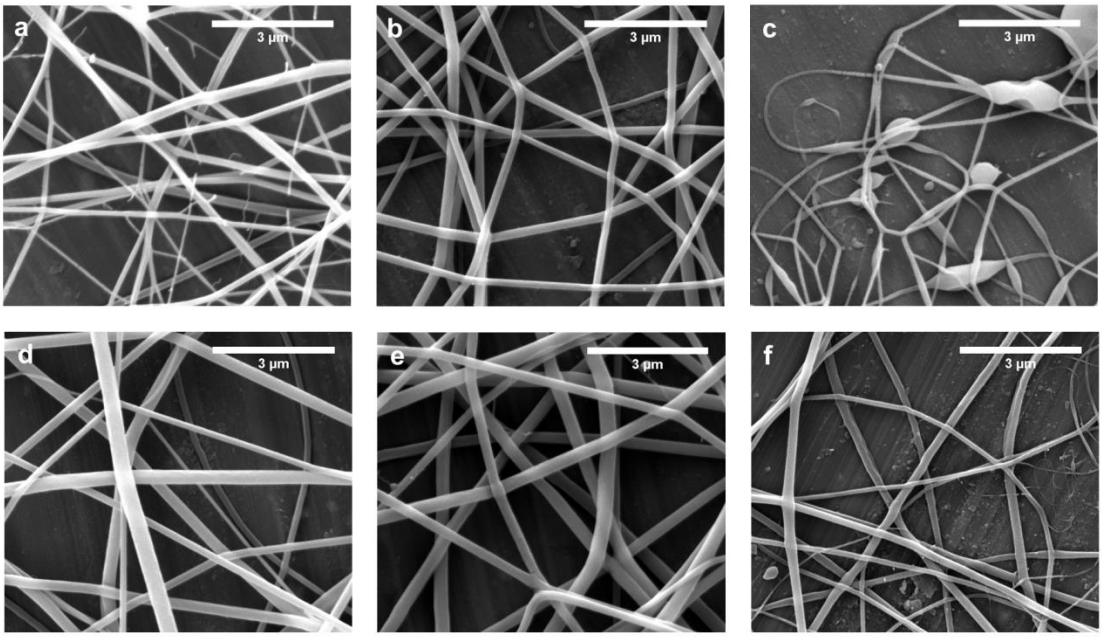

Figure 3.2 SEM images of electrospun Nafion nanofibers at Nafion contents of 83 wt% (a,d), 88 wt% (b,e), and 92 wt% (c,f) fabricated using needle electrospinning (a-c) and needleless electrospinning (d-f). X 30000 magnification, scale bar = 3 µm.

Previous studies have shown that higher polymer concentrations (concentrations above the polymer entanglement concentration) promote the formation of uniform, bead-free fibers produced *via* electrospinning.[158-159] Therefore, to promote the electrospinning of higher purity Nafion solutions, the polymer concentrations were increased to 10 and 6 wt% to electrospin 95 wt% and 98 wt% Nafion content of the solids in the solution, respectively. As shown in Figure 3.3a,c, both techniques can produce nanofibers for the 95 wt% Nafion content of the solids in the solution at 10 wt% polymer concentration. However, needle electrospinning produces beaded nanofibers at this polymer concentration, as shown in Figure 3.3a, whereas needleless electrospinning produces bead-free or defect-free nanofibers, as shown in Figure 3.3c. Also, the needle electrospinning technique requires frequent monitoring and clearing at the needle tip to inhibit solution clogging and non-continuous electrospinning of fibers for this polymer solution.

At 98 wt% Nafion content of the solids in a 6 wt% polymer solution, needle electrospinning produces multiple beads with few small fibers in between the beads, as shown in Figure 3.3b, whereas needleless electrospinning can still produce bead-free fibers, as shown in Figure 3.3d. These results demonstrate that needleless electrospinning produces higher purity defect-free Nafion nanofibers compared to needle electrospinning due to the increase in local polymer concentration at the bubble surfaces.

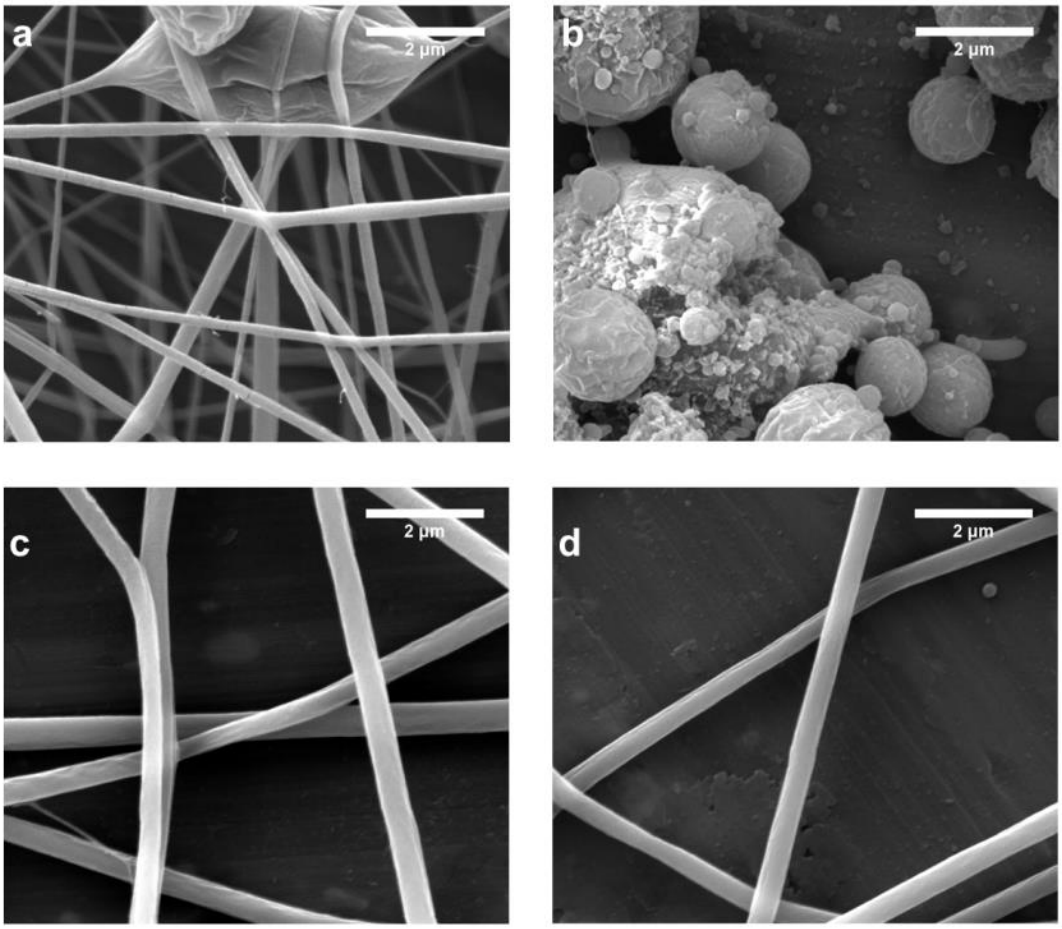

Figure 3.3 SEM images of Nafion nanofibers at Nafion contents of 95 wt% (a,c) and 98 wt% (b,d) fabricated using needle electrospinning (a,b) and needleless electrospinning (c,d). X 30000 magnification, scale bar = 2 µm.

Figure 3.4 shows the average fiber diameters of the images shown in Figure 3.2. The average fiber diameters for the 83, 88, and 92 wt% Nafion content of the solids in the solution fabricated using the needle electrospinning technique are 216, 130, and 110 nm, respectively. The average fiber diameters for 83, 88, and 92 wt% Nafion content of the solids in the solution fabricated using the needleless electrospinning technique are 233, 179, and 156 nm, respectively. The needle and needleless electrospinning techniques both produced similar diameter size fibers (*i.e.*, similar fidelity) for various Nafion contents of the solids in the solution. Both techniques also display similar trends in decreasing fiber diameter with increasing Nafion content, which is in agreement with the electrospinning of Nafion and PAA study by Chen *et al.*,[150] where nanofiber diameters ranging from 90 nm to 600 nm for a PAA content of 8 wt% to 100 wt%, respectively, were reported.[150, 159] Thus, needleless electrospinning can produce similar fidelity Nafion nanofibers as those produced by needle electrospinning.

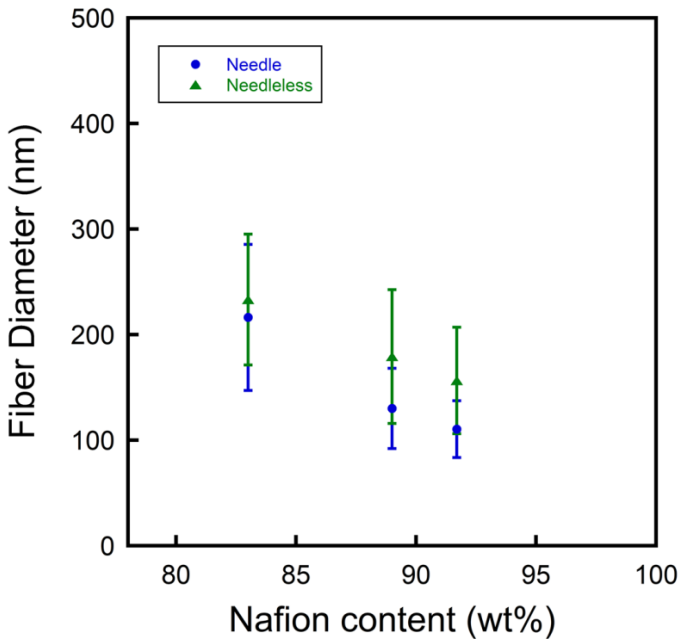

Figure 3.4 Nafion nanofiber diameters as a function of Nafion content fabricated using needle electrospinning (blue circles) and needleless electrospinning (green triangles).

Figure 3.5 shows the effect of various electrospinning parameters on the resulting fiber diameters for the needleless electrospinning technique, including polymer concentration (wt%), funnel-to-target distance (cm), and voltage (kV). Results show that the average fiber diameter for 4.0, 5.0, and 5.9 wt% polymer solutions is 216, 252, and 232 nm, respectively (see Figure 3.5a). These average fiber diameters are statistically similar, which demonstrates the ability of the needleless electrospinning technique to produce similar fiber diameters with different polymer concentrations. In Figure 3.5b, the funnel-to-target distance was varied from 13, 15, and 17 cm and the resulting fiber diameters are 392, 232, and 326 nm. Using a distance of 13 or 17 cm resulted in a higher standard deviation in the fiber diameter compared to that using a distance of 15 cm, suggesting that at 20 kV, 15 cm is the optimal distance for maintaining high fidelity fibers with similar diameter sizes. The applied voltage was varied from 15, 20, and 25 kV, and the resulting fiber diameters are 375, 232, and 292 nm (see Figure 3.5c). Applying a voltage of 20 or 25 kV resulted in higher standard deviation in the fiber diameter compared to that using a voltage of 15 kV, suggesting that at 15 cm, 15 kV is the optimal voltage for fabricating similar fiber diameter sizes. By changing electrospinning parameters, such as distance and voltage, the fiber diameters can vary, but by fixing one parameter and optimizing the other parameters, there is a combination that offers the highest fidelity in nanofibers produced using the needleless electrospinning technique.

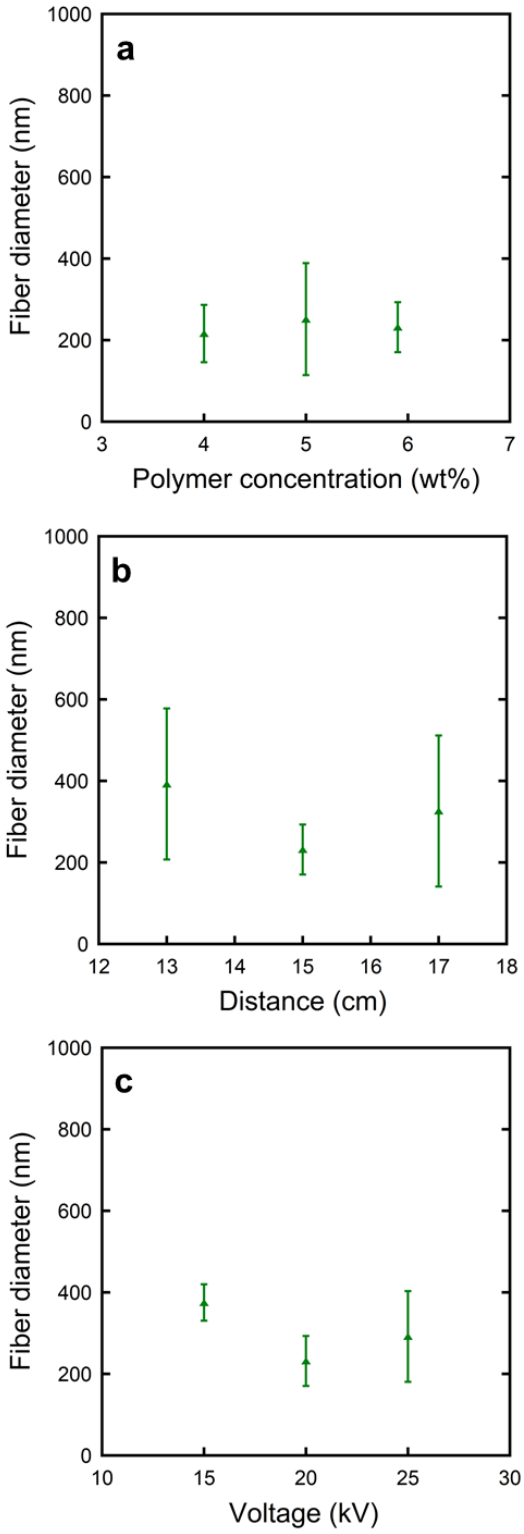

Figure 3.5 Nafion nanofiber diameters fabricated using needleless electrospinning as a function of (a) polymer concentration, (b) funnel-to-target distance, and (c) voltage.

Figure 3.6 shows the production rate of nanofibers fabricated using both the needle and needleless electrospinning techniques. The production rate for needle electrospinning ranges from 0.09 to 0.16 mg h^{-1} across a voltage range from 10 to 30 kV. From 10 to 20 kV, the needle electrospinning production rate is constant around 0.10 mg h^{-1} followed by a slight increase to 0.16 mg h^{-1} at 30 kV. The production rate for the needleless electrospinning technique ranges from 0.04 to 1.00 mg h^{-1} across a voltage range from 10 to 30 kV. At 15 kV, the production rate for the needleless electrospinning technique is 0.41 mg h^{-1}. From 15 to 20 kV, the production rate for needleless electrospinning increases to 0.71 mg h^{-1}. From 20 to 25 kV, the production rate for the needleless electrospinning technique further increases to 1.00 mg h^{-1}. At 30 kV, the production for the needleless electrospinning technique decreases to 0.82 mg h^{-1}. This decrease may be due to the strong electric field pulling the fibers from the surface faster than the production of the polymeric foam or curved surfaces. Comparing the two electrospinning techniques, at 10 kV, the production rate for needle electrospinning (0.11 mg h^{-1}) is slightly higher than that for needleless electrospinning (0.04 mg h^{-1}), which suggests that although there are multiple available curved surfaces for electrospinning, the voltage is not high enough to efficiently produce many Taylor cone jets for all the curved surfaces. At 20 kV, the production rate for needleless electrospinning (0.71 mg h^{-1}) is almost seven times larger than that for needle electrospinning (0.09 mg h^{-1}), demonstrating the ability of using the needleless electrospinning technique to quickly fabricate many nanofibers. At 25 kV, the needleless electrospinning production rate reaches its maximum at 1.00 mg h^{-1}, an order of magnitude larger than the needle electrospinning production rates. Therefore, there is an optimum voltage for the maximum production rate for needleless electrospinning; whereas, the production rate for needle electrospinning remains relatively constant with increasing voltage. Overall, needleless

electrospinning can produce Nafion nanofibers at an order of magnitude in higher production rate compared to needle electrospinning.

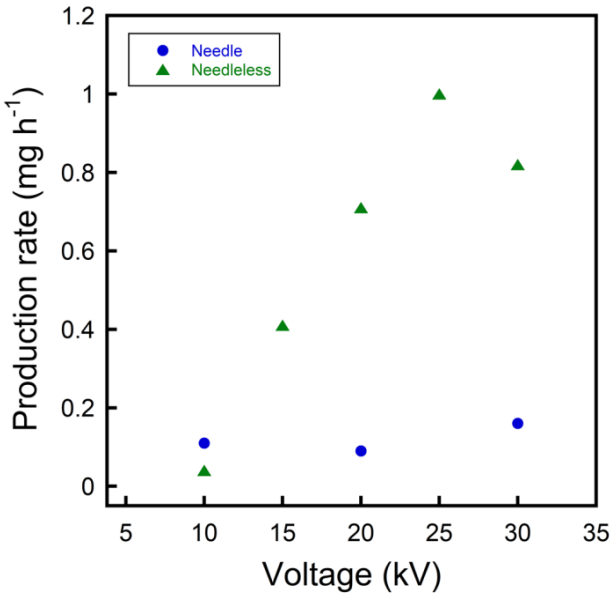

Figure 3.6 Nafion nanofiber production rate as a function of voltage for needle electrospinning (blue circles) and needleless electrospinning (green triangles).

In addition to purity, fidelity, and production rate, the physical properties of the resulting fiber mats produced by both needle and needleless electrospinning techniques were compared with one another and also compared to the bulk film (a control with similar Nafion/PAA composition as fibers). Table 3.1 lists the Young's modulus and proton conductivity for the film and the fiber mats for a composition of 83 wt% Nafion.

Table 3.1 Properties for fiber mats and cast film at 83 wt% Nafion content.

Fabrication	Young's modulus (MPa)[a]	Conductivity (mS cm^{-1})[b]
Cast film	130.0	54.3
Needle fiber mat	20.9	18.0
Needleless fiber mat	42.6	43.8

[a]Measured under ambient conditions (*ca.* 22 ± 2 °C, 40 ± 5% RH).
[b]Measured submersed in liquid deionized water at room temperature (*ca.* 25 ± 2 °C).

Overall, as expected, the film has a higher modulus (130.0 MPa) and proton conductivity (54.3 mS cm^{-1}) compared to both fiber mats. However, unexpectedly, the needleless electrospun fiber mat has a higher modulus (42.6 MPa) and proton conductivity (43.8 mS cm^{-1}) compared to the needle electrospun fiber mat (20.9 MPa and 18.0 mS cm^{-1}). One would expect that although the fibers were produced by different techniques that if their fidelities are similar than the properties should also be similar. However, at this composition, beaded-fibers were observed for the needle electrospun fibers (shown in Figure 3.7a) compared to defect-free fibers in the needleless electrospun fibers (shown in Figure 3.7c). The defects in the needle electrospun fibers may contribute to the differences in measured properties when compared to the defect-free needleless electrospun fibers.

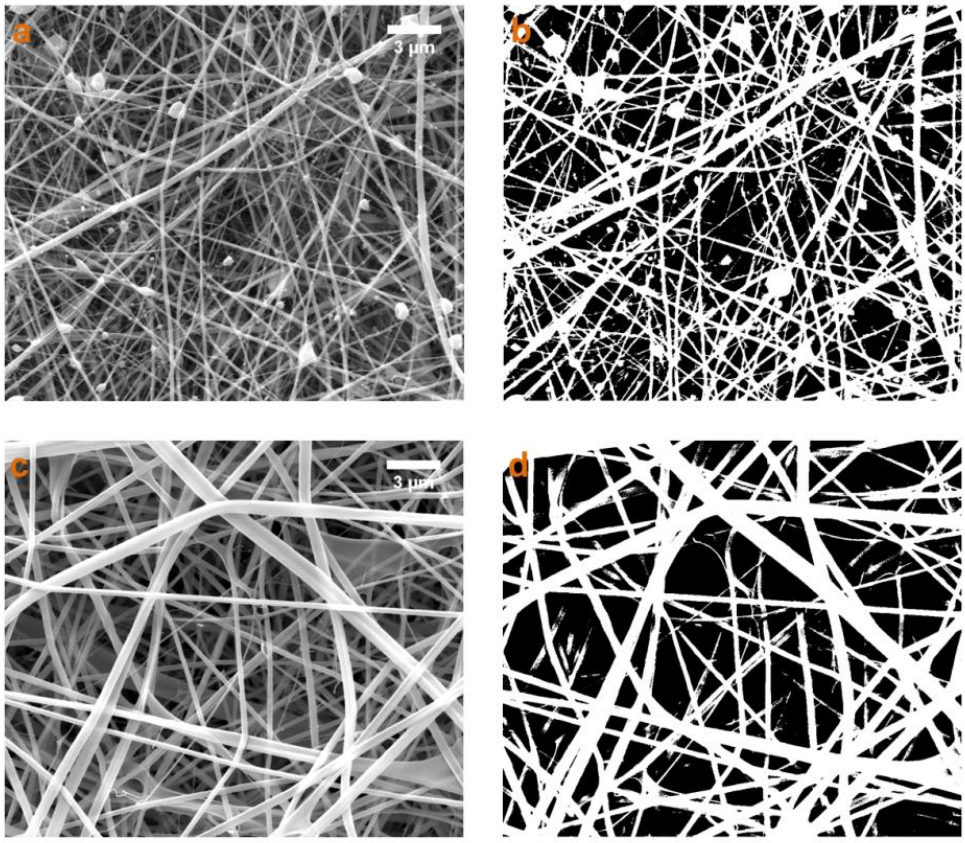

Figure 3.7 SEM images (a, c) and contrast images (b, d) of Nafion nanofibers at 83 wt% Nafion content of the solids in the electrospinning solution fabricated using (a, b) needle electrospinning and (c, d) needleless electrospinning. X 10000 magnification, scale bar = 3 µm.

More specifically, Figure 3.8 shows the stress-strain profiles (mechanical properties) for the needle and needleless electrospun fiber mats and the control film. Tensile strength trends are similar to the Young's modulus, where the needle electrospun fiber mat (0.8 MPa) is lower than the needleless electrospun fiber mat (2.4 MPa) and the film (5.7 MPa) is higher than both electrospun mats. It is expected that the mechanical properties of a dense film would be higher than a porous fiber mat. The elongation-to-break is similar for all samples (6.5% for needle electrospun fiber mat, 10.7% for needleless electropsun fiber mat, and 6.5% for dense film). Thus, needleless electrospinning can produce higher purity defect-free Nafion nanofibers, which

results in improved mechanical properties and liquid-saturated proton conductivity when compared to beaded-fibers from needle electrospinning at a similar composition.

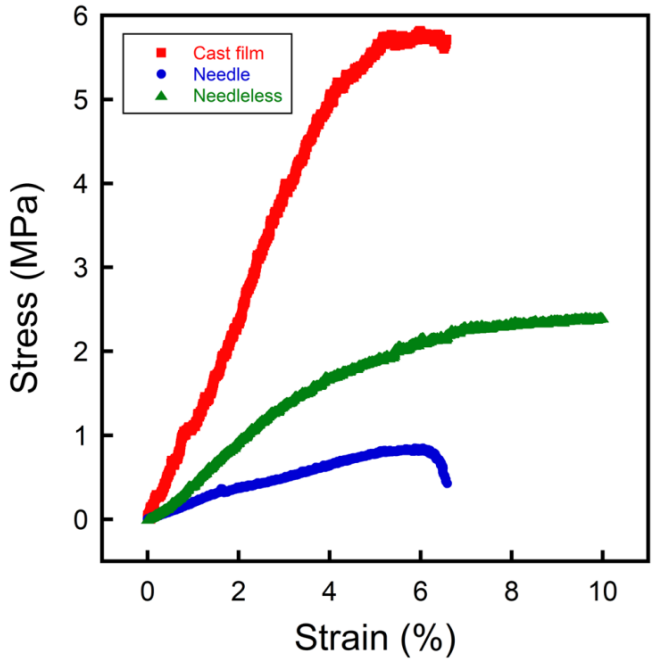

Figure 3.8 Stress-strain profiles for cast film (red squares), needle electrospun nanofiber mat (blue circles), and needleless electrospun nanofiber mat (green triangles).

Figure 3.9a shows the proton conductivity for the needle and needleless electrospun fiber mats and the control film at 90% relative humidity as a function of temperature (ranging from 30 °C to 80 °C). Similar to the results listed in Table 3.1 (submersed in liquid water at room temperature), the proton conductivity at 80 °C and 90% RH for the film (69.9 mS cm^{-1}) is higher than the needleless fiber mat (51.8 mS cm^{-1}), which is higher than the needle electrospun fiber mat (24.4 mS cm^{-1}). However, the cross-sectional area used to calculate conductivity from the impedance data assumes that the entire area is conducting medium, which is only the case for the solid dense film and not the porous fiber mats. In an attempt to normalize the data (*i.e.*, only the area of the conducting solid polymer), an estimated surface area porosity was measured from the SEM

images. The contrast feature in ImageJ was used to distinguish between solid and pores in the mat (see Figures 3.7b and 3.7d, which are contrasts of Figures 3.7a and 3.7c, respectively). From this method, the average void area fractions of the needle and needleless electrospun fiber mats were similar at 53.4% and 52.7%, respectively. These estimated surface area porosities were used to calculate a corrected surface area for the fiber mats (area of only the conducting solid) and subsequently a normalized conductivity. Figure 3.9b shows the normalized proton conductivity of the data shown in Figure 3.9a for the needle and needleless electrospun fiber mats and the control film. Here, the proton conductivity at 80 °C and 90% RH for needleless fiber mat (109 mS cm^{-1}) is higher than the dense film (70 mS cm^{-1}), which is higher than the needle electrospun fiber mat (52 mS cm^{-1}).

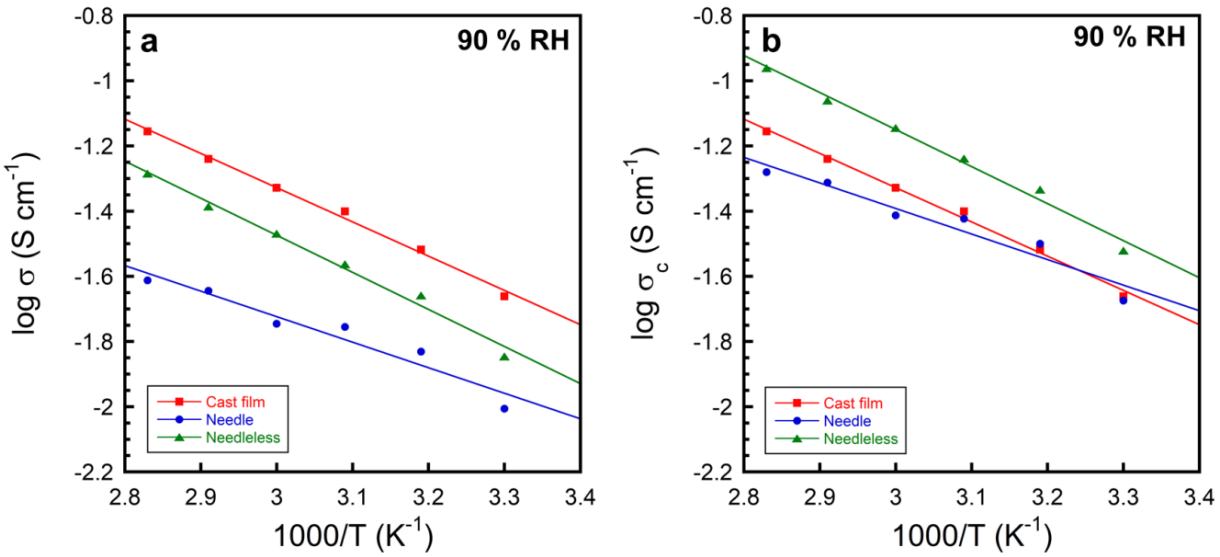

Figure 3.9 (a) Proton conductivity and (b) normalized proton conductivity as a function of temperature at 90% relative humidity for cast film (red squares), needle electrospun nanofiber mat (blue circles), and needleless electrospun nanofiber mat (green triangles). Solid lines represent a regression to the Arrhenius model.

This data is supported by a previous study by Dong *et al.*,[140] which reported on the proton conductivity of a single high-purity Nafion nanofiber at a value that was an order of magnitude higher than a cast Nafion dense film. They attributed this to the high alignment of connected nanoscale ionic network along the fiber axis (supported by small-angle X-ray scattering). The solid lines in Figure 3.9 represent a regression to the Arrhenius equation, where the activation energies were determined to be similar for all samples (8.7 kJ mol^{-1}, 9.4 kJ mol^{-1}, and 6.5 kJ mol^{-1} for film, needleless and needle fiber mat, respectively). These results are similar to other reports of Nafion proton conductivity activation energies.[160] Thus, needleless electrospinning can produce high purity Nafion nanofibers with improved proton conductive properties compared with needle electrospun Nafion nanofibers and solution cast Nafion films.

3.4 Conclusions

In this study, the needleless electrospinning of highly ionic polymer, Nafion, was demonstrated and the results were compared to a classic needle-based electrospinning process. Needleless electrospinning produced Nafion nanofibers (233 ± 62 nm) with similar fidelity to those produced by needle electrospinning (216 ± 69 nm). Needleless electrospinning produced higher purity Nafion nanofibers (98 wt% Nafion) compared to needle electrospinning, where no fibers (only beads) were produced at this similar polymer solution concentration. Needleless electrospinning produced Nafion nanofibers at an order of magnitude higher production rate compared to needle electrospinning (1.00 versus 0.10 mg h^{-1}). Both high productivity and high purity were afforded through the ability of this needleless electrospinning process to generate multiple electrospinning sites that promote chain entanglement for facile electrospinning due to the locally higher polymer concentrations at thin bubble surface solution sites. Also, the Nafion

nanofiber mats produced by needleless electrospinning resulted in enhanced Young's modulus and proton conductivity (42.6 MPa and 43.8 mS cm^{-1}, respectively) compared to those produced with needle electrospinning (20.9 MPa and 18.0 mS cm^{-1}). Overall, this work not only demonstrates the ability to produce high fidelity, high purity Nafion nanofibers at high production rates and improved properties using needleless electrospinning, but also extends the capability of foam electrospinning to highly ionic polymers, while maintaining high fidelity and higher production rates.

CHAPTER IV

ULTRA-LOW PLATINUM FUEL CELL ELECTRODES *VIA* NEEDLELESS ELECTROSPINNING/NEEDLE ELECTROSPRAYING

4.1 Introduction

In Chapter 2, E/E electrodes demonstrated similar power density compared to conventional electrodes at lower Pt loadings, suggesting that E/E is an effective technique to produce high performing ultra-low Pt fuel cell electrodes. Further investigation in varying the Nafion content in the electrospraying solution revealed an optimum (Pt/C)/Nafion ratio in the electrospraying solution due to a balance of mass transfer and proton transfer resistances. In Chapter 3, a needleless electrospinning technique was used to fabricate Nafion nanofibers, which resulted in enhanced mechanical and conductivity properties compared to needle electrospinning due to locally higher polymer concentration at the electrospinning surface. Overall, the goal of shifting from needle to needleless electrospinning is to increase the productivity rate of ultra-low Pt electrode fabrication. Here, in this chapter, the needleless electrospun nanofibers are utilized to produce nanofiber-nanoparticle electrodes using needle electrospraying with the optimum (Pt/C)/Nafion ratio. The morphology and fuel cell performance were investigated and compared to E/E electrodes using the same electrospinning and electrospraying solutions.

4.2 Experimental Methods

4.2.1 Materials

Isopropanol (IPA; ACS reagent, ≥ 99.5%) and poly(acrylic acid) (PAA; M_V = 450,000 g mol^{-1}) were purchased from Sigma-Aldrich. 20 wt% platinum on carbon (Pt/C; Vulcan XC-72) was

purchased from Premetek Co. 1100 EW Nafion solution (5 wt% in 3/1 v/v isopropanol/water) and Nafion membrane (NR-212, 1100 EW (0.91 meq g^{-1}), 0.002 in (~51 μm) dry thickness) were purchased from Ion Power. Gas diffusion layer (GDL; Sigracet 25BC) was purchased from Fuel Cells Etc. All materials were used as received. Deionized (DI) water with a resistivity of 16 MΩ cm was used as appropriate. Ultra-high purity grade nitrogen was purchased from Brazos Valley Welding Supply. Ultra-high purity grade oxygen and ultra-zero grade air were purchased from Airgas. Ultra-high purity grade hydrogen was purchased from Praxair. All gases were used for all fuel cell experiments.

4.2.2 Alternating Needleless Electrospinning/Needle Electrospraying

A needleless electrospinning apparatus, as illustrated in Figure 4.1 (left), consists of a high voltage power supply (ES40P-10W/DAM, Gamma High Voltage Research, Inc.), glass fine-fritted funnel (Pt No. CG-1402-04, Chemglass Life Sciences), circular copper electrode (16 gauge wire), and a grounded collector (9 in x 9 in (23 cm x 23 cm); square cardboard covered with aluminum foil). Compressed air with controlled flow rate was passed through the funnel to produce stable polymeric foam at the top surface of the fritted funnel. A needle electrospraying apparatus, as illustrated in Figure 4.1 (right), consists of a high-voltage power supply (PS/EL50R00.8, Glassman High Voltage, Inc.), syringe pump (NE-1000, New Era Pump Systems), glass syringe (Pt. No. CG-3070-03, Chemglass Life Sciences), syringe needle (i.d. = 0.024 in. (0.603 mm), Hamilton), and poly(vinyl chloride) tubing (Pt. No. 30600-65, Cole-Parmer). Four GDLs (*ca*. 2 cm × 2 cm) were adhered to the collector, where polymer nanofibers and catalyst nanoparticles were electrospun and electrosprayed onto the GDLs *via* alternating between the needleless electrospinning (1 min) and needle electrospraying (5 min), respectively.

The foam surface to collector distance and applied voltage were 15 cm and 15 kV, respectively, for the electrospinning process. The needle tip to collector distance, applied voltage, and solution flow rate were 9 cm, 12 kV, and 3.3 mL h^{-1}, respectively, for the electrospraying processes.

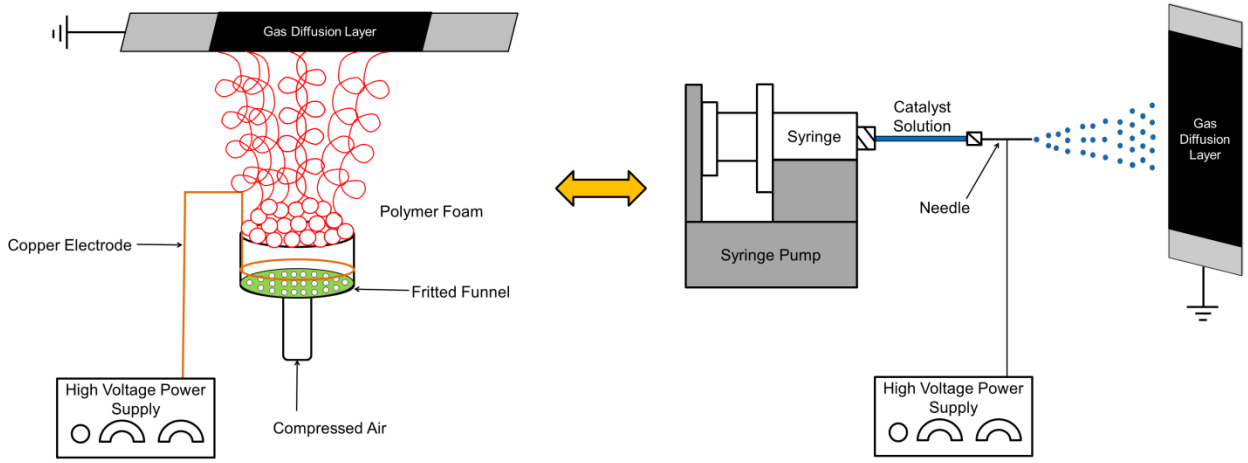

Figure 4.1 Schematic of alternating between needleless electrospinning (left) and needle electrospraying (right) apparatuses.

4.2.3 Electrode and Membrane Electrode Assembly (MEA) Fabrication

The electrospraying catalyst ink solution consisted of a base mixture of 20 mg of Pt/C catalyst, 250 mg of DI water, 400 mg of Nafion solution and 3370 mg of isopropanol. The resulting mixture was sonicated for 3 min at 35% amplitude (Q125, Qsonica) prior to electrospraying. The electrospinning polymer solution was a 5 wt% 4/1 Nafion/PAA polymer solution, *e.g.*, 25 mg of PAA, 2000 mg of Nafion solution, and 485 mg of 3/1 v/v isopropanol/water solution. The solution was stirred under ambient temperature for at least 12 h to ensure complete dissolution of PAA prior to electrospinning. The catalyst ink solution and the polymer solution were used in the electrospraying and electrospinning processes, respectively, to fabricate electrodes as described

in the previous section, For comparison, electrodes were fabricated using the electrospinning/electrospraying (E/E) process described in Chapter 2 using the same electrospinning and electrospraying solutions in this study. Membrane electrode assemblies (MEAs) were fabricated by placing the Nafion NR-212 membrane in between two catalyst-coated GDLs (anode and cathode) and heat pressing (3851-0, Carver) for 5 min at 275 °F (135 °C) and 3200 psi (22 MPa).

4.2.4 Electrode Characterization

The morphology of the E/E electrodes was investigated with scanning electron microscopy (SEM; FEI Quanta 600 FE-SEM, 10 kV) using a working distance of 10 mm. Samples were sputter coated (Cressington 208 HR) with platinum/palladium or iridium (6 nm thickness) prior to SEM analysis. For each image, the diameters of 20 nanofibers and 20 nanoparticles were randomly selected and measured using ImageJ software for each electrode sample.

The Pt loading was measured with thermal gravimetric analysis (TGA; Q50, TA Instrument). A small portion of the electrode (*ca*. 4–7 mg) was heated in the TGA from ambient temperature to 900 °C at 10 °C min^{-1} in air at 60 mL min^{-1}. Since all components in the E/E electrode degrade below 800 °C with the exception of Pt, the Pt loading was determined by dividing the residual weight at 850 °C by the original area of the TGA sample. The average Pt loading for each E/E experiment was determined using 2 samples.

4.2.5 Fuel Cell Tests and Cyclic Voltammetry (CV)

Each MEA (1.21 cm^2 area) was placed between two serpentine flow field graphite plates (1 cm^2 flow area) separated by two 0.152 mm thick PTFE/fiberglass gaskets (Gasket Kit #5,

Scribner Associates, Inc.). The entire fuel cell assembly consisted of an MEA, two gaskets, and two flow plates placed between copper current collectors followed by endplates all held together by bolts with 100 lb in (11.3 N m) of applied torque. Fuel cell performance of each MEA was evaluated with a fuel cell test station (850C, Scribner Associates, Inc.). Fuel cell tests were conducted under ambient pressure with saturated (100% RH) anode and cathode flow rates of 0.43 L min^{-1} hydrogen and 1.02 L min^{-1} oxygen or air, respectively. The stoichiometry of the anode and cathode flow rates used for the fuel cell testing is approximately 1:2 for hydrogen/oxygen and 1:2 for hydrogen/air. The cathode gas, anode gas, and cell temperatures were all maintained at 80 °C. Fuel cell performance was recorded after a new MEA was fully activated. The activation process consists of operating the MEA at 0.7 V for 1 h, followed by 0.6 V, 0.4 V, and 0.2 V for 30 min at each voltage, and ending with two cycles of 0.6 V and 0.4 V for 30 min at each voltage. Polarization curves (cell voltage *versus* current density) were collected from open circuit voltage (OCV) to 0.2 V at increments of 0.05 V min^{-1} to determine that no further increase in current density at a constant voltage was observed, thus the MEA was at steady state. After the MEA was fully activated and reached steady state, four polarization curves were taken to determine the average maximum power density.

Cyclic voltammetry (CV) was performed on a fully activated MEA with a potentiostat (Solartron SI 1287A, Corrware Software) at 20 mV s^{-1} from 0.01 V to 1 V versus NHE under ambient pressure. In this two-electrode configuration, the anode serves as both the counter and reference electrodes. The fuel cell anode and cathode were supplied with 0.04 L min^{-1} hydrogen and 0.02 L min^{-1} nitrogen, respectively. Temperatures of the cathode gas, anode gas, and cell were maintained at 30 °C. The Pt catalyst was assumed to have an average site density of 210 μC cm^{-2}.[110] The electrochemical surface area (ECSA) was determined from the hydrogen adsorption

area from 0.12 to 0.30 V of the CV data. Five cycles were taken to determine the average ECSA for each MEA. Linear sweep voltammetry was performed at 2 mV s^{-1} from OCV to 0.8 V *versus* NHE to determine if the MEA had any defects that resulted from internal shorts or significant hydrogen crossover.

4.3 Results and Discussion

Fuel cell experiments with nanofiber-nanoparticle catalyst layer electrodes using two different techniques were conducted to evaluate the performance of needleless electrospun Nafion/PAA nanofibers on fuel cell performance. SEM images of the E/E catalyst layers are shown in Figure 4.2a–d, where Figure 4.2a,c corresponds to nanofiber-nanoparticle catalyst layers fabricated using the simultaneous electrospinning/electrospraying (E/E) technique (method from Chapter 2) and Figure 4.2b,d corresponds to nanofiber-nanoparticle catalyst layers fabricated using the alternating needleless electrospinning/needle electrospraying (AE/E) technique (method from this Chapter).

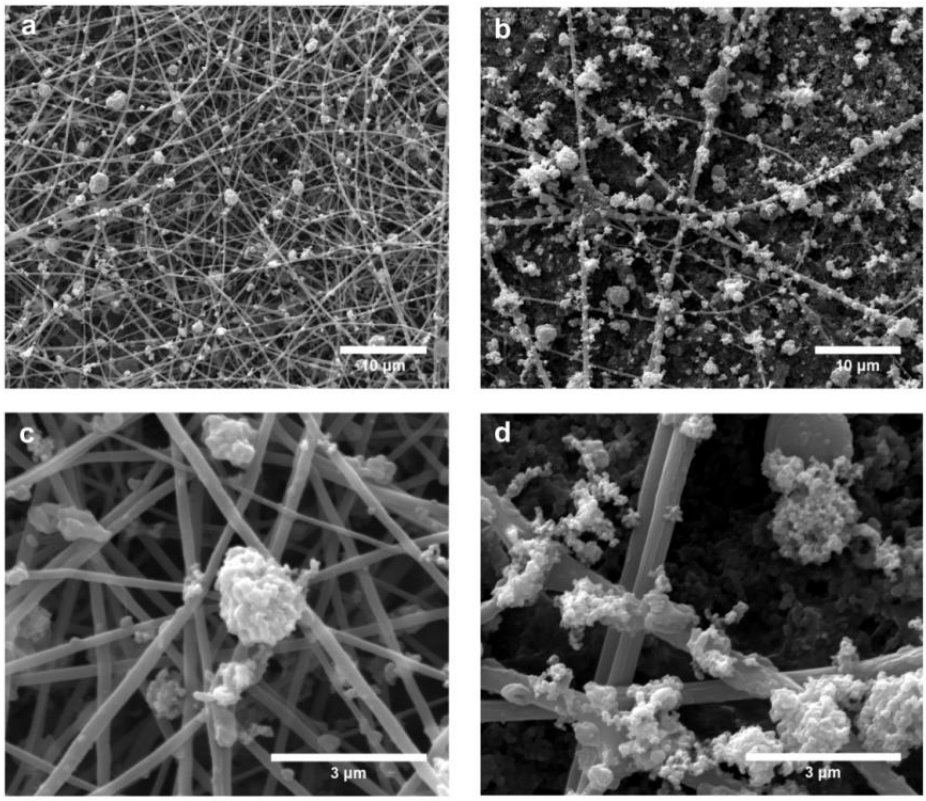

Figure 4.2 SEM images of electrodes fabricated using (a,c) needle electrospinning/electrospraying (E/E) and (b,d) alternating needleless electrospinning/electrospraying (AE/E). (a,b) X 5000 magnification, scale bar = 10 µm; (c,d) X 10000 magnification, scale bar = 3 µm.

The catalyst layers show a highly porous network of randomly arranged nanofibers and particle aggregates, which promotes facile gas transport to Pt sites for reactions to occur. Figure 4.3 shows the average fiber diameters and particle diameters of the images shown in Figure 4.2a–d. The nanofiber-nanoparticle catalyst layers fabricated using the E/E technique visually have a higher fiber density (*i.e.*, number of fibers) compared to the AE/E technique. This difference may be attributed to the E/E technique, which allows for simultaneous deposition of nanofibers and nanoparticles; therefore, allowing fibers to collect for the entire duration of the experiment (*ca.* 1.8 h). On the other hand, the AE/E technique deposits fibers for 1 min every 6 min, which is

equivalent to a total fiber deposition time of 20 min (0.3 h) for the *ca*. 2 h experiment. The average fiber diameters are 218 ± 74 nm and 335 ± 138 nm for E/E and AE/E, respectively. The average fiber diameter for E/E is smaller than that of AE/E which may be due to the rotation of the collector elongating the fiber during the whipping motion before landing on the collector, thereby reducing the fiber diameter. El-Hadi *et al.*[161] also observed a reduction in fiber diameter size between a grounded stationary collecting plate and a rotating collector using poly(3-hydroxybutyrate), where with increasing rotation speed, the fiber diameter reduction was more noticeable. The average particle diameters are 1.13 ± 0.56 µm and 1.63 ± 0.82 µm for E/E and AE/E, respectively. Interestingly, the particle diameter is also smaller for E/E, which suggests that the rotating collector may have an effect on the electrospraying as well.

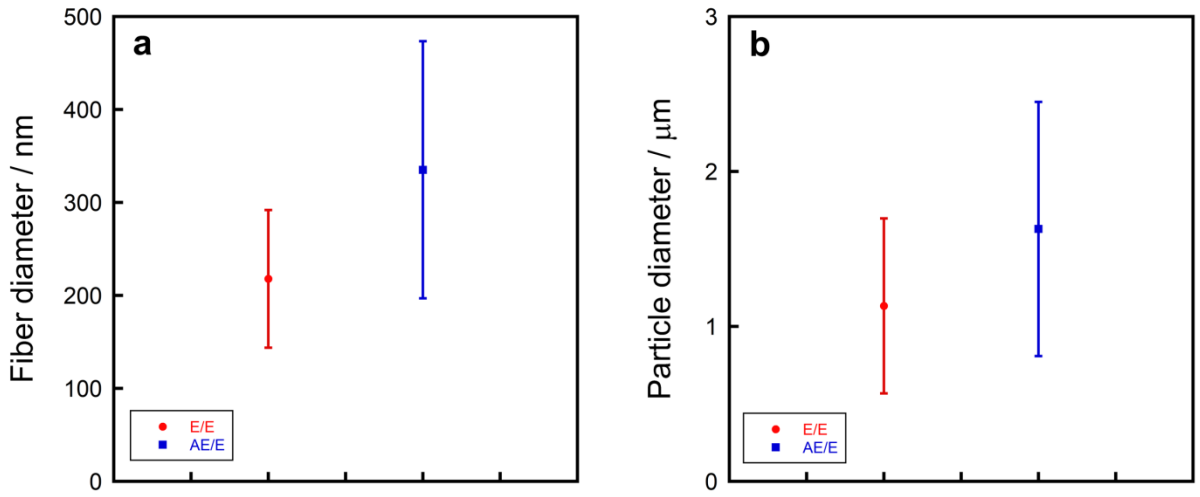

Figure 4.3 (a) Fiber diameter and (b) particle diameter distributions of electrodes fabricated using needle electrospinning/electrospraying (E/E) (red circles) and alternating needleless electrospinning/needle electrospraying (AE/E) (blue squares).

Figure 4.4 shows fuel cell performances (polarization and power curves; hydrogen/oxygen at ambient pressure at 80 °C) for E/E electrodes and for AE/E electrodes. The maximum power density for the E/E electrodes (378 mW cm^{-2}) is lower to that of AE/E electrodes (465 mW cm^{-2}). Two possible reasons for a lower power density may be attributed to the higher fiber density or the low particle-to-fiber ratio in the E/E electrodes as visually observed in Figures 4.2a,c. Higher fiber density may impede gas transport as the fibers are compressed and merged together during the heat press process, which could results in a lower performance. Low particle-to-fiber ratio may also lower electron conductivity as catalyst particles are not as visually well dispersed along the fibers (*i.e.*, poor electron connection). Nevertheless, these results demonstrate similar fuel cell performance for the AE/E electrodes with needleless electrospun fibers as the E/E electrodes shown in Chapter 2 (412–567 mW cm^{-2}), suggesting that the needleless electrospun fibers can produce similar power densities at ultra-low Pt loadings.

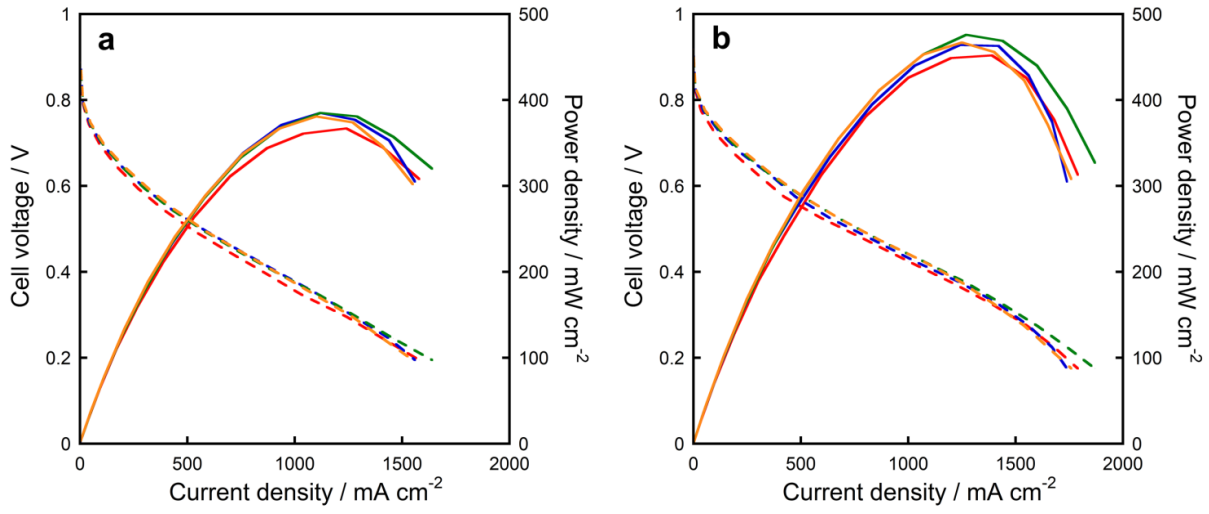

Figure 4.4 Fuel cell polarization curves (dashed) and power density curves (solid) of electrodes fabricated using (a) needle electrospinning/electrospraying (E/E) electrodes with 0.058 mg_{Pt} cm^{-2} and (b) alternating needleless electrospinning/needle electrospraying (AE/E) electrodes with 0.058 mg_{Pt} cm^{-2}. Fuel cell operating conditions: 1/2 mol/mol H_2/O_2 at 80 °C, 100% RH and ambient pressure.

Table 4.1 summarizes these results: maximum power density, average electrode Pt loading, Pt utilization, and electrochemical surface area (ECSA). As mentioned in Chapter 2, the ECSA is a measure of the adsorption or desorption of hydrogen onto the Pt sites; therefore, it is also dependent on the porous structure, electron conductivity, and proton conductivity. The ECSA for the AE/E electrodes (37.7 $m^2\ g_{Pt}^{-1}$) is higher than the E/E electrodes (28.6 $m^2\ g_{Pt}^{-1}$). The increase in the ECSA may be attributed to the increase in gas transport due to a more porous structure or more particle-particle interactions (*i.e.,* higher electron transport) in the AE/E electrodes. Overall, this trend is similar to the trend observed for power density, where AE/E electrodes have higher power density. The Pt utilization (*i.e.*, a measure of platinum use per power gained) is slightly higher for the E/E electrodes (0.31 $mg_{Pt}\ W^{-1}$) and the AE/E (0.25 $mg_{Pt}\ W^{-1}$) electrodes, having similar Pt loadings (0.058 $mg_{Pt}\ cm^{-2}$ for both E/E and AE/E electrodes) and different performances (378 mW cm^{-2} and 465 mW cm^{-2} for E/E and AE/E electrodes, respectively).

Table 4.1 Pt loading, maximum power density, Pt utilization, and electrochemical surface area for electrodes using different electrospinning techniques.

Technique	**Pt loading ($mg_{Pt}\ cm^{-2}$)**	**Max power density[a] ($mW\ cm^{-2}$)**	**Pt utilization[b] ($mg_{Pt}\ W^{-1}$)**	**ECSA[c] ($mg_{Pt}\ cm^{-2}$)**
E/E	0.058	378 ± 11	0.31	28.6 ± 1.3
AE/E	0.058	465 ± 10	0.25	37.7 ± 4.1

[a]Measured at 1/2 mol/mol H_2/O_2 at 80 °C, ambient pressure.
[b]Calclulated using the total Pt loading in the MEA.
[c]Measured at 2/1 mol/mol H_2/N_2 at 30 °C, ambient pressure.

4.4 Conclusions

Needleless electrospun nanofibers were fabricated and employed as nanofiber-nanoparticle catalyst layers in fuel cell electrodes using an alternating needleless electrospinning/needle

electrospraying (AE/E) technique. AE/E electrodes demonstrated a higher maximum power density compared to simultaneous electrospinning/electrospraying (E/E) electrodes in this study, which may be due to the lower fiber/particle ratio. Nevertheless, the results from this study demonstrate that needleless electrospun fibers can be utilized as ultra-low Pt fuel cell electrodes. Future work will work on the development of a new apparatus that utilizes the high production rate of nanofibers from needleless electrospinning to create a simultaneous nanofiber/nanoparticle deposition process similar to the needle E/E in Chapter 2.

CHAPTER V

SULFONATED PENTABLOCK TERPOLYMERS AS MEMBRANES AND IONOMERS IN HYDROGEN FUEL CELLS

5.1 Introduction

Recently, in an effort to find a low-cost alternative to Nafion, investigators have studied sulfonated block copolymers to develop a PEM that has properties similar to Nafion.[162] Ions favor hydrophilic domains (*i.e.,* highly solvated networks); therefore, under hydration, ion transport (*i.e.,* proton conductivity) will increase. However, without a hydrophobic component, the polymer will physically swell with increasing water content, rendering the polymer mechanically unstable. Block copolymers have the unique ability to self-assemble into well-defined nanostructures, allowing for specified tuning of different properties on the nanoscale level. Therefore, non-ionic blocks and ionic blocks can be seamlessly combined into one polymer with the orthogonal properties of mechanical strength and ionic conductivity.

Recently, a commercially available sulfonated pentablock terpolymer has been studied and characterized *ex situ* as a solution[163-165] and membrane.[165-170] Choi *et al.*[167] reported that changing the ion exchange capacity (*i.e.,* degree of sulfonation) of pentablock terpolymers can alter the nanoscale morphology which can significantly affect mechanical properties. Fan *et al.*[166] suggested that liquid, gas, and ion transport are correlated with IEC (*i.e.,* all transport properties increase with IEC) for these sulfonated pentablock terpolymers, demonstrating a conductivity of 0.099 S cm^{-1} at 30 °C in liquid water for an IEC of 2.0 meq g^{-1}. These studies suggest that these sulfonated pentablock terpolymers can be used as membranes and ionomers in PEMFC applications. Huang *et al.*[171] investigated the fuel cell performance using a sulfonated pentablock

terpolymer as the membrane and reported a maximum power density of 160 mW cm^{-2} with a high frequency resistance of 6.4 Ω cm^2. However, the effect of the sulfonated pentablock terpolymer as an ionomer in a fuel cell has yet to be determined. Here, in this chapter, a series of sulfonated pentablock terpolymers (same polymer backbone, but different IECs) are investigated and compared to Nafion. Their properties and fuel cell performances are evaluated, and insight into tuning optimum performance for these sulfonated pentablock terpolymers as a membrane and ionomer in PEMFC applications is provided.

5.2 Experimental Methods

5.2.1 Materials

An ABCBA pentablock terpolymer, poly(tbS-*b*-HI-*b*-S/sS-*b*-HI-*b*-tbS), also known as NEXAR, was synthesized and provided by Kraton Performance Polymers and contains outer A blocks of tert-butyl-styrene (tbS), B blocks of hydrogenated isoprene (HI) and an inner C block of partially sulfonated styrene (S/sS) (chemical structure shown in Figure 5.1). The unsulfonated ABCBA pentablock terpolymer has a $M_n \approx 68$ kg mol^{-1} with M_n of respective blocks equal to 14-8.5-23-8.5-14 kg mol^{-1}. This NEXAR was received as three different partially sulfonated polymers, each with different ion exchange capacities (IECs: 2.0, 1.5, and 1.0 meq g^{-1}). NEXAR with an IEC of 2.0 meq g^{-1} (NEXAR-2.0) was received as a 10 wt% solution in 2/1 w/w toluene/1-propanol. NEXAR with an IEC of 1.5 meq g^{-1} (NEXAR-1.5) and 1.0 meq g^{-1} (NEXAR-1.0) were both received as a 20 wt% solution in 2/1 w/w 1-propanol/toluene. Isopropanol (ACS reagent, ≥ 99.5%), 1-propanol (ACS reagent, ≥ 99.5%), and toluene (anhydrous, ≥ 99.8%) were purchased from Sigma-Aldrich. 20 wt% platinum on carbon (Pt/C; Vulcan XC-72) was purchased from Premetek Co. Gas diffusion layer (GDL; Sigracet 25BC)

was purchased from Fuel Cells Etc. 1100 EW Nafion solution (5 wt% in 3/1 v/v isopropanol/water) and Nafion membranes (NR-211 and NR-212, 26 and 51 μm dry thicknesses, respectively, both at 1100 EW (0.9 meq g^{-1})) were purchased from Ion Power. Mylar PET release liner film (Grade 26965, 0.0762 mm thickness) was purchased from LOPAREX. All materials were used as received. Deionized (DI) water with a resistivity of 16 MΩ cm was used as appropriate. Ultra-high purity grade nitrogen was purchased from Brazos Valley Welding Supply. Ultra-high purity grade oxygen was purchased from Airgas. Ultra-high purity grade hydrogen was purchased from Praxair. All gases were used for all fuel cell experiments.

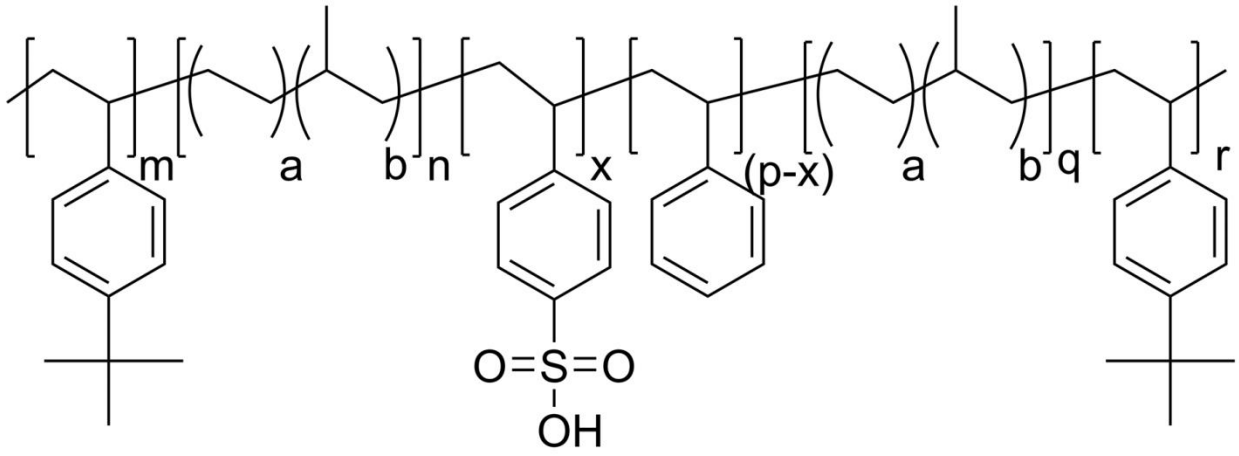

Figure 5.1 Chemical structure of NEXAR (sulfonated pentablock terpolymer).

5.2.2 NEXAR Membrane Preparation

NEXAR dense films or membranes were fabricated by casting the NEXAR solutions onto a silicon-coated Mylar PET film using an automatic film applicator (Elcometer 4340) with a doctor blade gauge height and speed of 300–500 μm and 90 mm s^{-1}, respectively, under ambient conditions. Polymer solutions were partially covered with aluminum foil and solvents were

allowed to evaporate under ambient conditions for at least 12 h before use. The final film thicknesses were *ca.* 30–40 μm measured with a digital micrometer (Marathon; Pt No. CO030025, accuracy = 2 μm). The values recorded are averages of five measurements for each sample. For conductivity and stress-strain measurements, membranes were cut into rectangular pieces (*ca.* 30 mm (L) x 10 mm (W) and *ca.* 25 mm (L) x 5 mm (W), respectively). For MEA fabrication, membranes were cut into square pieces (*ca.* 20 mm (L) × 20 mm (W)).

5.2.3 NEXAR Membrane Characterization

Mechanical properties of the membranes (*ca.* 25 mm (L) x 0.5 mm (W)) were measured with dynamic mechanical analysis (DMA; Q800, TA Instruments) under the given conditions: 22 ± 2 °C, 40 ± 5% RH and a strain ramp rate of 0.1% min^{-1}. Stress-strain profiles were collected for each sample. The Young's modulus was measured from the initial slope of the stress-strain curve.

Water uptake was measured with dynamic vapor sorption (DVS; TA Instruments Q5000). A dry film sample was first loaded into the DVS and preconditioned at 0% RH and 60 °C until equilibrium was established to remove any residual water in the sample; equilibrium was reached when < 0.1 wt% change was observed for at least 30 min. The temperature was then systematically changed to 30 °C, 40 °C, 50 °C, and 60 °C at a fixed relative humidity at 90% RH, equilibrating at each condition. The polymer water vapor uptake (WU_{vapor}) was calculated using the following equation: $WU_{vapor} = (W-W_0)/W_0$, where W_0 and W are dry and wet polymer weights measured before and after each DVS experimental condition, respectively.

Proton conductivity of the membranes (*ca.* 3 cm (L) x 1 cm (W)) was measured with electrochemical impedance spectroscopy (EIS; Solartron SI 1260A) in a four-point conductivity

cell (BekkTech BT112, Scribner Associates, Inc.) by sweeping frequencies from 1 MHz to 0.05 Hz with an amplitude of 10 mV under different temperatures ranging from 30 °C to 80 °C at 90% RH and under different relative humidities from 30% RH to 90% RH at 60 °C. The temperature and relative humidity were controlled by placing the four-point conductivity cell in a bench top environmental chamber (ESPEC). The data was analyzed by determining the high-frequency intercept of the real impedance, *R*, which was measured between the two inner reference electrodes. Conductivity was calculated by using the following equation: $\sigma = L/(AR)$, where *L* is the distance between the two inner electrodes (*ca.* 0.48 mm) and *A* is the cross-sectional area of the sample ($A = Wl$; *W* is the sample width and *l* is the sample thickness). Samples were allowed to equilibrate for 1 h at each temperature at 90% RH and for 2 h at each relative humidity at 60 °C followed by five repeated measurements. The reported values are the averages of these repeated measurements at each condition.

To investigate the effect of fuel cell conditions (*i.e.,* elevated pressure, gas flow, temperature and water), on NEXAR-1.0 membrane properties, a NEXAR-1.0 membrane (*ca.* 3 cm x 3 cm) was pretreated in the fuel cell assembly by applying the same torque (100 lb in) as the MEAs and operating under 80 °C, 100% RH with nitrogen flowing through at 0.42/1.01 L min^{-1} for anode/cathode flow rates, respectively, for 6 h (approximate time for activation and polarization curve collection), prior to conductivity measurements. The proton conductivity of a portion of this treated membrane (*ca.* 3 cm (L) x 1 cm (W)) was measured after the pretreatment.

5.2.4 Nafion Electrode (Conventional Electrode) Fabrication

Conventional (control) electrodes were prepared by mixing 100 mg of Pt/C catalyst, 550 mg of DI water, 1000 mg of Nafion solution, and 1350 mg of isopropanol, which corresponds to 2/1

w/w (Pt/C)/Nafion in 3/1 v/v isopropanol/water. The mixture was sonicated for 3 min at 35% amplitude (Q125, Qsonica) and subsequently brushed onto the GDL (*ca.* 20 mm (L) x 20 mm (W)) with an ox hair brush (0689-00025, Gordon Brush Mfg. Co., Inc.). This process was repeated to achieve the target Pt loading of *ca.* 0.20/0.50 mg_{Pt} cm^{-2} for the anode/cathode Pt loadings, respectively.

5.2.5 NEXAR Electrode Fabrication

The catalyst ink solution used to fabricate NEXAR electrodes consisted of a mixture of Pt/C catalyst, NEXAR polymer as the ionomer, toluene, and isopropanol. The amount of toluene and isopropanol were adjusted to match the weight ratio as the original NEXAR solution. The NEXAR catalyst ink solution corresponds to 2/1 w/w (Pt/C)/NEXAR. The solids weight percent was kept constant at 1 wt% for all catalyst ink solutions. The mixture was sonicated for 3 min at 35% amplitude (Q125, Qsonica) and subsequently brushed onto the GDL (*ca.* 20 mm (L) x 20 mm (W)) with an ox hair brush (0689-00025, Gordon Brush Mfg. Co., Inc.).

For the systematic study of (Pt/C)/ionomer and 1-propanol/water ratios, the amount of Pt/C catalyst, dry solid NEXAR-1.0 ionomer, 1-propanol and water were adjusted to achieve (Pt/C)/ionomer ratios of 1/1, 2/1, and 4/1 and 1-propanol/water ratios of 2/1, 1/1, 1/2, and 0/1. The resulting mixture was sonicated for 3 min at 35% amplitude (Q125, Qsonica) prior to airbrushing with an airbrush gun (AEROPRO1, Aeroblend) on a GDL substrate (*ca.* 15 mm (L) x 15 mm (W)) on a hot plate heated to 120 °C. The airbrushing process was repeated to achieve the desired target Pt loading.

5.2.6 Electrode Characterization

The morphology of the electrodes was investigated with scanning electron microscopy (SEM; FEI Quanta 600 FE-SEM, 10 kV) using a working distance of 10 mm. Samples were sputter coated (Cressington 208 HR) with iridium (6 nm thickness) prior to SEM analysis.

The Pt loading was measured with thermal gravimetric analysis (TGA; Q50, TA Instrument). A small portion of the electrode (*ca.* 4–6 mg) was heated in the TGA from ambient temperature to 900 °C at 10 °C min^{-1} in air at 60 mL min^{-1}. Since all components in the electrode degrade below 800 °C with the exception of Pt, the Pt loading was determined by dividing the residual weight at 850 °C by the original area of the TGA sample.

5.2.7 Membrane Electrode Assembly (MEA) and Fuel Cell Tests

Membrane electrode assemblies (MEAs) were fabricated by placing the membrane in between two catalyst-coated GDLs (anode and cathode) and heat pressing (3851-0, Carver) for 5 min at 80 °C and 22 MPa. Each MEA (1.21 cm^2 area) was placed between two serpentine flow field graphite plates (1 cm^2 flow area) separated by two 0.152 mm thick PTFE/fiberglass gaskets (Gasket Set #5, Scribner Associates, Inc.). The entire fuel cell assembly consisted of an MEA, two gaskets, and two flow plates placed between copper current collectors followed by endplates all held together by bolts with 2.8 N m of applied torque. Fuel cell performance of each MEA was evaluated with a fuel cell test station (850C, Scribner Associates, Inc.). Fuel cell performance tests were conducted under ambient pressure with saturated (100% RH) anode and cathode flow rates of 0.43 L min^{-1} hydrogen and 1.02 L min^{-1} oxygen, respectively. The stoichiometry of the anode and cathode flow rates used for the fuel cell testing is approximately 1:2 for hydrogen/oxygen. The cathode gas, anode gas, and cell temperatures were all maintained

at 30 °C. Fuel cell performance was recorded after a new MEA was fully activated. The activation process consists of operating the MEA at 0.7 V for 1 h, followed by 0.6 V, 0.4 V, and 0.2 V for 30 min at each voltage, and ending with two cycles of 0.6 V and 0.4 V for 30 min at each voltage. Polarization curves (cell voltage *versus* current density) were collected from open circuit voltage (OCV) to 0.2 V at increments of 0.05 V min^{-1} to determine that no further increase in current density at a constant voltage was observed, thus the MEA was at steady state. After the MEA was fully activated and reached steady state, three to five polarization curves were taken to determine the average maximum power density. Then, the cathode gas, anode gas, and cell temperatures were systematically changed to 40 °C, 50 °C, 60 °C, 70 °C, and 80 °C and equilibrated at each temperature for 15 min prior to taking three to five polarization curves to determine the average maximum power density at each temperature.

Fuel cell tests under different relative humidity were conducted under back pressure of 1.7 MPa and a constant cell temperature of 80 °C. The cell relative humidity was systematically changed to 90% RH, 60% RH, and 30% RH by changing the anode/cathode gas temperatures to 77/77 °C, 68/68 °C, and 53/53 °C, respectively. The fuel cell was equilibrated at each condition for 15 min prior to taking five polarization curves to determine the average maximum power density at each cell relative humidity.

5.2.8 Electrochemical Impedance Spectroscopy (EIS)

Electrochemical impedance spectroscopy (EIS; Solartron SI 1260A) was performed after the fuel cell tests from 1 MHz to 1 Hz at 0.6 V *versus* NHE under back pressure of 1.7 MPa. In this two-electrode configuration, the anode serves as both the counter and reference electrodes. The fuel cell anode and cathode were supplied with 0.43 L min^{-1} hydrogen and 1.02 L min^{-1} oxygen,

respectively. The stoichiometry of the anode and cathode flow rates used for the fuel cell testing is approximately 1:2 for hydrogen/oxygen. The EIS data was analyzed using a common equivalent circuit model that consisted of a resistor (resistance of the solid electrolyte membrane) in series with a parallel circuit of a constant phase element and a second resistor (resistance of the catalyst layer) that is typically used to describe a porous electrode.[111] The resistance reported here is the resistance of the solid electrolyte membrane.

5.3 Results and Discussion

Figure 5.2a shows the temperature-dependent (ranging from 30–80 °C) proton conductivity at 90% RH for the NEXAR and Nafion NR-212 membranes. The conductivities of all membranes increase with increasing temperature. At a lower temperature (30 °C), all NEXAR membranes (0.09, 0.15, and 0.14 S cm^{-1} for NEXAR-1.0, -1.5, and -2.0, respectively) are almost one order of magnitude higher than Nafion NR-212 (0.02 S cm^{-1}). At a higher temperature (80 °C), all NEXAR membranes (0.22, 0.34, and 0.30 S cm^{-1} for NEXAR-1.0, -1.5, and -2.0, respectively) are 2-fold higher than Nafion NR-212 (0.14 S cm^{-1}). Surprisingly, NEXAR-2.0 and NEXAR-1.5 have similar proton conductivities (0.23 and 0.25 S cm^{-1}, respectively, at 60 °C) at all temperatures, suggesting that there is a maximum limit in proton conductivity, regardless of degree of sulfonation or IEC. Interestingly, at all temperatures, NEXAR-1.0 has a higher proton conductivity than Nafion NR-212, where both have a similar IEC.

Figure 5.2b shows the humidity-dependent (ranging from 30–90% RH) proton conductivity at 60 °C for the NEXAR and Nafion NR-212 membranes. As expected, the conductivity of all membranes increases several orders of magnitude from 30 to 90% RH due to a water-assisted proton transport mechanism. At 30% RH, the conductivity of NEXAR-1.0 (3.9×10^{-4} S cm^{-1}) is

lower than Nafion NR-212 (6.2 x 10^{-4} S cm^{-1}), while the conductivities of NEXAR-1.5 (5.6 x 10^{-4} S cm^{-1}) and NEXAR-2.0 (8.0 x 10^{-4} S cm^{-1}) are comparable and higher, respectively, than Nafion NR-212. At 90% RH, the conductivities of all NEXAR membranes (13.8 x 10^{-2}, 21.3 x 10^{-2}, and 22.2 x 10^{-2} S cm^{-1} for NEXAR-1.0, -1.5, and -2.0, respectively) are higher than Nafion NR-212 (9.7 x 10^{-2} S cm^{-1}). Overall, these results suggest that NEXAR membranes have sufficient proton conductivity to translate into high power density hydrogen fuel cell performance.

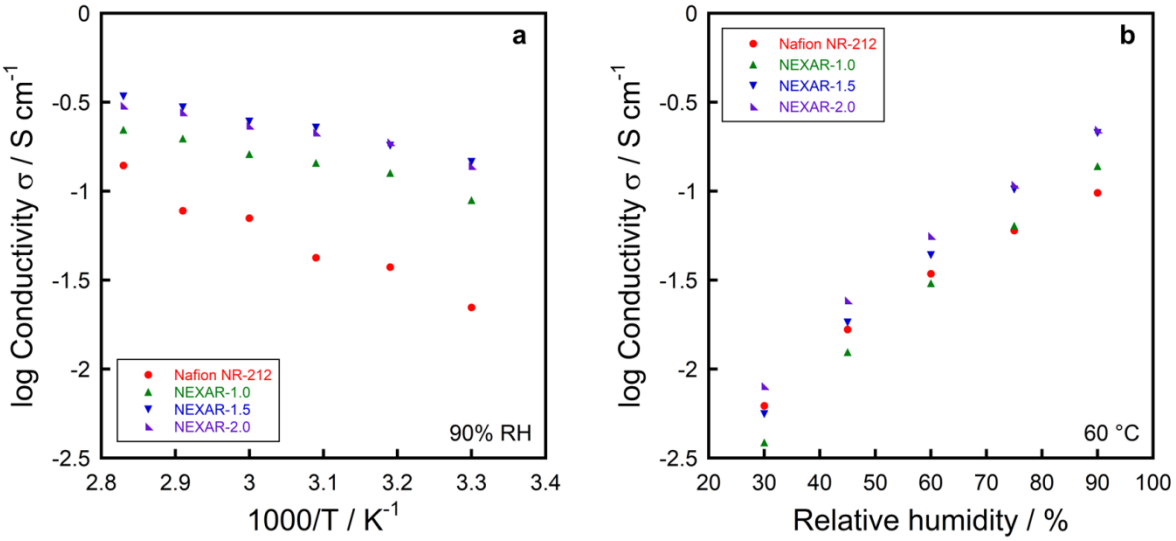

Figure 5.2 (a) Temperature-dependent proton conductivity at 90% RH and (b) humidity-dependent proton conductivity at 60 °C for Nafion NR-212 (red circles) and NEXAR membranes (with different IECs (meq g^{-1}): 1.0 (green upward triangles), 1.5 (blue downward triangles), 2.0 (purple right triangles)).

The temperature-dependent conductivity data in Figure 5.2a was regressed to the Arrhenius equation to determine the activation energies. Table 5.1 lists the activation energies along with IECs, dry film thickness, vapor water uptake, and Young's modulus for all NEXAR and Nafion NR-212 membranes. The activation energies of all NEXAR membranes (5.7, 6.4, and 6.7 kJ mol^{-}

[1] for NEXAR-1.0, -1.5, and -2.0, respectively) are lower than that of Nafion NR-212 (13.0 kJ mol^{-1}); similar to those reported in literature (10 ± 2 kJ mol^{-1}).[160] The Young's modulus of all NEXAR membranes (427, 419, and 288 MPa for NEXAR-1.0, -1.5, and -2.0, respectively) are higher than that of Nafion (142 MPa), which suggests that the NEXAR materials are stronger in tensile strength but not as elastic compared to Nafion. The vapor water uptakes of NEXAR membranes (21.3, 29.0, and 38.9 wt% for NEXAR-1.0, -1.5, and -2.0, respectively) are higher than that of Nafion (9.9 wt%).

Table 5.1 Properties of membranes.

Material	IEC (meq g^{-1})	Film dry thickness (μm)	Young's modulus[a] (MPa)	WU_{vapor}[b] (%)	σ[b] (S cm^{-1})	E_a[c] (kJ mol^{-1})
Nafion NR-212	0.9	55	142	9.9	0.07	13.0
NEXAR-1.0	1.0	37	427	21.3	0.16	6.7
NEXAR-1.5	1.5	38	419	29.0	0.25	6.4
NEXAR-2.0	2.0	30	288	38.9	0.23	5.7

[a]Measured under ambient conditions: 22 ± 1 °C, 45 ± 5% RH.
[b]Measured under 60 °C, 90% RH.
[c]Calculated from the Arrhenius regression of temperature-dependent proton conductivity under 90% RH.

Figure 5.3 shows the maximum power densities under different operating temperatures (obtained from hydrogen/oxygen fuel cell polarization curves at ambient pressure, 100% RH) of MEAs with either NEXAR membranes or Nafion NR-212/NR-211 membranes and Nafion ionomer in the electrodes (control) (*i.e.*, MEAs (membrane/ionomer): Nafion NR211/Nafion, Nafion NR-212/Nafion, NEXAR-1.0/Nafion, NEXAR-1.5/Nafion, NEXAR-2.0/Nafion). The maximum power densities of Nafion NR-211/Nafion, Nafion NR-212/Nafion, and NEXAR-1.0/Nafion MEAs increase with increasing temperature over the entire temperature range (30–80

°C), where at 30 °C, Nafion NR-211/Nafion (262 mW cm^{-2}) is higher than Nafion-NR212/Nafion (189 mW cm^{-2}) and NEXAR-1.0/Nafion (223 mW cm^{-2}), and at 80 °C, Nafion NR-211/Nafion (547 mW cm^{-2}) is higher than Nafion-NR212/Nafion (421 mW cm^{-2}) and NEXAR-1.0/Nafion (368 mW cm^{-2}). As expected, the maximum power density of the Nafion NR-211/Nafion MEA is consistently higher than that of Nafion NR-212/Nafion MEA, *i.e.*, a thinner membrane (26 and 51 μm for NR-211 and NR-212, respectively) results in lower membrane resistance and therefore higher fuel cell performance. NEXAR-2.0/Nafion MEA reaches its highest maximum power density (646 mW cm^{-2}) at 50 °C and decreases at the higher temperature range (60–80 °C). NEXAR-1.5/Nafion MEA reaches its highest maximum power density (452 mW cm^{-2}) at 60 °C and decreases at the higher temperature range (70–80 °C). These results suggest NEXAR-2.0 and NEXAR-1.5 membranes are not thermally stable at the higher temperature ranges. However, NEXAR-1.0 membrane shows thermally stability across the entire temperature range (30–80 °C) under fuel cell operation and comparable power densities to NR-212, suggesting that the NEXAR-1.0 may be a good candidate as a PEM for hydrogen fuel cells.

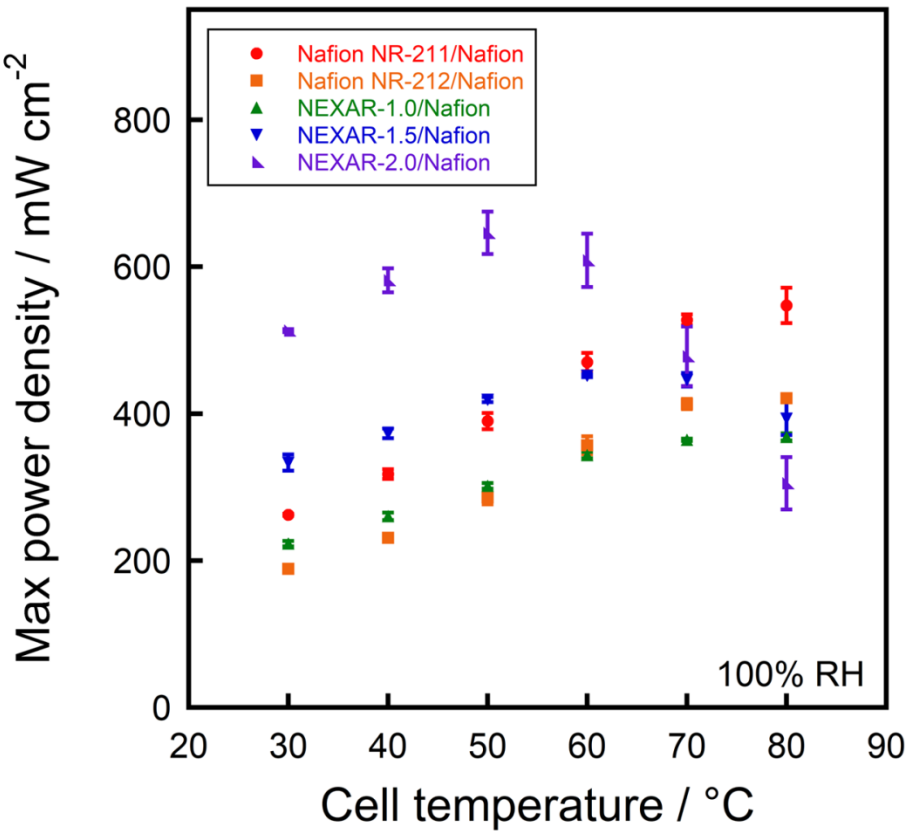

Figure 5.3 Maximum fuel cell power densities at various temperatures of MEAs (membrane/ionomer): Nafion NR-211/Nafion (red circles), Nafion NR-212/Nafion (orange squares), and NEXAR-1.0/Nafion (green upward triangles), NEXAR-1.5/Nafion (blue downward triangles), and NEXAR-2.0/Nafion (purple right triangles). Fuel cell operating conditions: 1/2 mol/mol/ H_2/O_2 at 100% RH, and ambient pressure.

Figure 5.4 shows the maximum power densities under different operating temperatures (obtained from hydrogen/oxygen fuel cell polarization curves at ambient pressure, 100% RH) of MEAs with either NEXAR membranes or Nafion NR-212/NR-211 membranes and the same polymer ionomer in the electrodes as the membrane (*i.e.,* MEAs (membrane/ionomer): Nafion NR211/Nafion, Nafion NR-212/Nafion, NEXAR-1.0/NEXAR-1.0, NEXAR-1.5/NEXAR-1.5, NEXAR-2.0/NEXAR-2.0). The Nafion NR-212/Nafion and Nafion NR-211/Nafion MEAs are the same as those shown in Figure 5.3. The maximum power densities of all MEAs increase with

increasing temperature. At 30 °C, NEXAR-1.0/NEXAR-1.0 (147 mW cm^{-2}) is higher than NEXAR-1.5/NEXAR-1.5 (79 mW cm^{-2}) and NEXAR-2.0/NEXAR-2.0 (97 mW cm^{-2}), and at 80 °C, NEXAR-1.0/NEXAR-1.0 (181 mW cm^{-2}) is higher than NEXAR-1.5/NEXAR-1.5 (114 mW cm^{-2}) and NEXAR-2.0/NEXAR-2.0 (174 mW cm^{-2}). The maximum power density of NEXAR-1.0/NEXAR-1.0 MEA is consistently higher than that of the other higher IEC NEXAR MEAs, which suggests that NEXAR-1.0 is more stable as an ionomer in the electrodes. Table 5.2 lists the power density results and catalyst loadings for all MEAs in this study.

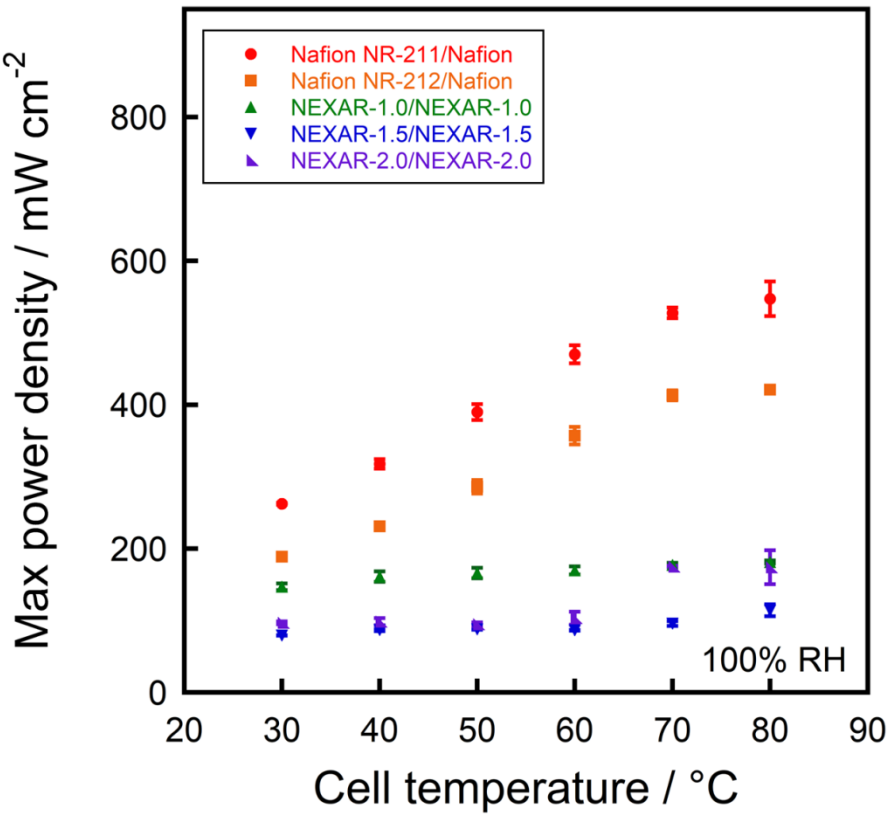

Figure 5.4 Maximum fuel cell power densities at different temperatures of MEAs (membrane/ionomer): Nafion NR-211/Nafion (red circles), Nafion NR-212/Nafion (orange squares), NEXAR-1.0/NEXAR-1.0 (green upward triangles), NEXAR-1.5/NEXAR-1.5 (blue downward triangles), and NEXAR-2.0/NEXAR-2.0 (purple right triangles). Fuel cell operating conditions: 1/2 mol/mol/ H_2/O_2 at 100% RH and ambient pressure.

Table 5.2 Catalyst loading and fuel cell performance of MEAs.

Membrane	**Ionomer**	**Pt loading[a] (mg_{Pt} cm^{-2})**	**Max power density[b] (mW cm^{-2})**
Nafion NR-211	Nafion	0.20/0.77	547 ± 24
Nafion NR-212	Nafion	0.20/0.62	421 ± 2
NEXAR-1.0	Nafion	0.23/0.68	368 ± 5
NEXAR-1.5	Nafion	0.23/0.51	393 ± 23
NEXAR-2.0	Nafion	0.14/0.45	305 ± 36
NEXAR-1.0	NEXAR-1.0	0.19/0.52	181 ± 2
NEXAR-1.5	NEXAR-1.5	0.25/0.55	114 ± 8
NEXAR-2.0	NEXAR-2.0	0.21/0.57	174 ± 24

[a]Anode/cathode catalyst loading, respectively.
[b]Measured at 1/2 mol/mol H_2/O_2 at 80 °C, 100% RH, and ambient pressure.

Figures 5.5a–c show images of the NEXAR/NEXAR MEAs before fuel cell testing. The MEAs are pristine before testing with no distinct discolorations or tears in the membranes from heat-pressing. *Post mortem* analysis (images of MEAs after fuel cell testing) of the NEXAR-1.5/NEXAR-1.5 and NEXAR-2.0/NEXAR-2.0 MEAs, shown in Figure 5.5e–f, shows distinct tears at the membrane-electrode boundary, whereas the NEXAR-1.0/NEXAR-1.0 MEA, shown in Figure 5.5d, is still pristine. This suggests that during fuel cell operation, NEXAR-1.0/NEXAR-1.0 is thermally and mechanically stable. These results are supported by the power density results shown in Figs. 3 and 4, where MEAs with NEXAR-1.0 as a membrane and an ionomer perform better than MEAs with NEXAR-1.5 or NEXAR-2.0 at higher temperatures even though it has a lower IEC. Therefore, the remainder of this study will focus on NEXAR-1.0.

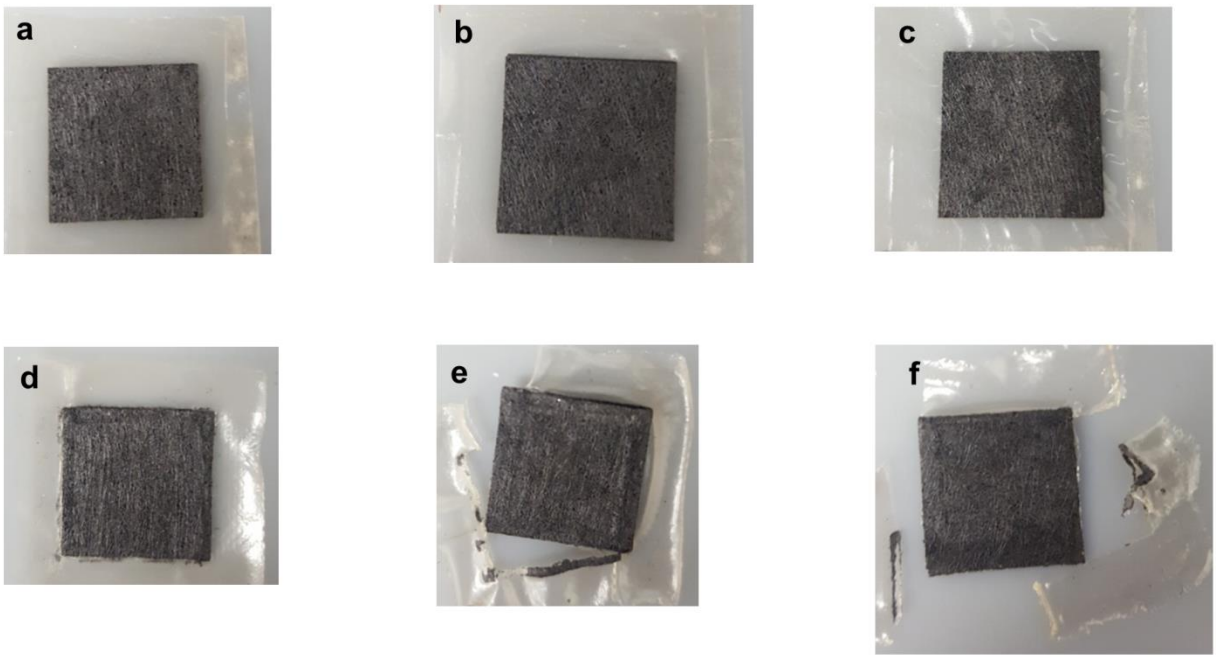

Figure 5.5 Still images of NEXAR/NEXAR MEAs (a-c) before and (d-f) after fuel cell testing; different IECs (meq g^{-1}): (a,d) 1.0, (b,e) 1.5, and (c,f) 2.0.

To understand the impact of the NEXAR-1.0 ionomer on fuel cell performance, the compositions of the ionomer and solvent ratios in the catalyst ink solution were varied. Figure 5.6 shows fuel cell performances (hydrogen/oxygen fuel cell polarization and power curves at ambient pressure at 80 °C, 100% RH) for NEXAR-1.0/NEXAR-1.0 MEAs with electrodes fabricated with different catalyst/NEXAR-1.0 ionomer ratios in the catalyst ink solution. At low ionomer content (4/1 w/w (Pt/C)/ionomer), the maximum power density is 163 mW cm^{-2} and the polarization curve exhibits erratic behavior at higher current densities. At higher ionomer content (2/1 w/w (Pt/C)/ionomer), the maximum power density is 318 mW cm^{-2}, which is a 95% gain in power output. Further increase in ionomer content (1/1 w/w (Pt/C)/ionomer) decreases the power density to 232 mW cm^{-2}, which is a 27% loss in power output. These results suggest that sufficient ionomer content is required to provide proton conduction between catalyst particle

aggregates and membrane to maintain high power density. Studies on the effect of the Nafion content in the catalyst layer show that the Nafion content has a simultaneous impact on both the ionomer and pore network.[18-22] Passalacqua *et al.*[19] demonstrated that at low ionomer content, there is a loss of ionomer connectivity and subsequently proton conductivity or transport (*i.e.*, increases charge resistance), which lowers fuel cell performance. At higher ionomer contents, Uchida *et al.*[21] showed that pore volume decreases and blocks O_2 gas from reaching Pt reaction sites (*i.e.*, increases mass transfer resistance), which also lowers fuel cell performance. Therefore, multiple studies have reported that the optimum Nafion content is around 30 wt% ionomer content in the electrodes due to a balance between proton transfer and mass transfer resistances.[19, 122-123, 172] Interestingly, the optimum NEXAR-1.0 content (33 wt%) is similar to the optimum Nafion content (~30 wt%), suggesting that NEXAR-1.0 as an ionomer behaves similarly to Nafion ionomer in fuel cell electrodes.

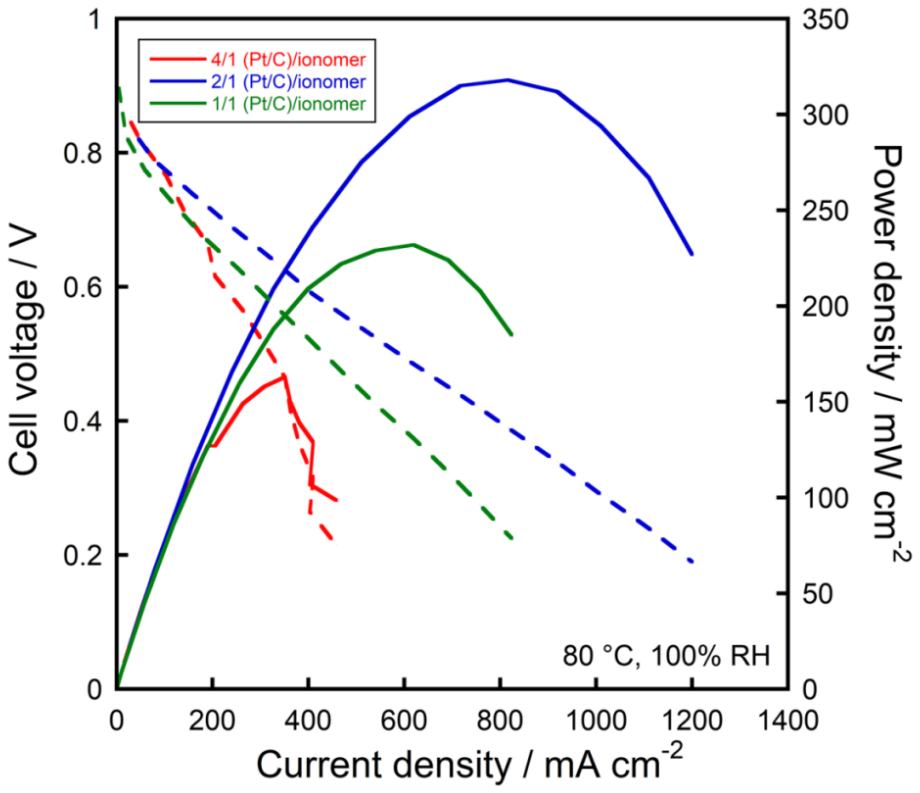

Figure 5.6 Fuel cell polarization curves (dashed lines) and power density curves (solid lines) of MEAs with electrodes fabricated with NEXAR-1.0 ionomer at 4/1 (red), 2/1 (blue), and 1/1 (green) w/w (Pt/C)/ionomer in the catalyst ink solution. Fuel cell operating conditions: 1/2 mol/mol H_2/O_2 at 80 °C, 100% RH, and ambient pressure.

These results are supported by the electron microscopy images (shown in Figure 5.7) of the electrodes fabricated with different ratios of catalyst and ionomer. At 4/1 w/w (Pt/C)/ionomer (20 wt% ionomer of the solids in the solution), shown in Figure 5.7a, the ionomer is not clearly visible throughout the entire catalyst layer. Therefore, the catalyst particles are not continuously bound throughout and form small, loose aggregates, which form multiple, small pores in the catalyst layer. At 2/1 w/w (Pt/C)/ionomer (33 wt% ionomer of the solids in the solution), shown in Figure 5.7b, the ionomer is more visibly present throughout, binding multiple catalyst particles together. At 1/1 w/w (Pt/C)/ionomer (50 wt% ionomer of the solids) in the solution, shown in

Figure 5.7c, the ionomer creates larger aggregates with strands of ionomer and embeds some of the individual catalyst particle aggregates. These results suggest that the amount of ionomer has a significant impact on the binding of ionomer to the catalyst particles, and subsequently the catalyst layer morphology. These visual observations coincide with the fuel cell performance in Figure 5.6, where at low ionomer content (4/1 (Pt/C)/ionomer), the lack of ionomer (*i.e.*, poor proton conduction) between catalyst particles results in poor and erratic fuel cell performance. However, at high ionomer content (1/1 (Pt/C)/ionomer), the ionomer surrounding the catalyst particles (*i.e.*, poor gas transport), results in a lower performance. Therefore, there is an optimum catalyst/ionomer ratio (2/1 (Pt/C)/ionomer) using NEXAR-1.0 as an ionomer in fuel cell electrodes.

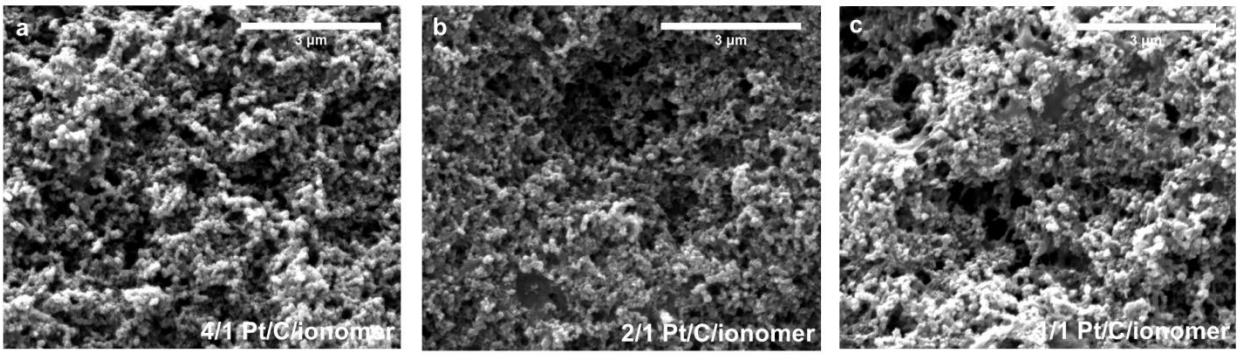

Figure 5.7 SEM images of electrodes fabricated with NEXAR-1.0 ionomer: (a) 4/1, (b) 2/1, and (c) 1/1 w/w (Pt/C)/ionomer in the catalyst ink solution. X 30000 magnification, scale bar = 3 µm.

Figure 5.8 shows fuel cell performances (hydrogen/oxygen fuel cell polarization and power curves at ambient pressure at 80 °C, 100% RH) for NEXAR-1.0/NEXAR-1.0 MEAs with different 1-propanol/water ratios in the NEXAR-1.0 ionomer catalyst ink solution. At a low water content (2/1 w/w 1-propanol/water), the maximum power density is 125 mW cm^{-2} and the

polarization curve exhibits erratic behavior at higher current densities. At a higher water content (1/1 w/w 1-propanol/water), the maximum power density is 204 mW cm^{-2}, which is a 63% gain in power output. A further increase in water content (1/2 w/w 1-propanol/water) increases the power density to 270 mW cm^{-2}, which is an additional 32% gain in power output. However, using pure water (0/1 w/w 1-propanol/water) decreases the power density to 178 mW cm^{-2}. These results suggest that the amount of water in the catalyst ink solution can significantly affect fuel cell performance due to changes in catalyst layer morphology.

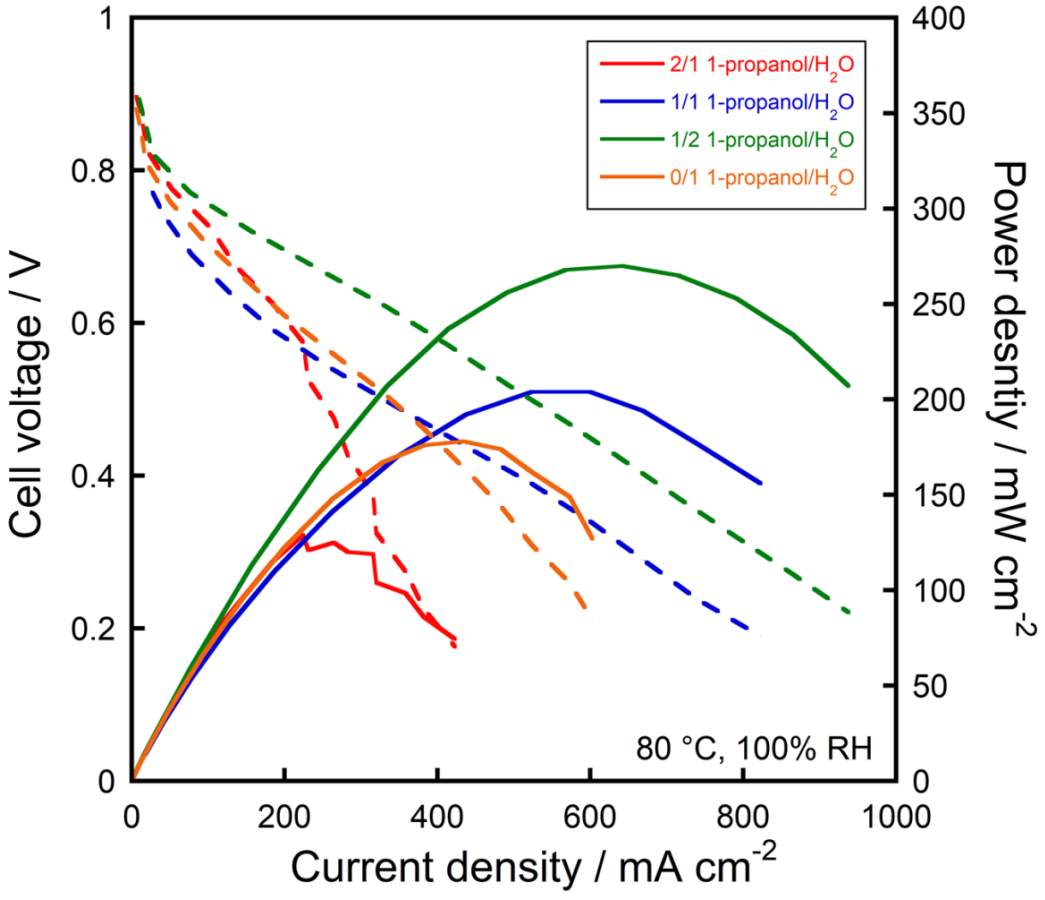

Figure 5.8 Fuel cell polarization curves (dashed lines) and power density curves (solid lines) of MEAs with electrodes fabricated with NEXAR-1.0 ionomer at 2/1 (red), 1/1 (blue), 1/2 (green), and 0/1 (orange) w/w 1-propanol/H_2O in the catalyst ink solution. Fuel cell operating conditions: 1/2 mol/mol H_2/O_2 at 80 °C, 100% RH, and ambient pressure.

These results are supported by the electron microscopy images, shown in Figure 5.9, of the electrodes fabricated using different water contents. At 2/1 w/w 1-propanol/water (33 wt% water content in the solution), as shown in Figure 5.9a, there are multiple large pores in addition to many small pores in the electrode. At 1/1 w/w 1-propanol/water (50 wt% water content in the solution), as shown in Figure 5.9b, there are still large pores, but fewer larger pores overall. At 1/2 w/w 1-propanol/water (67 wt% water content in the solution), as shown in Figure 5.9c, all pores are small with no visible evidence of the large pores observed in Figures 5.9a and 5.9b. At 0/1 w/w 1-propanol/water (*i.e.,* pure water in the solution), as shown in Figure 5.9d, the pores between catalyst particles appear even smaller and the presence of ionomer is difficult to distinguish. These results suggest that the amount of water has a significant impact on the morphology of the catalyst layer, specifically on the pore sizes between catalyst particle aggregates. The higher boiling point temperature of water may allow slower evaporation, which results in smaller pores, compared to the lower boiling point temperature of 1-propanol, which evaporates more rapidly, resulting in larger pores. The fuel cell results in Figure 5.8 corroborate with the electron microscopy images in Figure 5.9, where the highest fuel cell performance coincides with the optimal electrode morphology at an optimum solvent ratio (1/2 w/w 1-propanol/water) with NEXAR-1.0 as an ionomer. Table 5.3 summarizes these results, including the catalyst loadings and average maximum power densities.

Table 5.3 Catalyst loading, catalyst ink composition, and performance of NEXAR-1.0 MEAs.

MEA	Pt loading[a] (mg_{Pt} cm^{-2})	(Pt/C)/ionomer	1-propanol/H_2O	Max power density[b] (mW cm^{-2})
1	0.18/0.46	1/1	1/1	230 ± 4
2	0.22/0.43	2/1	1/1	320 ± 9
3	0.18/0.35	4/1	1/1	142 ± 27
4	0.19/0.21	2/1	2/1	143 ± 23
5	0.19/0.22	2/1	1/1	206 ± 17
6	0.21/0.15	2/1	1/2	271± 9
7	0.17/0.21	2/1	0/1	180 ± 11

[a]Anode/cathode catalyst loading, respectively.
[b]Measured at 1/2 mol/mol H_2/O_2 at 80 °C, 100% RH, and ambient pressure.

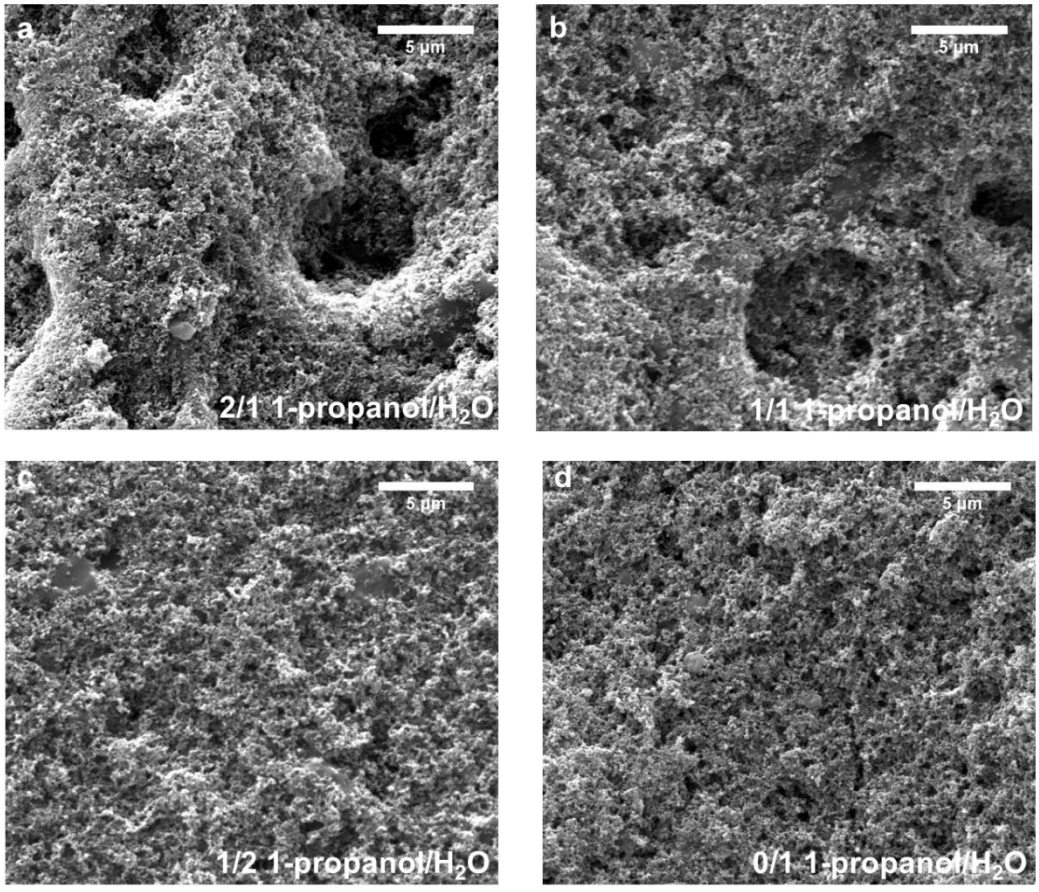

Figure 5.9 SEM images of electrodes fabricated with NEXAR-1.0 ionomer at (a) 2/1, (b) 1/1, (c) 1/2, and (d) 0/1 w/w 1-propanol/H_2O in the catalyst ink solution. X 10000 magnification, scale bar = 5 µm.

Figure 5.10 compares fuel cell performances (hydrogen/oxygen fuel cell polarization and power curves with back pressure of 1.7 bar at 80 °C, 100% RH) of optimized Nafion NR-212/Nafion (control), NEXAR-1.0/Nafion, and NEXAR-1.0/NEXAR-1.0 MEAs. The NEXAR-1.0 ionomer-based electrodes used the optimum catalyst/ionomer and 1-propanol/water compositions (2/1 w/w (Pt/)/ionomer and 1/2 w/w 1-propanol/water) as shown in earlier results. Nafion NR-212/Nafion has the highest maximum power density (1120 mW cm^{-2}) compared to NEXAR-1.0/Nafion (489 mW cm^{-2}) and NEXAR-1.0/NEXAR-1.0 (307 mW cm^{-2}). These results suggest that although NEXAR-1.0 has excellent proton conductivity, as well as thermal and mechanical stability under fuel cell operation, there is an additional resistance in the fuel cell that lowers performance compared to an all-Nafion MEA.

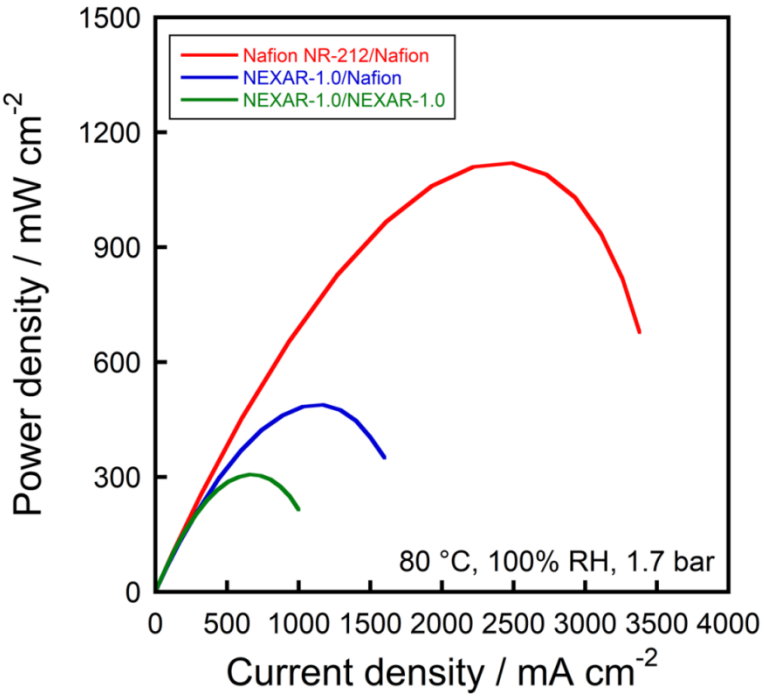

Figure 5.10 Fuel cell power density curves of MEAs fabricated under optimum conditions for each MEA (membrane/ionomer): Nafion NR-212/Nafion (red), NEXAR-1.0/Nafion (blue), NEXAR-1.0/NEXAR-1.0 (green). Fuel cell operating conditions: 1/2 mol/mol H_2/O_2 at 80 °C, 100% RH, and back pressure = 1.7 bar.

Figure 5.11 compares average maximum power densities and corresponding electrolyte membrane resistances under different fuel cell relative humidities. As shown in Figure 5.11a, the average maximum power density increases with increasing relative humidity, where at low relative humidity (30% RH), Nafion NR-212/Nafion (487 mW cm^{-2}) is higher than NEXAR-1.0/Nafion (101 mW cm^{-2}) and NEXAR-1.0/NEXAR-1.0 (62 mW cm^{-2}) and at high relative humidity (100% RH), Nafion NR-212/Nafion (1170 mW cm^{-2}) is also higher than NEXAR-1.0/Nafion (524 mW cm^{-2}) and NEXAR-1.0/NEXAR-1.0 (309 mW cm^{-2}). Interestingly, the power density of NEXAR-1.0/NEXAR-1.0 is higher at 90% RH (388 mW cm^{-2}) compared to 100% RH and comparable with that of NEXAR-1.0/Nafion (374 mW cm^{-2}). In addition, the power density of NEXAR-1.0/NEXAR-1.0 and NEXAR-1.0/Nafion are also comparable at lower relative humidity (246 and 278 mW cm^{-2}, respectively, at 60% RH). These results suggest that the optimized NEXAR-1.0 electrodes are comparable to Nafion (control) electrodes under fuel cell operation. As shown in Figure 5.11b, the electrolyte membrane resistance decreases with increasing relative humidity, where at low relative humidity (30% RH), Nafion/NR-212 (0.16 Ω cm^2) is four times lower than NEXAR-1.0/Nafion (0.61 Ω cm^2) and NEXAR-1.0/NEXAR-1.0 (0.71 Ω cm^2) and at high relative humidity (100% RH), Nafion/NR-212 (0.08 Ω cm^2) is two times lower than NEXAR-1.0/Nafion (0.13 Ω cm^2) and NEXAR-1.0/NEXAR-1.0 (0.12 Ω cm^2).

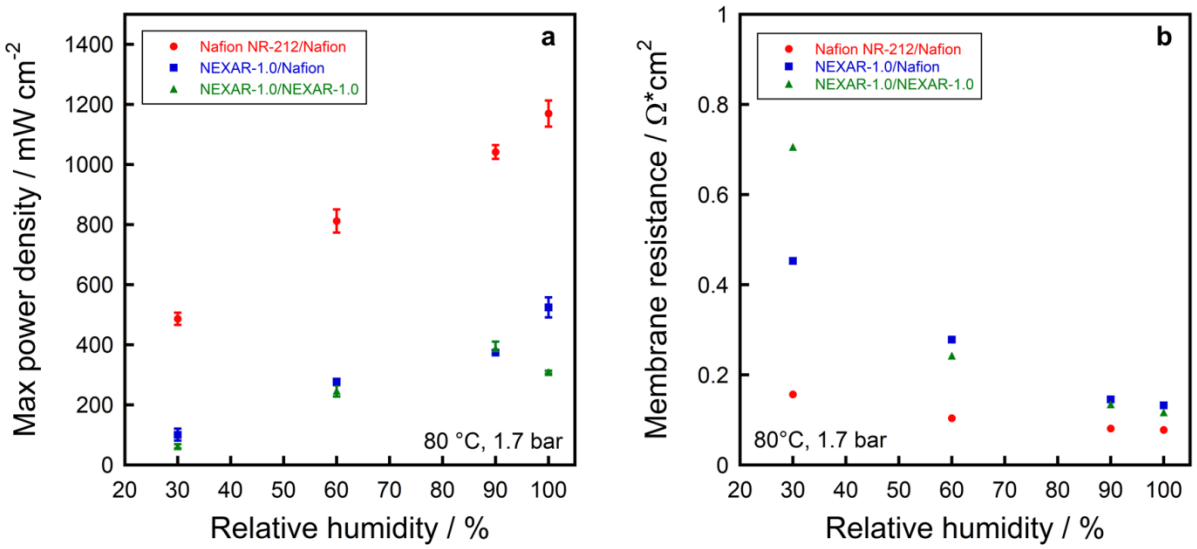

Figure 5.11 Fuel cell (a) maximum power densities and (b) membrane resistance of MEAs at different relative humidities fabricated under optimum conditions for each MEA (membrane/ionomer): Nafion NR-212/Nafion (red), NEXAR-1.0/Nafion (blue), NEXAR-1.0/NEXAR-1.0 (green). Fuel cell operating conditions: 1/2 mol/mol H_2/O_2 at 80 °C and back pressure = 1.7 bar.

The results in Figure 5.11b (membrane resistance) explains the differences observed if fuel cell performance, but contradicts the proton conductivity results in Figure 5.2. This suggests that under the conditions of the fuel cell, the NEXAR membrane properties may be changing. Figure 5.12a shows the temperature-dependent (ranging from 30–80 °C) proton conductivity at 90% RH for the Nafion NR-212 and NEXAR-1.0 (untreated and treated) membranes. The conductivities of all membranes increase with increasing temperature, where at a lower temperature (30 °C), NEXAR-1.0 (untreated) (0.09 S cm^{-1}) is almost one magnitude higher than Nafion NR-212 (0.02 S cm^{-1}) and NEXAR-1.0 (treated) (0.02 S cm^{-1}), and at a higher temperature (80 °C), Nafion NR-212 (0.14 S cm^{-1}) and NEXAR-1.0 (untreated) (0.22 S cm^{-1}) are almost one magnitude higher than NEXAR-1.0 (treated) (0.03 S cm^{-1}). Figure 5.12b shows the humidity-dependent (ranging from 30 – 90% RH) proton conductivity at 60 °C for the Nafion NR-212 and NEXAR-1.0

(untreated and treated) membranes. The conductivities of all membranes increase with increasing relative humidity, where at a low relative humidity (30% RH), Nafion NR-212 (6.2×10^{-3} S cm^{-1}) and NEXAR-1.0 (untreated) (3.9×10^{-3} S cm^{-1}) are one magnitude higher than and NEXAR-1.0 (treated) (0.2×10^{-3} S cm^{-1}). At a higher relative humidity (90% RH), Nafion NR-212 (9.8×10^{-3} S cm^{-1}) and NEXAR-1.0 (untreated) (13.8×10^{-3} S cm^{-1}) are three times higher than and NEXAR-1.0 (treated) (3.2×10^{-3} S cm^{-1}). Therefore, these results confirm that the fuel cell operating conditions alters the proton conductivity properties of NEXAR-1.0 and these results are in agreement with the power density and membrane resistance results in Figure 5.11. Therefore, these results suggest that the combination of pressure, gas flow, water, and temperature has an effect on the proton conductivity of the NEXAR-1.0 membrane that is not seen under *ex situ* environmental conditions (*i.e.,* only temperature and water). Overall, these results suggest that NEXAR-1.0 is a promising candidate as a membrane and ionomer in PEMFC applications due to its high conductivity (0.22 S cm^{-1} at 80 °C, 90% RH); however, alternative block compositions may improve the properties of the polymer (*e.g.,* less swelling) to minimize resistances within the fuel cell to match the performance of Nafion.

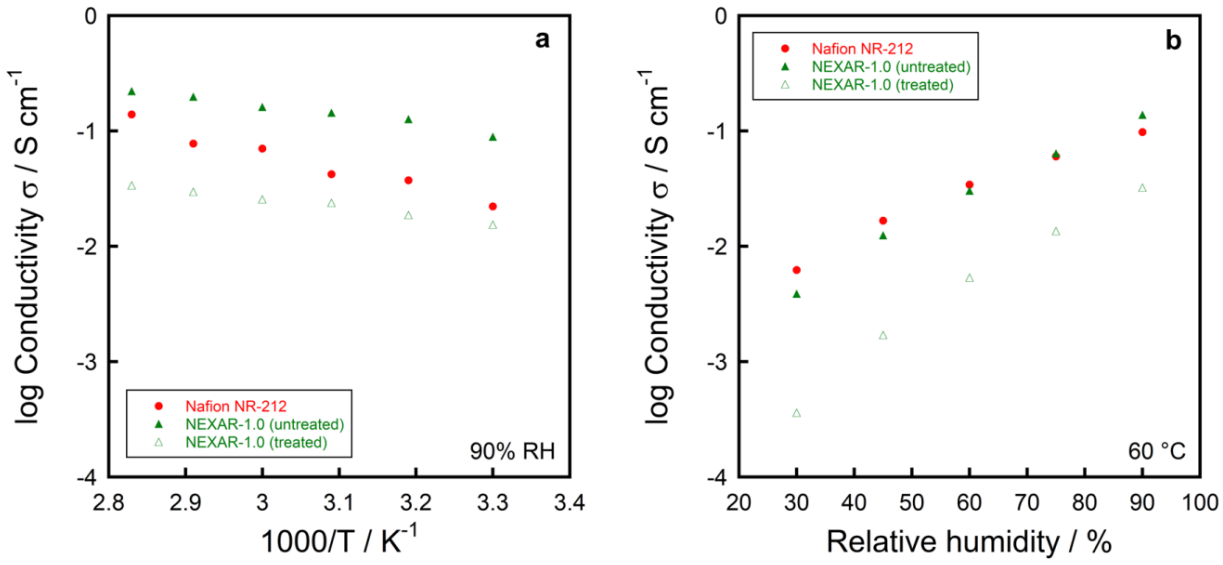

Figure 5.12 (a) Temperature-dependent proton conductivity at 90% RH and (b) humidity-dependent proton conductivity at 60 °C for Nafion NR-212 (closed red circles) and NEXAR with IEC of 1.0 meq g^{-1} membranes (untreated (closed green upward triangles) and treated (open green upward triangles)).

5.4 Conclusions

In this study, NEXAR with different IECs (1.0, 1.5, and 2.0) were investigated as membranes and ionomers in PEMFC applications. NEXAR, a commercially available hydrocarbon-based material, demonstrated higher proton conductivity for all IECs at all temperatures studied than the commercial perfluorinated membrane, Nafion. NEXAR with an IEC of 1.0 (NEXAR-1.0) proved to be the most durable after fuel cell operation and confirmed by *post mortem* still images of the NEXAR MEAs. Therefore, NEXAR/NEXAR (membrane/ionomer) MEAs were developed with NEXAR-1.0 as the membrane and ionomer. Various compositions of 1-propanol and water as the solvent and ionomer and catalyst in the solids in the catalyst ink solution were investigated. A maximum in power density and minimum in catalyst layer resistance was observed at a composition of 1/1 w/w 1-propanol/water and 2/1 catalyst/ionomer in the catalyst ink solution. Furthermore, the NEXAR/NEXAR MEA demonstrated similar performance to

NEXAR/Nafion MEA under 80 °C, 90% RH. However, the Nafion/Nafion MEA is still superior in fuel cell performance. The electrolyte membrane resistance for the Nafion membraned-based MEA is two-times higher the NEXAR membraned-based MEA, which was supported by the conductivity results of the fuel cell-treated NEXAR-1.0 membrane, where the NEXAR-1.0 membrane had significantly lower conductivity after the fuel cell treatment. Alternative polymer compositions using NEXAR as a starting point may provide a future non-fluorinated polymer to substitute Nafion.

CHAPTER VI

SOLID-STATE ALKALINE FUEL CELL PERFORMANCE OF PENTABLOCK TERPOLYMER WITH METHYLPYRROLIDINIUM CATIONS AS ANION EXCHANGE MEMBRANE AND IONOMER

6.1 Introduction

AFCs are attractive alternatives to proton exchange membrane fuel cells PEMFCs due to the faster oxygen reduction reaction kinetics in alkaline environments, which allows the use of non-noble catalysts (*e.g.,* nickel), *i.e.,* a low-cost alternative to the PEMFC. However, unlike PEMFCs which have commercially available, robust proton exchange membranes, AFCs have not yet identified a durable, commercially viable anion exchange membrane (AEM). AEMs require the following properties for long-lasting performance: electron insulating (*i.e.,* barrier to electrons), high ionic conductivity (*i.e.,* hydroxide ion transport), good mechanical strength (*i.e.,* limited swelling in water), and good chemical stability (*i.e.,* no degradation in alkaline environments).[66]

Recently, several investigators have developed and characterized new ion-containing polymer materials, such as graft polymers,[67-69, 76] random co-polymers,[71-75, 77-82] and block co-polymers,[70, 173-180] as AEMs to meet these requirements, focusing on alkaline stability and conductivity. Block co-polymers (BCPs) have a distinct advantage over random co-polymers due to the unique self-assembly of blocks into well-defined nanostructures. In the context of AEMs, BCPs can combine the properties of a non-ionic polymer (*e.g.,* poly(styrene)) and an ionic polymer (*e.g.,* poly(vinylbenzyltrimethylammonium hydroxide) into one material platform.[181] Ye *et al.*[182] demonstrated an order-of-magnitude higher hydroxide ion conductivity for a block copolymer

compared to its analogous random copolymer, suggesting that the microphase separation of the blocks (*i.e.,* confinement of ions and water in ion-rich phases) may contribute to enhanced properties (*i.e.,* improved ion transport). These observations are further supported by several studies that have reported high elastic modulus[177] and good ion conductivity of BCPs[178] which are ideal AEM properties. Recently, Ertem *et al.*[180] reported low water uptake and high bromide ion conductivity of a pentablock terpolymer with a quaternary ammonium cation (22 wt% at 60 °C, 95% RH and 57 mS cm^{-1} at 90 °C, 95% RH, respectively), suggesting this pentablock terpolymer is a promising candidate as an AEM for AFC applications. However, the stability of this polymer has yet to be determined. A recent review by Dekel[85] summarized the AFC stability studies on quaternary ammonium cation-based polymers for the last two decades with test durations as long as 5 h and decay rates (*i.e.*, difference in voltage loss over time) between 0.6 and 1 mV h^{-1}.

Quaternary ammonium is the most commonly studied cation for designing and developing polymers as AEMs. However, Meek and Elabd[84] demonstrated that polymers with alternative cations, such as imidazolium and pyrrolidinium, have better alkaline stability than the ubiquitous quaternary ammonium cation, suggesting that other cation-based polymers could perform better as AEMs. This is further supported by Ponce-Gonzalez *et al.*[183] which demonstrated that radiation-grafted ETFE films with methylpyrrolidinium cations had better stability and performance than the quaternary ammonium cation.

Recently, Meek *et al.*[179] investigated a pentablock terpolymer with methylpyrrolidinium cations and demonstrated high hydroxide ion conductivity (44 mS cm^{-1} at 60 °C in liquid water) and excellent stability (0% conductivity loss after 168 h in 1 M KOH at 60 °C). However, the performance and durability of this pentablock terpolymer with methylpyrrolidinium cations as a

membrane and ionomer in AFC applications have yet to be determined. In light of these recent publications, there is significant motivation in investigating the stability and performance of alternative cation-based polymers (*e.g.,* methylpyrrolidinium and methylpiperidinium cations). Here, in this work, a pentablock terpolymer (PTP) with methylpyrrolidinium cation and hydroxide anion was used as the membrane and ionomer in alkaline fuel cells with a focus on the effect of the PTP with methylpyrrolidinium cations as an ionomer and the fuel cell operating conditions on AFC performance. The effect of the solvent and solids compositions on the catalyst layer morphology and fuel cell performance were investigated and compared. The effect of the fuel cell temperature and relative humidity on fuel cell performance and resistances was also studied.

6.2 Experimental Methods

6.2.1 Materials

Initially, a precursor polymer was used to synthesize and fabricate hydroxide ion conducting pentablock terpolymer films. The precursor polymer is an ABCBA pentablock terpolymer (PTP), poly(tbS-*b*-EP-*b*-MS-*b*-EP-*b*-tbS), that was synthesized and provided by Kraton Performance Polymers and contains tert-butyl-styrene (tbS) as the A outer blocks, a random copolymer of ethylene-*r*-propylene (EP) as the B blocks, and 4-methyl styrene (MS) as the inner C block. This precursor ABCBA pentablock terpolymer has a $M_n \approx 76$ kg mol^{-1} with M_n of respective blocks equal to 15-13-16-14-18 kg mol^{-1}. The precursor polymer was subsequently brominated and quaternized to covalently attach the methylpyrrolidinium cation to the inner C block. Extensive details of the bromination and quaternization of this polymer have been reported elsewhere.[184] Methanol (MeOH; ACS reagent, ≥ 99.8%), tetrahydrofuran (THF; anhydrous, ≥ 99.9%), toluene

(anhydrous, ≥ 99.8%) and potassium hydroxide (KOH; reagent, 90%) were purchased from Sigma-Aldrich. 20 wt% platinum on carbon (Pt/C; Vulcan XC-72) was purchased from Premetek Co. Gas diffusion layer (GDL; Sigracet 25BC), Fumapem membrane (FAA-3-50; Fumatech), and Fumion solution (10 wt% in N-2-methylpyrrolidone; FAA-3-SOLUT-10; Fumatech) were purchased from Fuel Cells Etc. All materials were used as received. Deionized (DI) water with a resistivity of 16 MΩ cm was used as appropriate. Ultra-high purity grade nitrogen, ultra-high purity grade hydrogen, and ultra-high purity grade oxygen were purchased from Airgas. All gases were used for all fuel cell experiments.

6.2.2 Polymer Film Preparation

Bromide ion-form of the PTP films were fabricated by casting the quaternized polymer solution (16 wt% in 4/1 w/w toluene/methanol) onto a silicon-coated Mylar PET film using an automatic film applicator (Elcometer 4340) with a doctor blade at gauge height and speed of *ca.* 800 μm and 90 mm s^{-1}, respectively, under ambient conditions. Films were partially covered by aluminum foil and evaporation of solvent occurred under ambient condition for at least 12 h. The films were then annealed under 100 °C for 48 h before use. The final film thicknesses were *ca.* 70-80 μm and measured with a digital micrometer (Marathon; accuracy = 2 μm). For MEA fabrication, the films were cut into square pieces of *ca.* 30 mm (L) × 30 mm (W).

6.2.3 Electrode Fabrication and Ion Exchange

The catalyst ink solution used to fabricate Fumion electrodes (control) consisted of a 1 wt% mixture of 110 mg of Pt/C catalyst, 360 mg of Fumion solution, and 14.2 g of 1/1 w/w THF/MeOH co-solvent mixture. The resulting mixture was sonicated for 3 min at 35% amplitude

(Q125, QSonica) and subsequently brushed onto a GDL substrate (*ca.* 30 mm (L) x 30 mm (W)) with an ox hair brush (0689-00025, Gordon Brush Mfg. Co., Inc.). This process was repeated to achieve the target Pt loading of *ca.* 0.30 mg_{Pt} cm^{-2}. The catalyst ink solution used to fabricate PTP electrodes consisted of a mixture of Pt/C catalyst, PTP as the ionomer, water, and methanol. The amount of water, methanol, catalyst, and ionomer were adjusted to achieve different ratios of methanol and water, and catalyst and ionomer in the catalyst ink solution as detailed in Table 6.1 (see section 6.3). The solids content was held constant at 1 wt% for all electrode fabrication. The resulting mixture was sonicated for 3 min at 35% amplitude (Q125, Qsonica) prior to airbrushing with an airbrush gun (AEROPRO1, Aeroblend) on a GDL substrate (*ca.* 25 mm (L) x 25 mm (W)) on a hot plate heated to 120 °C. The process was repeated to achieve the target Pt loading of *ca.* 0.10 mg_{Pt} cm^{-2}. The films and electrodes were ion exchanged in a 1.0 M KOH solution for 24 h under ambient conditions (chemical structure of PTP in hydroxide form shown in Figure 6.1). The films and electrodes were extensively washed with DI water (once per hour, three times) prior to assembling in the fuel cell stack.

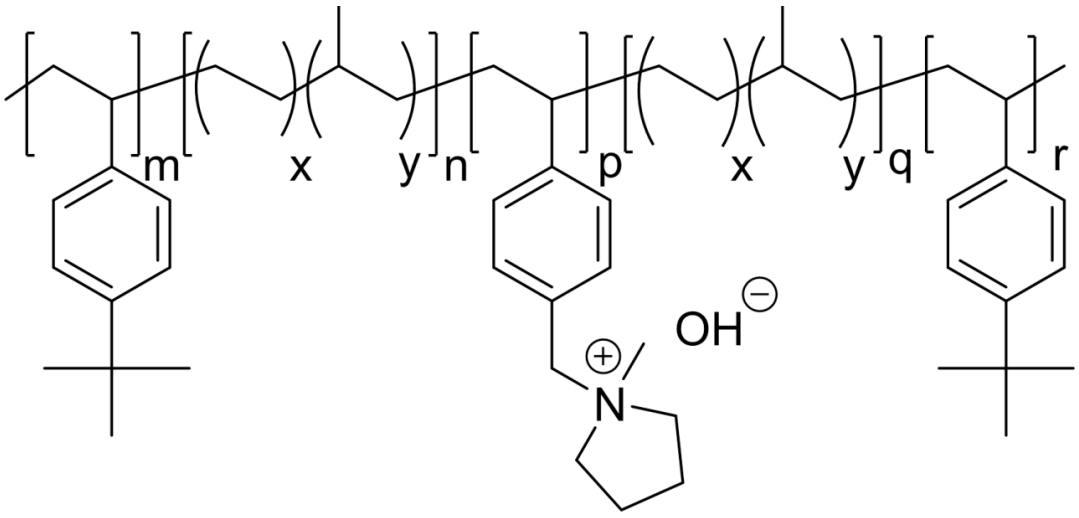

Figure 6.1 Chemical structure of PTP with methylpyrrolidinium cation and hydroxide anion.

6.2.4 Electrode Characterization

The morphology of the electrodes was investigated with scanning electron microscopy (SEM; FEI Quanta 600 FE-SEM, 10 kV) using a working distance of 10 mm. Samples were sputter coated (Cressington 208 HR) with iridium (6 nm thickness) prior to SEM analysis.

The Pt loading was measured with thermal gravimetric analysis (TGA; Q50, TA Instrument). A small portion of the electrode (*ca.* 2–6 mg) was heated in the TGA from ambient temperature to 900 °C at 10 °C min^{-1} in air at 60 mL min^{-1}. Since all components in the electrode degrade below 800 °C with the exception of Pt, the Pt loading was determined by dividing the residual weight at 850 °C by the original area of the TGA sample.

6.2.5 Membrane Electrode Assembly (MEA) and Fuel Cell Tests

Membrane electrode assemblies (MEAs) were fabricated by placing either the Fumion membrane or PTP film between two catalyst-coated GDLs (anode and cathode) in the fuel cell without any heat pressing, which was placed between two serpentine flow field graphite plates (5 cm^2 flow area) separated by two 0.152 mm thick PTFE/fiberglass gaskets (Gasket Set #5, Scribner Associates, Inc.). The entire fuel cell assembly consisted of an MEA, two gaskets, and two flow plates placed between copper current collectors followed by endplates all held together by bolts with 2.8 N m of applied torque. Fuel cell performance of each MEA was evaluated with a fuel cell test station (850e, Scribner Associates, Inc.). Fuel cell tests were conducted under ambient pressure with saturated (100% RH) anode and cathode flow rates of 0.2 L min^{-1} hydrogen and 0.2 L min^{-1} oxygen, respectively, corresponding to a stoichiometric ratio of 1:1 hydrogen:oxygen. The cathode gas, anode gas, and cell temperatures were all maintained at 30 °C. Fuel cell performance was recorded after a new MEA was fully activated. The activation

process consisted of operating the MEA at 0.5 V for 1 h, followed by three cycles of 0.6 V and 0.4 V for 30 min at each voltage. The MEA was at steady state when no further increase in current density at a constant voltage was observed. After the MEA was fully activated and reached steady state, polarization curves (cell voltage versus current density) were collected from open circuit voltage (OCV) to 0.2 V at at increments of 0.05 V every 5 min. Five polarization curves were collected to determine the average maximum power density.

6.2.6 Electrochemical Impedance Spectroscopy (EIS)

Electrochemical impedance spectroscopy (EIS; Solartron SI 1260A) was performed on a fully activated MEA from 1 MHz to 1 Hz at *ca.* 0.86 V *versus* NHE under ambient pressure. In this two-electrode configuration, the anode serves as both the counter and reference electrodes. The fuel cell anode and cathode were supplied with 0.2 L min^{-1} hydrogen and 0.2 L min^{-1} oxygen, respectively. Temperatures of the cathode gas, anode gas, and cell were all maintained at 30 °C. The EIS data was analyzed using a common equivalent circuit model that consisted of a resistor (resistance of the solid electrolyte membrane) in series with a parallel circuit, typically used to describe a porous electrode,[111] of a constant phase element and a second resistor (resistance of the catalyst layer in the electrode). Two parallel circuits were employed to describe the two electrodes (anode and cathode) in the MEA. The catalyst layer resistances reported here are the polarization resistances.

6.2.7 Durability Tests

The fuel cell anode and cathode were supplied with 0.2 L min^{-1} hydrogen and 0.2 L min^{-1} oxygen, respectively. Temperatures of the cathode gas, anode gas, and cell were all maintained at

either 30 or 40 °C. MEAs were held at a constant current density (typically the current density at a voltage slightly lower than the voltage where maximum power density occurs) for at least 72 h. The voltage was recorded and normalized with the initial voltage at t = 0 h (V_o) for the duration of the durability test. The decay rate was calculated from the slope of the linear regression to the data.

6.3 Results and Discussion

First, the fuel cell performance of an MEA with PTP AEM was compared to an MEA with commercial Fumatech (Fumapem) AEM (control). Both MEAs contained commercial Fumion solution as the ionomer in the electrodes (0.4 mg_{Pt} cm^{-2} loading). Figure 6.2 shows fuel cell performances (polarization and power curves; hydrogen/oxygen at ambient pressure at 30 °C, 100% RH) for both the PTP and Fumatech MEAs at t = 0 h and t = 72 h. At t = 0 h, the maximum power density for the PTP MEA (26.5 mW cm^{-2}) was 8% higher than the Fumatech MEA (23.4 mW cm^{-2}). However, after 72 h, under constant current density, the maximum power density of the PTP MEA (15.9 mW cm^{-2}) was 179% higher than the Fumatech MEA (5.7 mW cm^{-2}).

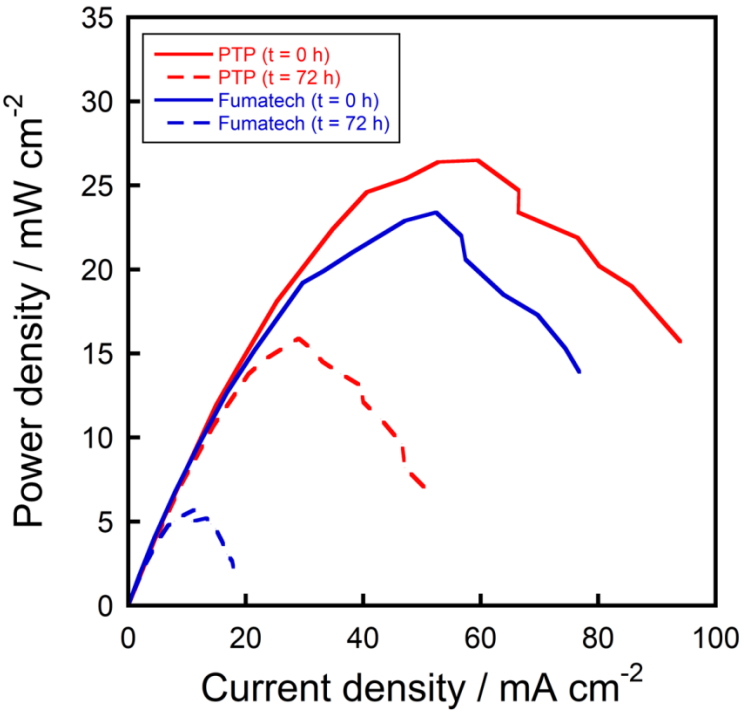

Figure 6.2 Fuel cell polarization curves of PTP MEA (red) and Fumatech MEA (blue) both with 3/1 Pt/C/Fumion electrodes with 0.4 mg_{Pt} cm^{-2} Pt loading at t = 0 h (solid) and t = 72 h (dashed). Fuel cell operating conditions: 1/1 mol/mol H_2/O_2 at 30°C, 100% RH, and ambient pressure.

Both MEAs were held at a constant current density (40.7 mA cm^{-2} and 27.3 mA cm^{-2} for PTP and Fumatech, respectively) over the 72 h. The PTP MEA was able to maintain a constant current density (40.7 mA cm^{-2}) for 72 h as shown in Figure 6.3a. However, the Fumatech MEA was only able to maintain a constant current density (27.3 mA cm^{-2}) for 41 h and then continually dropped until it decreased to 41% of the initial current density (16.2 mA cm^{-2}) at t = 72 h, as shown in Figure 6.3a. The short-term (t = 0–5 h) voltage decay rate for the PTP MEA (5.6 mV h^{-1}) was 32% less than for the Fumatech MEA (8.2 mV h^{-1}). The long-term (t = 15–72 h for PTP MEA, t = 15–40 h for Fumatech membrane MEA) voltage decay rate for the PTP MEA (1.7 mV h^{-1}) was 76% less compared to the Fumatech MEA (7.0 mV h^{-1}). These results show improved life-time stability for the PTP AEM compared to the Fumatech AEM. There are a

number of factors that can be attributed to these differences. One factor may include the higher alkaline stability of the methylpyrrolidinium cation in the PTP AEM compared to the quaternary ammonium cation in the Fumatech AEM, supported by other studies that show excellent alkaline stability for the pyrrolidinium cation compared to the quaternary ammonium cation.[178, 185]

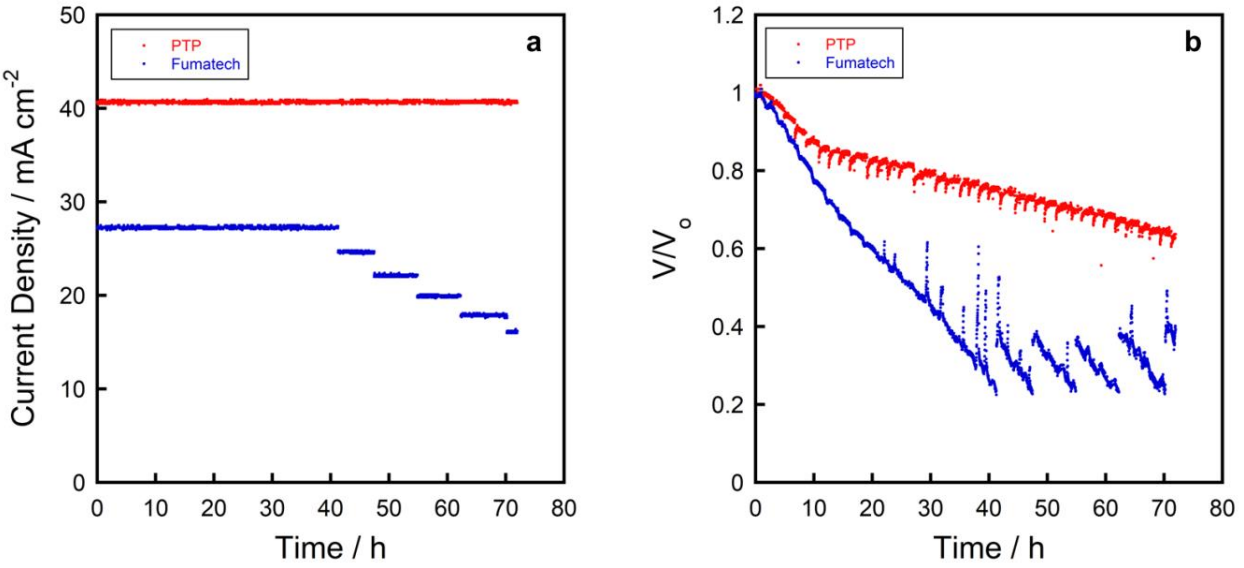

Figure 6.3 Fuel cell (a) current density and (b) normalized voltage *versus* time of the pentablock terpolymer (PTP) membrane MEA (red) and Fumatech membrane MEA (blue). Voltage is normalized by the initial voltage at t = 0 h (V_o). Fuel cell operating conditions: 1/1 mol/mol H_2/O_2 at 30°C, 100% RH, and ambient pressure.

PTP MEAs were also produced with PTP as both the membrane and the ionomer. Figures 6.4–6.7 represent the impact of changing the electrode solvent composition and catalyst/ionomer composition on the AFC performance of all these PTP MEAs. Table 6.1 lists the various electrode solvent compositions and catalyst/ionomer compositions investigated. Figure 6.4 shows fuel cell performances (polarization and power curves; hydrogen/oxygen at ambient pressure at 30 °C, 100% RH) for all PTP MEAs, where the electrodes were fabricated with

different methanol/water solvent compositions ratios in the catalyst ink solution. The PTP MEA fabricated with 11/1 w/w methanol/water solvent composition (*i.e.*, 8 wt% water in solution) resulted in a maximum power density of 34.9 mW cm^{-2}. Changing the solvent composition to 5/1 w/w methanol/water (*i.e.*, 17 wt% water in solution) resulted in a PTP MEA with a maximum power density of 40.3 mW cm^{-2} (15% increase). An additional change in solvent composition to 2/1 w/w methanol/water (*i.e.*, 33 wt% water in solution) resulted in a PTP MEA that produced a maximum power density of 57.2 mW cm^{-2} (an additional 17% increase). A further change in solvent composition to 1/2 w/w methanol/water (*i.e.*, 66 wt% water in solution) resulted in a PTP MEA that produced a maximum power density of 35.7 mW cm^{-2}, a similar output compared to the 11/1 w/w methanol/water composition. These results show that the highest maximum power density for an all PTP MEA occurs when the solvent composition is at 2/1 w/w methanol/water.

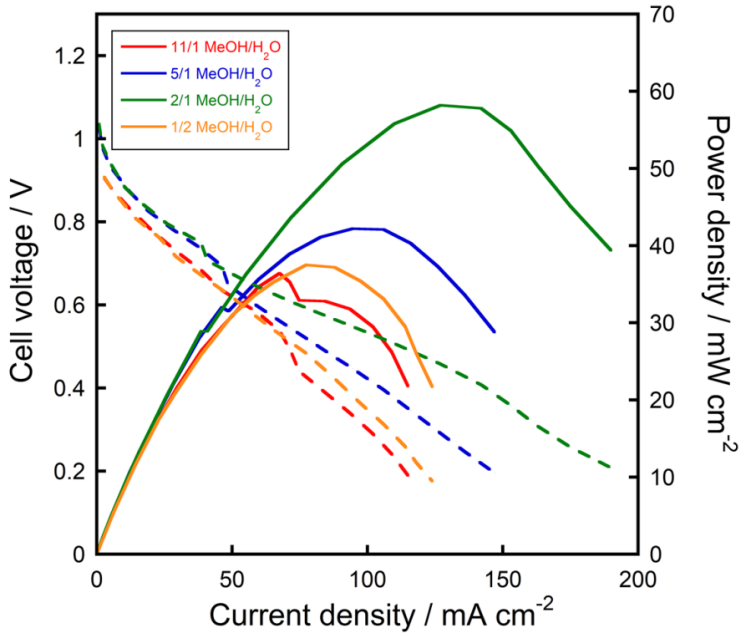

Figure 6.4 Fuel cell polarization curves (dashed) and power density curves (solid) of MEAs with 0.1 mg_{Pt} cm^{-2} electrodes fabricated with 11/1 $MeOH/H_2O$ (red), 5/1 $MeOH/H_2O$ (blue), 2/1 $MeOH/H_2O$ (green), and 1/2 $MeOH/H_2O$ (orange) in the catalyst ink solution. Fuel cell operating conditions: 1/1 mol/mol H_2/O_2 at 30 °C, 100% RH, and ambient pressure.

To understand the possible impact of electrode morphology on the results in Figure 6.4, scanning electron microscopy (SEM) images of the catalyst layers at the various solvent compositions are shown in Figure 6.5. At all solvent compositions, a connected network of pores, catalyst, and ionomer are evident. As the solvent composition increases in water content (from 11/1 w/w to 1/2 w/w methanol/water, shown from Figures 6.5a to 6.5d), it is clear that the ionomer becomes more evident in the images. Specifically, in Figure 6.5a and Figure 6.5b (11/1 and 5/1 w/w methanol/water), ionomer is noticeable, but not a majority component. In Figure 6.5c (2/1 w/w methanol/water), the ionomer is more evident and creates a distinct network among the catalyst network. A further increase in water content in the solvent (1/2 w/w methanol/water, shown in Figure 6.5d), results in large agglomerates of ionomer completely encapsulating regions of the catalyst network. The combination of Figure 6.4 and Figure 6.5c suggests that an optimal catalyst morphology is attained among the solvent compositions explored, *i.e.*, a connected a network of pores, catalyst, and ionomer with optimal number of triple phase boundaries. The combination of Figure 6.4 and Figure 6.5a and also Figure 6.4 and Figure 6.5b, suggests that the ionomer network may not be fully connected resulting in some hydroxide ion transfer resistance. The combination of Figure 6.4 and Figure 6.5d suggests that the excess of ionomer results in oxygen mass transfer resistance. Overall, these results show that 2/1 w/w methanol/water is the optimal solvent composition (among the compositions studied) for the catalyst ink solution to maximize the AFC performance of the PTP MEA.

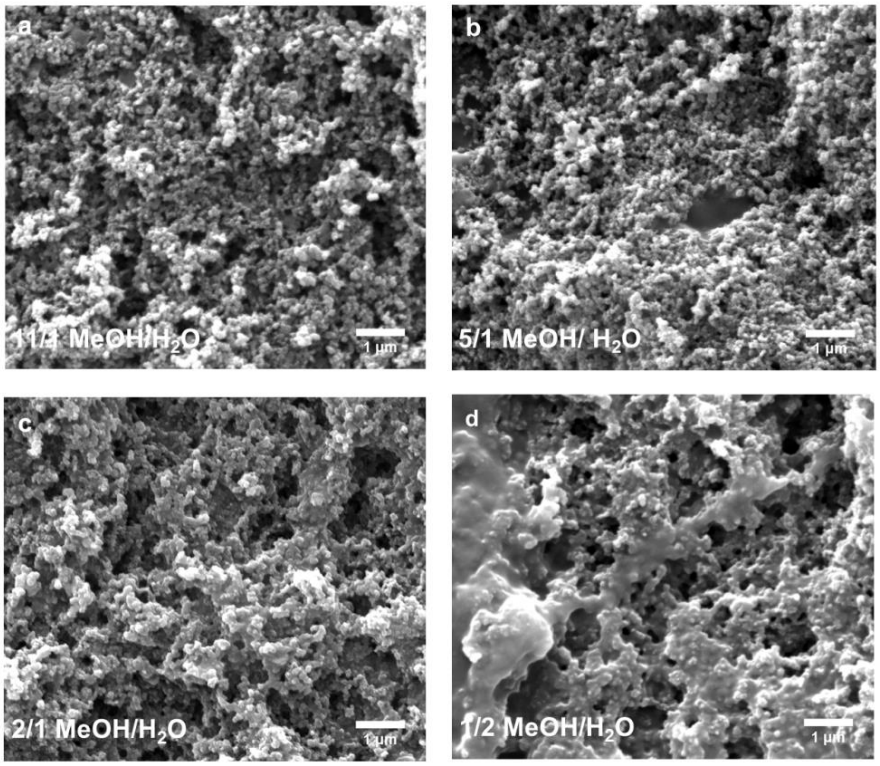

Figure 6.5 SEM images of electrodes with 0.1 $mg_{Pt}\,cm^{-2}$ at X 30000 magnification, scale bar = 1 µm: (a) 11/1 MeOH/H_2O, (b) 5/1 MeOH/H_2O, (c) 2/1 MeOH/H_2O, and (d) 1/2 MeOH/H_2O co-solvent mixtures in the catalyst ink solution.

Figure 6.6 shows fuel cell performances (polarization and power curves; hydrogen/oxygen at ambient pressure at 30 °C, 100% RH) for all PTP MEAs fabricated with different catalyst/ionomer ratios in the catalyst ink solution (all of these MEAs were fabricated at the optimal 2/1 w/w methanol/water solvent composition). As the catalyst/ionomer ratio changes from 4/1 to 2/1 to 1/1 w/w (Pt/C)/ionomer in the catalyst ink solution (*i.e.*, 20 wt% to 33 wt% to 50 wt% ionomer content in the solids in the catalyst ink solution) the resulting maximum power density of the PTP MEAs increases from 21.0 mW cm^{-2} to 57.2 mW cm^{-2} and then decreases to 18.9 mW cm^{-2}.

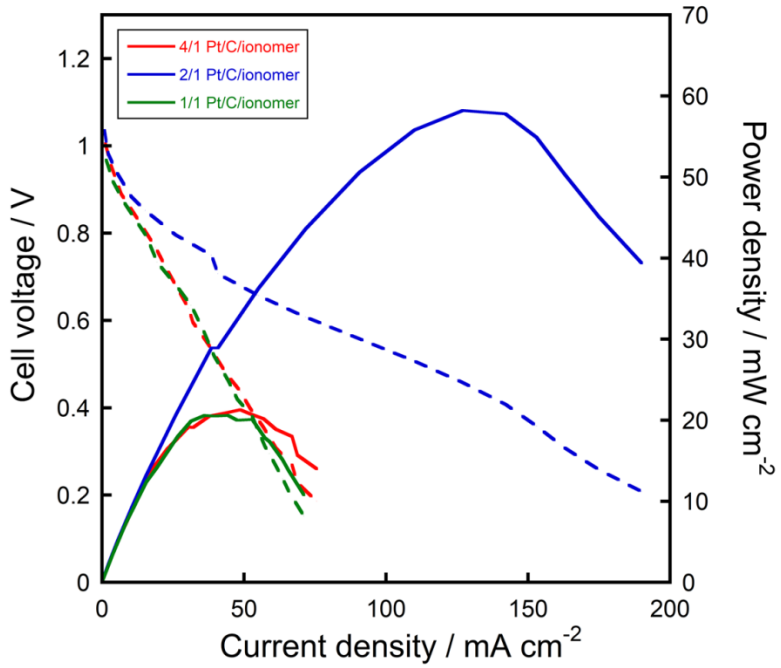

Figure 6.6 Fuel cell polarization curves (dashed) and power density curves (solid) of MEAs with 0.1 mg_{Pt} cm^{-2} electrodes fabricated with 4/1 catalyst/ionomer (red), 2/1 catalyst/ionomer (blue), and 1/1 catalyst/ionomer (green) in the catalyst ink solution. Fuel cell operating conditions: 1/1 mol/mol H_2/O_2 at 30 °C, 100% RH, and ambient pressure.

These results suggest that the catalyst layer morphology and the amount of ionomer in the electrode have a significant impact on the AFC performance. This is supported by SEM images of catalyst layers (Figure 6.7), where each image corresponds to different ratios of catalyst and ionomer in the catalyst ink solution. As shown in Figure 6.7a, with 4/1 w/w (Pt/C)/ionomer ratio in the catalyst ink solution, there is no or little ionomer attached to the catalyst particles, forming large catalyst particle aggregates. Figure 6.7b shows that as the catalyst/ionomer ratio in the catalyst ink solution changes to a 2/1 w/w (Pt/C)/ionomer ratio, the ionomer can be seen more clearly and acts as a binder between catalyst particle aggregates, forming smaller catalyst particle aggregates and more visible pores in the catalyst layer. As the catalyst/ionomer ratio changes further to 1/1 w/w (Pt/C)/ionomer, as shown in Figure 6.7c, the visible presence of the ionomer

is more notable as the ionomer covers large areas of the catalyst particles and binds them into large aggregates, which acts as a physical barrier to pores and prevents gas from reaching catalyst particles. These results suggest that the amount of ionomer in the catalyst ink solution also significantly affects the final catalyst layer morphology of the electrodes by increasing the presence of the ionomer that surrounds the catalyst particles. Overall, these results show that there is an optimum catalyst/ionomer ratio in the catalyst ink solution to maximize PTP AFC performance. Table 6.1 summarizes these results: methanol/water ratio, catalyst/ionomer ratio, Pt loading, and maximum power density.

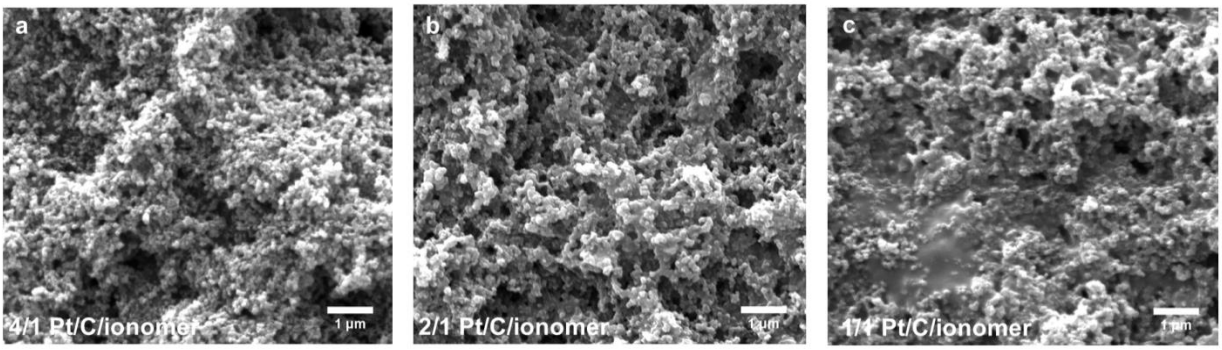

Figure 6.7 SEM images of electrodes with 0.1 $mg_{Pt}\,cm^{-2}$ at X 30000 magnification, scale bar = 1 µm: (a) 4/1 catalyst/ionomer, (b) 2/1 catalyst/ionomer, and (c) 1/1 catalyst/ionomer in the catalyst ink solution.

Table 6.1 Maximum power density as a function of electrode composition.

MEA	MeOH/H_2O	Catalyst/ionomer	Pt loading ($mg_{Pt}\,cm^{-2}$)	Max power density[a] ($mW\,cm^{-2}$)
1	11/1	2/1	0.09/0.08	34.9 ± 2.5
2	5/1	2/1	0.07/0.08	40.3 ± 1.7
3	2/1	4/1	0.09/0.11	21.0 ± 1.1
4	2/1	2/1	0.07/0.09	57.2 ± 1.4
5	2/1	1/1	0.10/0.07	18.9 ± 1.7
6	1/2	2/1	0.06/0.08	35.7 ± 1.4

[a]Measured at 1/1 mol/mol H_2/O_2 at 30 °C, 100% RH, and ambient pressure.

To further explore the impact of these different catalyst layer morphologies on fuel cell performance, EIS was conducted *in operando* to analyze polarization resistances of the PTP MEAs under 0.86 V *vs.* NHE. Reshetenko *et al.*[186] demonstrated that EIS of anion exchange membrane fuel cell (AEMFC) operation under low current density (*i.e.*, potential slightly lower than open circuit voltage) reveals two depressed capacitive semi-circles. One at high-frequency (>100 Hz) and one at intermediate-frequency (>1 Hz), suggesting that the high-frequency semi-circle is related to the anode processes and the intermediate-frequency semi-circle is related to cathode processes. Figure 6.8 shows the anode and cathode polarization resistances of the PTP MEAs as a function of the amount of water and amount of ionomer in the solids in the catalyst ink solution. Overall, the anode resistances are significantly smaller than the cathode process resistances, suggesting that the cathode (*i.e.*, oxygen reduction reaction) is the main resistance in the PTP MEA fuel cell.

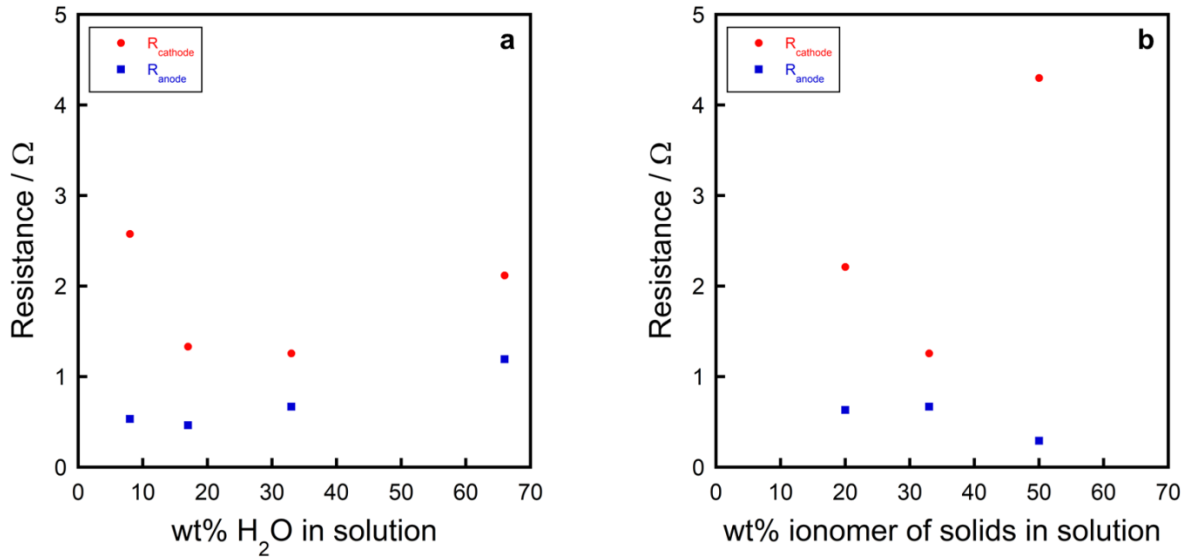

Figure 6.8 Cathode resistance (red) and anode resistance (blue) *versus* (a) water content in catalyst ink solution and (b) ionomer content in the electrode.

Figure 6.8a shows that the cathode resistance is high for electrodes fabricated using 8 wt% water content (11/1 w/w methanol/water) in the catalyst ink solution (2578 mΩ). The cathode resistance decreases with increasing water content reaching a minimum resistance at 33 wt% water content (2/1 w/w methanol/water) in the solution (1257 mΩ). Further increase in water content results in an increase in cathode resistance at 66 wt% water content (1/2 w/w methanol/water) (2119 mΩ). Interestingly, the anode resistance has a minimum at 17 wt% water content (5/1 w/w methanol/water) (464 mΩ). These results are further supported by the power density results, which shows that the highest maximum power density occurs at 33 wt% water content (2/1 w/w methanol/water ratio) in the solution, where the minimum total resistance occurs. As mentioned previously, changing the methanol/water ratio in the catalyst ink solution affects the final catalyst layer morphology in the electrodes, which has a significant impact on the fuel cell performance. The ideal catalyst layer morphology has sufficient connections for hydroxide ions and electrons as well as pores for gas transport for ease of access to triple phase boundaries. The importance of these features is emphasized in the differences in the resistances of the electrochemical reaction processes at the anode and cathode.

Figure 6.8b shows that the cathode resistances also decrease and increase with increasing ionomer content. At 20 wt% ionomer content (4/1 w/w (Pt/C)/ionomer ratio) of the solids in the catalyst ink solution, the cathode resistance is 2213 mΩ. The cathode resistance decreases with increasing ionomer content in the solution at 33 wt% ionomer content (2/1 w/w (Pt/C)/ionomer ratio) (1257 mΩ). Further increase in ionomer content results in an increase in cathode resistance at 50 wt% ionomer content (1/1 w/w (Pt/C)/ionomer ratio) (4300 mΩ). These results are further supported by the power density results, which shows that the highest maximum power density occurs at 33 wt% ionomer content (2/1 (Pt/C)/ionomer ratio) in the solution. Interestingly, the

anode resistances have an inverse trend compared to the cathode resistances, showing a minimum resistance at 50 wt% ionomer content (1/1 w/w (Pt/C)/ionomer ratio) (237 mΩ). The solid electrolyte membrane resistances were also evaluated from the EIS spectra. Most MEAs show a membrane resistance between 50 and 88 mΩ and open circuit voltage ≥ 1 V, suggesting that the membranes are in good condition (*i.e.,* no gas crossover). One MEA exhibits a membrane resistance of 120 mΩ and an open circuit voltage < 1 V, which suggests that the membrane may be compromised (*i.e.,* gas crossover). However, there was no significant loss in open circuit voltage in the beginning of the experiment (< 0.5 % loss within the first 30 minutes); therefore, the gas crossover is minimal. Overall, the EIS results support the fuel cell performance data. Table 6.2 summarizes these results: membrane, anode, and cathode resistances.

Table 6.2 *in operando* resistances at *ca.* 0.86 V *versus* NHE.

MEA	Open circuit voltage[a] (V)	Membrane resistance[b] (mΩ)	Anode resistance[b] (mΩ)	Cathode resistance[b] (mΩ)
1	0.94	120	534	2578
2	1.05	88	464	1333
3	1.02	53	631	2213
4	1.06	88	668	1257
5	1.00	88	293	4300
6	1.06	67	1193	2119

[a]Measured after activation procedure.
[b]Measured at 1/1 mol/mol H_2/O_2 at 30 °C, 100% RH, and ambient pressure.

To investigate the effect of fuel cell operating parameters (*e.g.,* temperature and humidity) on fuel cell performance, the fuel cell temperature was systematically increased from 30–50 °C, while maintaining 100% relative humidity. Figure 6.9a shows fuel cell performances (polarization and power curves; hydrogen/oxygen at ambient pressure at 100% RH) of an

optimized (*i.e.*, fabricated using optimal solution contents) PTP MEA at 30, 40, and 50 °C. The maximum power density at 30 °C is 40.5 mW cm^{-2}. As the temperature increased to 40 °C, the maximum power density increased to 74.0 mW cm^{-2}. A further increase in temperature to 50 °C, resulted in a decrease in the maximum power density to 53.8 mW cm^{-2} and shows erratic behavior in the polarization curve.

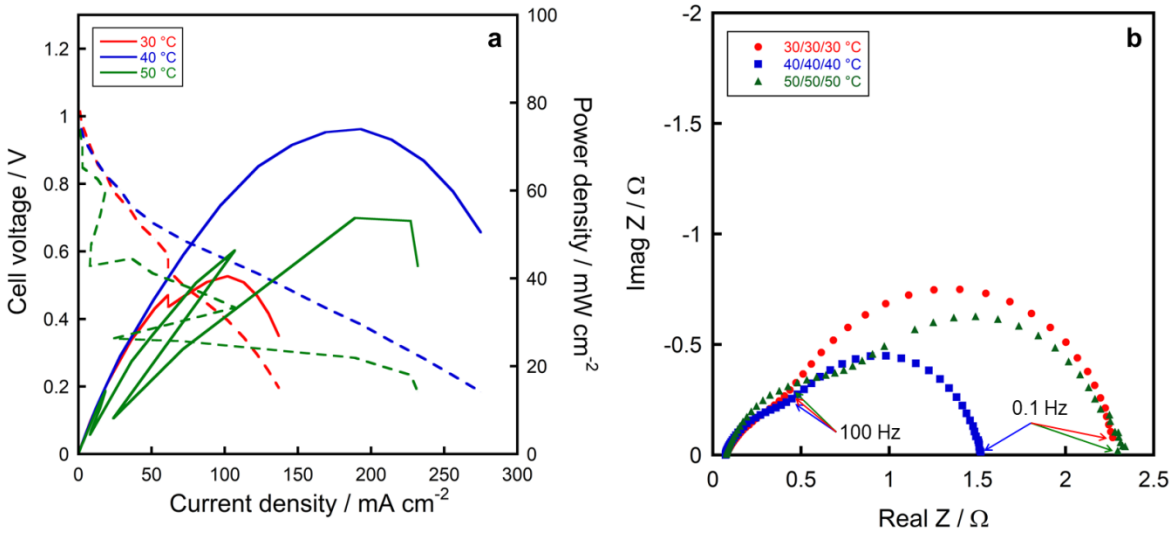

Figure 6.9 (a) Fuel cell polarization curves (dashed) and power density curves (solid), and (b) impedance spectra at *ca.* 0.86 V *versus* NHE at cell temperatures of 30 °C (red circles), 40 °C (blue squares), and 50 °C (green triangles). Fuel cell operating conditions: 1/1 mol/mol H_2/O_2 at 100% RH and ambient pressure.

To study the erratic behavior at lower current densities, EIS was conducted *in operando* to analyze polarization resistances of the PTP MEAs under 0.86 V *vs.* NHE at different temperatures. Figure 9b shows the electrochemical impedance response of the PTP MEA under different temperatures. All spectra exhibit two depressed capacitive semi-circles. As mentioned previously, the high-frequency semi-circle represents the anode processes and the intermediate-frequency semi-circle represents the cathode processes. The high-frequency semi-circle is similar between 30 and 40 °C; however, the intermediate-frequency semi-circle decreases in size at 40

°C, which suggests that at 40 °C, the oxygen reduction reaction is more facile (*i.e.*, less resistive). As the temperature further increases to 50 °C, both semi-circles increase in size and the high-frequency semi-circle is slightly shifted to a lower frequency. These results are further supported by the power density results shown previously, where fuel cell operation at 40 °C has the highest maximum power density (*i.e.*, lowest resistance).

Omasta *et al.*[187] suggested that due to the reactant consumption of water in the cathode and production of water in the anode of AFCs, excessive water dehydration and flooding can occur in the cathode and anode, respectively, and overall decrease fuel cell performance. To further explore this, the fuel cell humidity was systematically changed by maintaining a cell temperature of 40 °C and changing the anode and cathode gas line temperatures. Figure 6.10a shows fuel cell performances (polarization and power curves; hydrogen/oxygen at ambient pressure at 40 °C) of optimized PTP MEA with different anode/cell/cathode temperatures. At 40/40/40 °C (*i.e.*, 100% relative humidity), the maximum power density is 83.3 mW cm^{-2}. At 41/40/41 °C (*i.e.*, 105% relative humidity), the maximum power density decreases to 61.6 mW cm^{-2}, which suggests that the presence of liquid water in the cell results in performance loss. At 39/40/39 °C (*i.e.*, 95% relative humidity), the maximum power density decreases to 56.9 mW cm^{-2} and the polarization curve is erratic at low current densities, which suggests that there are kinetic polarization losses due to the lack of water in the cell. At 39/40/41 °C (*i.e.*, 95% relative humidity on the anode and 105% relative humidity on the cathode), the power density further decreases to 46.5 mW cm^{-2}. These results suggest that a fully-humidified cell produces the best performance for PTP MEAs. To further explore the impact of relative humidity on the anode and cathode, EIS was conducted *in operando* to analyze polarization resistances of the PTP MEAs under 0.86 V *vs.* NHE at different anode/cell/cathode temperatures. Figure 6.10b shows the electrochemical impedance

response of the PTP MEA under different anode/cell/cathode temperatures. All spectra exhibit two depressed capacitive semi-circles; however, the high-frequency semi-circle is shifted towards the intermediate-frequency region, which results in the appearance of one elongated depressed semi-circle and suggests the time constants of the two processes are similar. In general, changing the anode/cathode gas line temperatures results in an increase in electrode resistance. These results suggest that proper cell humidification is required to minimize electrode resistances that affect hydroxide ion transport between the electrodes and the membrane. These results are supported by the maximum power density results, where any change in anode/cathode gas line temperatures resulted in a performance loss. Therefore, a fully humidified cell is the optimal fuel cell condition for PTP MEAs.

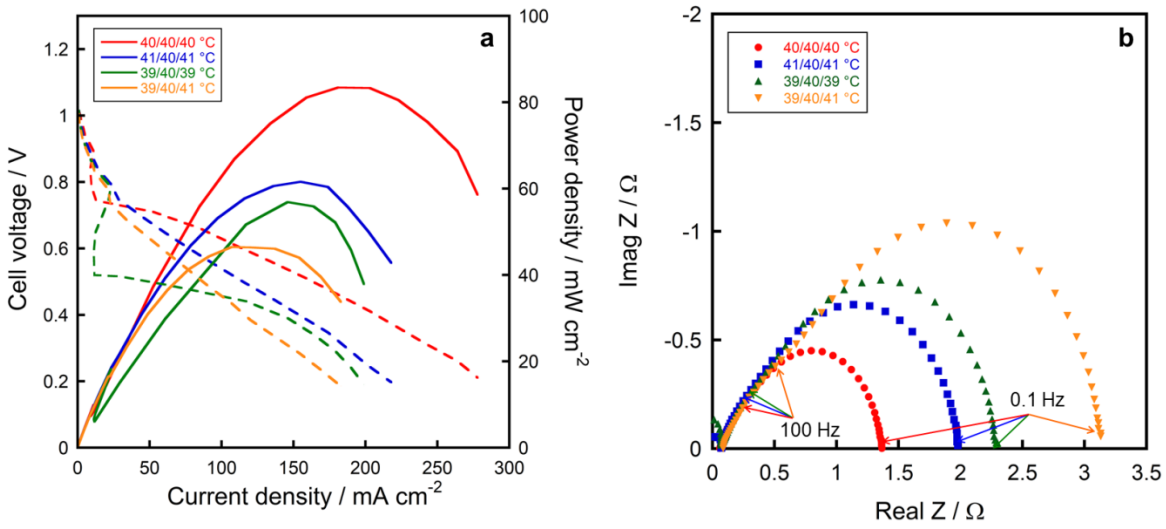

Figure 6.10 (a) Fuel cell polarization curves (dashed) and power density curves (solid), and (b) impedance spectra at *ca.* 0.86 V *versus* NHE at anode/cell/cathode temperatures of 40/40/40 °C (red squares), 41/40/41 °C (blue circles), 39/40/39 °C (green upward triangles), and 39/40/41 °C (orange downward triangles). Fuel cell operating conditions: 1/1 mol/mol H_2/O_2 at ambient pressure.

Figure 6.11 shows the normalized voltage and iR cell resistance for optimized PTP MEA (electrodes fabricated using 2/1 w/w methanol/water and 2/1 (Pt/C)/ionomer) under optimized fuel cell conditions (40 °C, 100% RH) under constant current density as function of time. The PTP AEMFC initially operated at a current density of 100 mA cm^{-2}. However, at t = 13.6 h, the cell was unable to maintain that current density and subsequently reduced to a current density of 73 mA cm^{-2}, and continued to operate for a total duration of at least 100 h. The voltage decay rate of the fuel cell operating under 73 mA cm^{-2} is 0.7 mV h^{-1}. The iR resistance, which can be used to monitor electrolyte resistance,[188] slightly increases from 63 mΩ to 93 mΩ, which suggests that the membrane is relatively stable under alkaline fuel cell operation. Overall, the PTP MEA operates under stable current density over time under 40 °C, 100% RH.

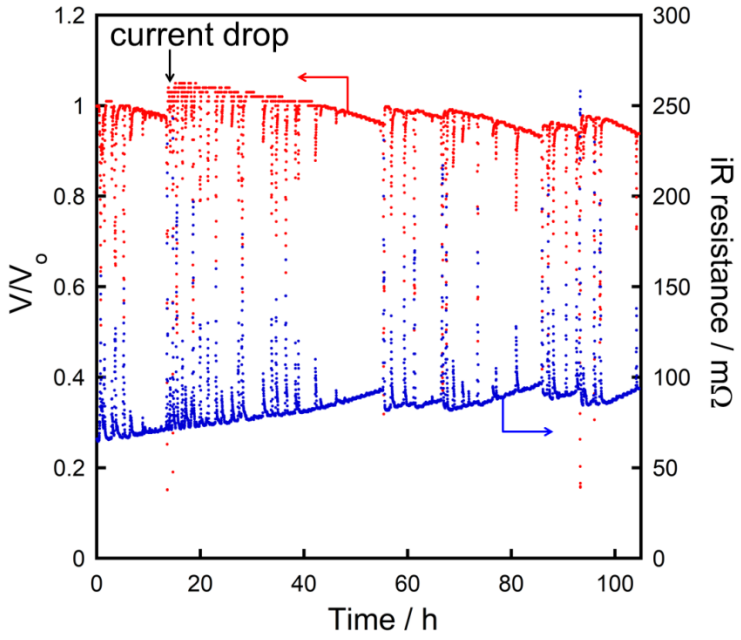

Figure 6.11 Normalized voltage (red) and iR resistance (blue) versus time of 0.4 mg_{Pt} cm^{-2} electrodes. Voltage is normalized by the initial voltage at t = 0 h (V_o). Fuel cell operating conditions: 1/1 mol/mol H_2/O_2 at 40°C, 100% RH, and ambient pressure.

6.4 Conclusions

In this study, PTP with methylpyrrolidinium cations were used as membranes and ionomers in AFC applications. PTP membranes demonstrated better performance and durability than commercial Fumatech membranes, which may be attributed to the stable methylpyrrolidinium cations in the PTP membrane *versus* the ubiquitous quaternary ammonium cation in the Fumatech membrane. Various compositions of methanol and water as the solvent and ionomer and catalyst in the solids in the catalyst ink solution were investigated. As the amount of water or ionomer increased in the catalyst ink solution, the maximum power density increased and then decreased due to significant changes in the morphology, specifically the more notable presence of the ionomer with increasing water or ionomer content. These observations are further supported by fuel cell resistance data where the cathode resistances decreased and then increased, suggesting that at low water or ionomer content, there is high ion transfer resistance and at high water or ionomer content, there is a high mass transfer resistance. Therefore, the optimum PTP catalyst ink composition was 2/1 w/w ionomer/catalyst and 2/1 w/w methanol/water. Fuel cell temperature and relative humidity were also varied to determine the effect of operating conditions on PTP MEAs. Overall, the fuel cell resistances were higher for operating conditions outside of 40 °C and 100% RH, which correlated with fuel cell performance results. Furthermore, the optimal PTP MEA produced a maximum power density of 83.3 mW cm^{-2} and lasted up to 100 h under 40 °C, 100% RH, suggesting that PTP MEAs may be suitable for long-term AFC performance.

CHAPTER VII

ELECTROSPUN PENTABLOCK TERPOLYMER NANOFIBERS/ELECTROSPRAYED CATALYST PARTICLE ELECTRODES FOR ALKALINE FUEL CELLS

7.1 Introduction

In Chapter 2, E/E electrodes demonstrated similar power density compared to conventional electrodes at lower Pt loadings, due to the highly porous network of nanofiber-nanoparticles that allows facile oxygen gas access to catalyst particles. Omasta *et al.*[189] suggested that proper water management can significantly improve AFC performance. The water balance in the fuel cell electrodes is different than the PEMFC in the cathode and anode due to the consumption of water at the cathode and generation of water at the anode. In Chapter 6, the fuel cell relative humidity was changed to determine if a lower or higher relative humidity will alleviate the problems mentioned by Omasta *et al.*[189] However, the best performance was still at 100% RH, suggesting that using airbrushed (conventional) PTP electrodes, 100% RH was the optimum fuel cell condition. Therefore, having a porous network may allow for rapid diffusion of water to the cathode and away from the anode, alleviating water starvation or flooding in the cathode and anode, respectively, that is not seen in Chapter 6. Here, in this Chapter, E/E electrodes using PTP nanofibers and Pt/C catalyst particles are used in the AFC. The morphology of the E/E electrodes is characterized and analyzed. The performance and durability of the E/E electrodes are investigated and compared to airbrushed (conventional) electrodes.

7.2 Experimental Methods

7.2.1 Materials

Ethanol (reagent grade), methanol (ACS reagent, ≥99.8%), and toluene (anhydrous, 99.8%) were purchased from Sigma-Aldrich. Poly(methyl methacrylate) (PMMA; M_W = 540,000 g mol^{-1}) was purchased from Scientific Polymer Products, Inc. 20 wt% platinum on carbon (Pt/C; Vulcan XC-72) were purchased from Premetek Co. The preparation of the pentablock terpolymer (PTP) and pentablock terpolymer films used in this study was previously described in Chapter 6. Gas diffusion layer (GDL; Sigracet 25BC) was purchased from Fuel Cells Etc. All materials were used as received. Deionized (DI) water with a resistivity of 16 MΩ cm was used as appropriate. Ultra-high purity grade nitrogen, ultra-high purity grade oxygen, and ultra-high purity grade hydrogen were purchased from Airgas. All gases were used for all fuel cell experiments.

7.2.2 Two-Needle Electrospinning/Electrospraying (E/E) Apparatus

A custom-designed E/E apparatus, as illustrated in Chapter 2 (Figure 2.1), consists of two high-voltage power supplies (CZE1000R, Spellman High Voltage Electronics Corporation and ES40P-10W/DAM, Gamma High Voltage Research, Inc.), two syringe pumps (NE-1000, New Era Pump Systems), two glass syringes (Pt. No. CG-3070-03, Chemglass Life Sciences), two syringe needles (i.d. = 0.024 in. (0.603 mm), Hamilton), poly(vinyl chloride) tubing (Pt. No. 30600-65, Cole-Parmer), poly(tetrafluoroethylene) tubing (Pt. No. 86510, Hamilton), luer lock needle adapter (Pt. No. 86511, Hamilton), and a grounded collector (cylindrical drum covered with aluminum foil, o.d. = 4.85 cm) connected to a motor (4IK25GN-SW2, Oriental Motor) to rotate the drum at 85 rpm during the E/E process. Two GDLs (*ca*. 3 cm × 3 cm) were adhered to

the drum, where catalyst nanoparticles and polymer nanofibers were electrosprayed and electrospun simultaneously onto the GDLs *via* the E/E process. The needle tip to collector distances, applied voltages, and solution flow rates were 10 and 8 cm, 16 and 12 kV, and 0.15 and 3.30 mL h^{-1} for the electrospinning and electrospraying processes, respectively.

7.2.3 Electrode Fabrication

The electrospraying catalyst ink solution used to fabricate E/E electrodes consisted of a base mixture of 40 mg of Pt/C catalyst, 500 mg of DI water, and 3440 mg of ethanol. For the E/E experiment with PTP in the electrospraying solution, 20 mg of PTP was first dispersed in 500 mg of DI water, followed by the addition of 40 mg of Pt/C catalyst and 3460 mg of ethanol. The resulting mixture was sonicated for 3 min at 35% amplitude (Q125, Qsonica) prior to electrospraying. The electrospinning polymer solution used to fabricate E/E electrodes was a 6 wt% 7/3 PTP/PMMA polymer solution, *e.g.*, 24 mg of PMMA, 56 mg of PTP, and 1300 mg of 4/1 w/w toluene/methanol solution. The solution was stirred under ambient temperature for at least 12 h to ensure complete dissolution of PTP and PMMA prior to electrospinning. The catalyst ink solution and the polymer solution were used in the electrospraying and electrospinning processes, respectively, to fabricate E/E electrodes as described in the previous section, and the Pt loading was controlled by the duration of the E/E process. Conventional (control) electrodes were prepared by dispersing 10 mg of PTP in 1000 mg of DI water, followed by addition of 20 mg Pt/C catalyst and 2970 mg of methanol, which corresponds to 2/1 w/w (Pt/C)/PTP in 3/1 w/w methanol/water. The mixture was sonicated for 3 min at 35% amplitude and subsequently airbrushed onto the GDL (*ca.* 25 mm (L) x 25 mm (W)) with an airbrush gun

(AEROPRO1, Aeroblend). This process was repeated to achieve the target Pt loading of 0.30 $mg_{Pt}\ cm^{-2}$.

7.2.4 Electrode Characterization

The morphology of the E/E electrodes was investigated with scanning electron microscopy (SEM; FEI Quanta 600 FE-SEM, 10 kV) using a working distance of 10 mm. Samples were sputter coated (Cressington 208 HR) with iridium (6 nm thickness) prior to SEM analysis. For each image, the diameters of 20 nanofibers and 20 nanoparticles were randomly selected and measured using ImageJ software for each electrode sample.

The Pt loading was measured with thermal gravimetric analysis (TGA; Q50, TA Instrument). A small portion of the electrode (*ca*. 4–6 mg) was heated in the TGA from ambient temperature to 900 °C at 10 °C min^{-1} in air at 60 mL min^{-1}. Since all components in the E/E electrode degrade below 800 °C with the exception of Pt, the Pt loading was determined by dividing the residual weight at 850 °C by the original area of the TGA sample. The average Pt electrode loading for each MEA was determined using 2 samples.

7.2.5 Membrane Electrode Assembly (MEA) and Fuel Cell Tests

Membrane electrode assemblies (MEAs) were fabricated by placing the PTP film between two catalyst-coated GDLs (anode and cathode) in the fuel cell without any heat pressing, which was placed between two serpentine flow field graphite plates (5 cm^2 flow area) separated by two 0.152 mm thick PTFE/fiberglass gaskets (Gasket Set #5, Scribner Associates, Inc.). The entire fuel cell assembly consisted of an MEA, two gaskets, and two flow plates placed between copper current collectors followed by endplates all held together by bolts with 2.8 N m of applied

torque. Fuel cell performance of each MEA was evaluated with a fuel cell test station (850e, Scribner Associates, Inc.). Fuel cell tests were conducted under ambient pressure with saturated (100% RH) anode and cathode flow rates of 0.2 L min^{-1} hydrogen and 0.2 L min^{-1} oxygen, respectively, corresponding to a stoichiometric ratio of 1:1 hydrogen/oxygen. The cathode gas, anode gas, and cell temperatures were all maintained at 30 °C. Fuel cell performance was recorded after a new MEA was fully activated. The activation process consisted of operating the MEA at 0.5 V for 1 h, followed by three cycles of 0.6 V and 0.4 V for 30 min at each voltage. The MEA was at steady state when no further increase in current density at a constant voltage was observed. After the MEA was fully activated and reached steady state, polarization curves (cell voltage *versus* current density) were collected from open circuit voltage (OCV) to 0.2 V at increments of 0.05 V every 5 min. Five polarization curves were collected to determine the average maximum power density.

7.2.6 Durability Tests

The fuel cell anode and cathode were supplied with 0.2 L min^{-1} hydrogen and 0.2 L min^{-1} oxygen, respectively. Temperatures of the cathode gas, anode gas, and cell were all maintained at 30 °C. MEAs were held at a constant current density (typically the current density at a voltage slightly lower than the voltage where maximum power density occurs) for at least 100 h. The voltage was recorded and normalized with the initial voltage at t = 0 h (V_o) for the duration of the durability test. The decay rate was calculated from the slope of the linear regression to the data in the first 13 h.

7.3 Results and Discussion

Alkaline fuel cell experiments with E/E electrodes with different ionomer content were conducted to evaluate the performance of PTP nanofibers on alkaline fuel cell performance. SEM images of the E/E catalyst layers are shown in Figure 7.1a–d, where Figure 7.1a,c corresponds to E/E catalyst layers fabricated using 0/1 PTP/(Pt/C) in the electrospraying solution and Figure 7.1b,d corresponds to E/E electrodes fabricated using 1/2 PTP/(Pt/C) in the electrospraying solution. All E/E catalyst layers show a highly porous network of randomly arranged nanofibers and particle aggregates, which promotes facile gas transport to Pt sites for reactions to occur. The E/E electrodes fabricated using 1/2 PTP/(Pt/C) in the electrospraying solution has polymer beads, shown in Figure 7.1d, which suggests that the PTP and Pt/C catalyst are not well mixed in the solution and results in electrospraying of PTP beads and Pt/C catalyst particles.

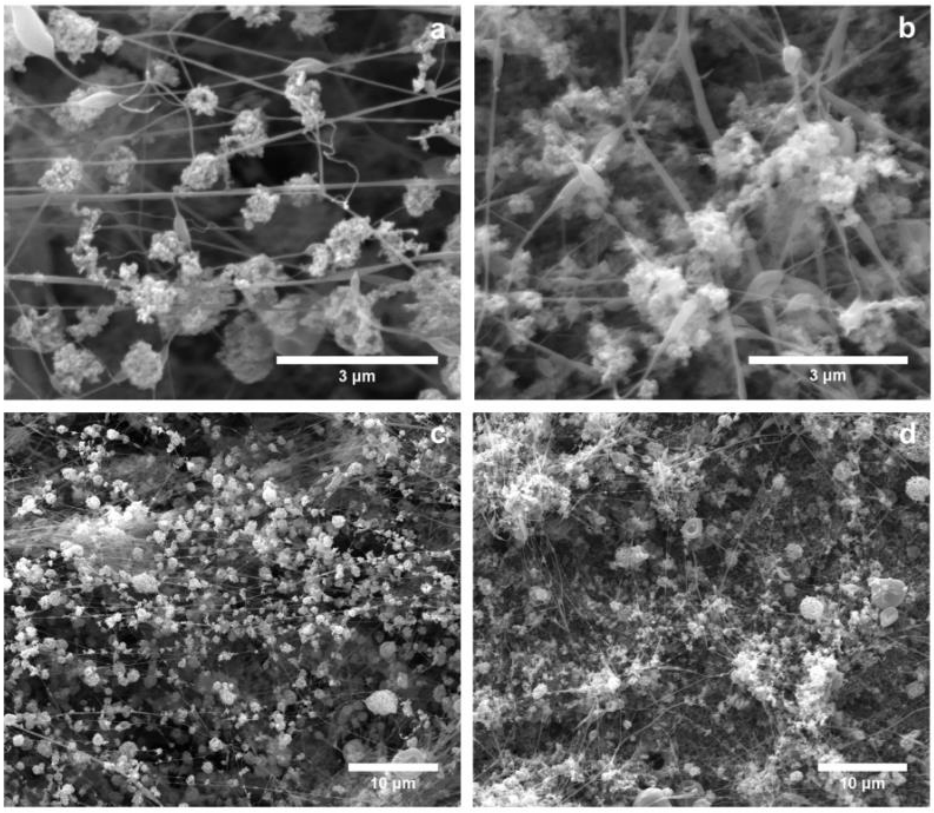

Figure 7.1 SEM images of E/E electrodes (a,c) 0/1 PTP/(Pt/C) and (b,d) 1/2 PTP/(Pt/C) in the electrospray. (a,b) X 5000 magnification, scale bar = 10 µm; (c,d) X 30000 magnification, scale bar = 3 µm.

Figure 7.2 shows the average fiber diameters and particle diameters of the images shown in Figure 7.1a–d. The average fiber diameters are 117 ± 83 nm and 121 ± 97 nm for E/E electrodes fabricated using 0/1 PTP/(Pt/C) and 1/2 PTP/(Pt/C) in the electrospraying solution, respectively. The average particle diameters are 0.84 ± 0.34 µm and 0.91 ± 0.60 µm for for E/E electrodes fabricated using 0/1 PTP/(Pt/C) and 1/2 PTP/(Pt/C) in the electrospraying solution, respectively. The average fiber and particle diameters are similar for all E/E experiment, which emphasizes the ability of the E/E technique to maintain morphology as mentioned previously in Chapter 2.

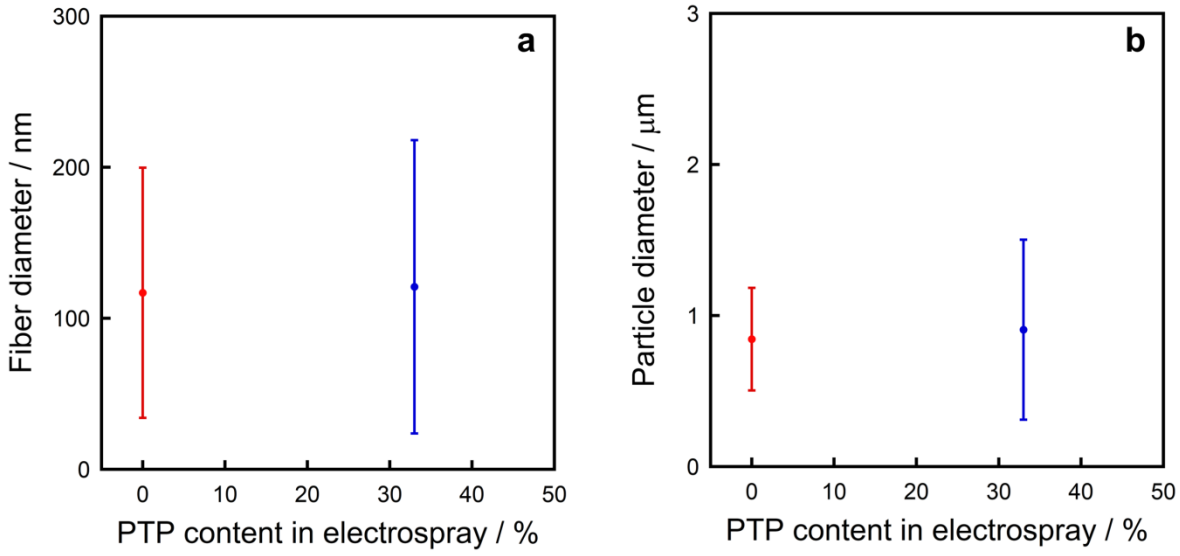

Figure 7.2 (a) Fiber diameter and (b) particle diameter distributions of E/E electrodes as a function of PTP content in the electrospray: 0/1 PTP/(Pt/C) (red) and 1/2 PTP/(Pt/C) (blue).

Figure 7.3 shows fuel cell performances (polarization and power curves; hydrogen/oxygen at ambient pressure at 30 °C) for airbrushed (conventional) electrodes with 0.30 mg_{Pt} cm^{-2} and E/E MEA with 0.10 mg_{Pt} cm^{-2}. The maximum power density for the airbrushed MEA (38.0 mW cm^{-2}) is slightly higher than that of E/E MEAs (31.7 mW cm^{-2} and 30.1 mW cm^{-2} for E/E electrodes fabricated using 0/1 PTP/(Pt/C) and 1/2 PTP/(Pt/C) in the electrospraying solution, respectively). Interestingly, the maximum power densities are within 10 mW cm^{-2} between the airbrushed and E/E MEAs, despite three times higher Pt loading for the airbrushed electrodes compared to the E/E electrodes. Moreover, the Pt utilization is 68–75% lower for the E/E electrodes (4.2 and 5.4 mg_{Pt} W^{-1} for E/E electrodes fabricated using 0/1 PTP/(Pt/C) and 1/2 PTP/(Pt/C) in the electrospraying solution, respectively) compared to that for the airbrushed electrodes (16.8 mg_{Pt} W^{-1}). These results suggest that E/E electrodes can produce similar power densities to airbrushed electrodes with lower overall Pt loading.

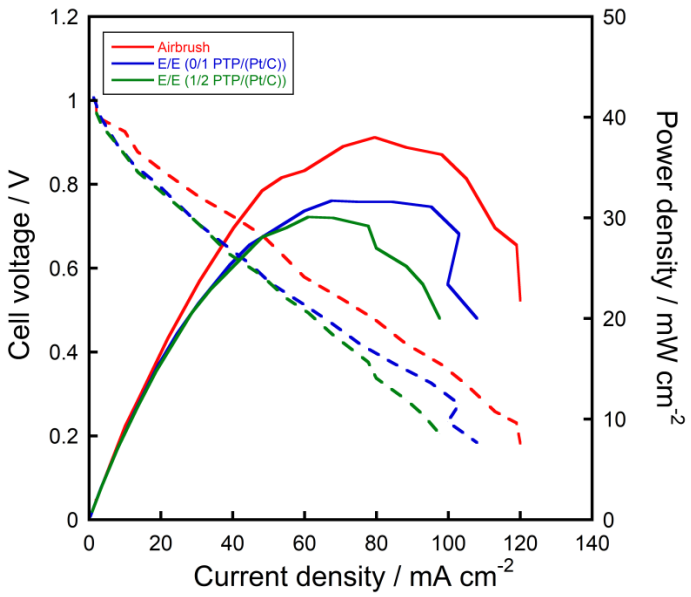

Figure 7.3 Fuel cell polarization curves (dashed) and power density curves (solid) of airbrushed electrodes (red), E/E electrodes with 0/1 PTP/(Pt/C) in the electrospray (blue), and E/E electrodes with 1/2 PTP/(Pt/C) in the electrospray (green). Fuel cell operating conditions: 1/1 mol/mol H_2/O_2 at 30 °C, 100% RH, and ambient pressure.

The airbrushed (control) MEA was able to maintain a constant current density (50.0 mA cm^{-2}) for 80.0 h, as shown in Figure 7.3a, before it decreased to 27% of the initial current density (36.4 mA cm^{-2}). However, the E/E MEA with E/E electrodes fabricated using 0/1 PTP/(Pt/C) was only able to maintain a constant current density (50.0 mA cm^{-2}) for 13.5 h and then dropped to 41% of the initial current density (20.6 mA cm^{-2}) as shown in Figure 7.3a. Moreover, the E/E MEA with E/E electrodes fabricated using 1/2 PTP/(Pt/C) was not able to maintain a constant current density of 50 mA cm^{-2} and held an initial current density of 40.5 mA cm^{-2} for 66.9 h and then continually decreased until it dropped to 35% of the initial current density (26.5 mA cm^{-2}). The short-term voltage decay rate (t = 0–13 h) is similar between the airbrushed MEA (3.9 mV h^{-1}) and E/E MEAs (3.7 mV h^{-1}).

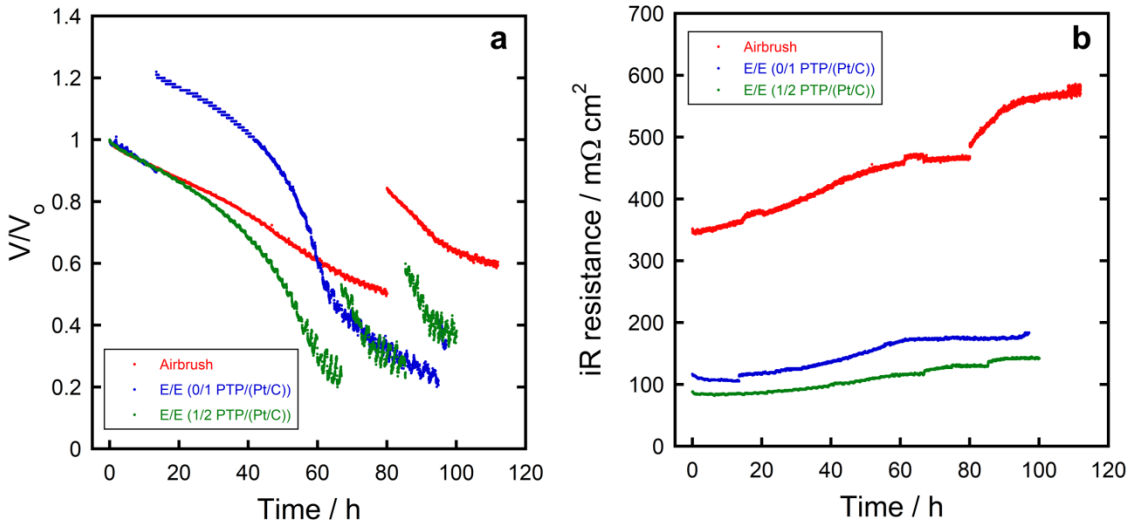

Figure 7.4 (a) Normalized voltage and (b) iR resistance *versus* time of airbrushed electrodes (red), E/E electrodes with 0/1 PTP/(Pt/C) in the electrospray (blue), and E/E electrodes with 1/2 PTP/(Pt/C) in the electrospray (green). Voltage is normalized by the initial voltage at t = 0 h. Fuel cell operating conditions: 1/1 mol/mol H_2/O_2 at 30 °C, 100% RH, and ambient pressure.

These results show lower life-time stability for the E/E MEA compared to the airbrushed (conventional) MEA. One possible reason may be due to the low Pt loading in the E/E MEAs. Gazdzicki *et al.*[190] demonstrated that for PEMFCs with electrode Pt loadings < 0.2 mg_{Pt} cm^{-2} suffered a dramatic decrease in durability at current densities > 0.4 A cm^{-2}, suggesting that low Pt loading electrodes are more susceptible to irreversible degradation losses. Therefore, durability losses seen in E/E MEAs may be attributed to the low Pt loading in the electrodes. Table 7.1 summarizes these results: maximum power density, average electrode Pt loading, Pt utilization, and decay rate.

Table 7.1 Pt loading, maximum power density, Pt utilization, and decay rate for airbrushed and E/E electrodes.

Technique	Pt loading (mg_{Pt} cm^{-2})	Max power density[c] (mW cm^{-2})	Pt utilization[d] (mg_{Pt} W^{-1})	Decay rate[e] (mV h^{-1})
Airbrush	0.33 ± 0.02	40.0 ± 1.3	16.8	3.9
E/E[a]	0.07 ± 0.02	32.5 ± 0.6	4.2	3.7
E/E[b]	0.08 ± 0.03	31.6 ± 1.0	5.4	3.7

[a]0/1 PTP/(Pt/C) in electrospraying solution.
[b]1/2 PTP/(Pt/C) in electrospraying solution.
[c]Measured at 1/1 mol/mol H_2/O_2 30 °C, ambient pressure.
[d]Calculated using the total Pt loading in the MEA.
[e]Calculated using initial voltage (t = 0 h) and final voltage (t = 13 h).

Interestingly, the initial iR resistance (t = 0 h) is 67–75% lower for the E/E MEAs (117 and 88 mΩ cm^2 for E/E electrodes fabricated using 0/1 PTP/(Pt/C) and 1/2 PTP/(Pt/C) in the electrospraying solution, respectively) compared to the airbrushed MEA (351 mΩ cm^2), despite a higher maximum power density for the airbrushed MEA. The iR resistance is generally attributed to the electrolyte membrane resistance, but may have some contributions from electrolyte resistance in the electrode.[44] Therefore, a lower iR resistance could suggest a better electrolyte ion transport at the membrane-electrode interface that allows for similar power densities between airbrushed MEA and the E/E MEAs, despite a higher Pt loading for the airbrushed (conventional) MEA. Thus, these results suggest that the nanofiber-nanoparticle catalyst layer network may improve the membrane-electrode interface, leading to similar power densities at a lower Pt loading.

7.4 Conclusions

E/E electrodes were fabricated and utilized in the AFC using PTP nanofibers and Pt/C catalyst particles. E/E MEAs demonstrated similar power densities compared to an airbrushed

(conventional) MEA at almost one-third of the Pt loading, which revealed higher Pt utilization for the E/E MEAs. In addition, the initial decay rate (within the first 13 h) was similar for the airbrushed and E/E MEAs, suggesting that the E/E electrodes are durable in the beginning. However, E/E MEAs were not able to hold the same current density (50 mA cm^{-2}) for the same amount of time as the airbrushed MEA, which may be due to the low Pt loading in the E/E electrodes. Moreover, the iR resistance is overall lower for the E/E MEAs throughout the entire duration of the durability test, despite a lower performance, which warrants deeper investigation into the interface between E/E catalyst layers and PTP membranes. Future work on improving the E/E electrodes with PTP nanofibers and Pt/C catalyst particles and understanding the effect of the nanofiber-nanoparticle network on AFC performance will elucidate the primary transport (ion and mass transfer) mechanisms in AFC electrodes.

CHAPTER VIII

CONCLUSIONS AND FUTURE OUTLOOK

8.1 Summary

Investigating and understanding transport resistances within fuel cells is important in developing low-cost next-generation hydrogen fuel cells. In this work, transport resistances in fuel cells using nanofiber-nanoparticle electrodes were investigated and new polymer materials with promising conductivity (*e.g.*, ion transport) were applied in PEMFCs and AFCs.

E/E electrodes as a function of Nafion content in the electrospraying were developed to investigate the effect of Nafion content on catalyst particle aggregates. This study allowed for the sole investigation of the effect of Nafion surrounding catalyst particle aggregates, while maintaining morphology (difficult to achieve using conventional fabrication techniques). E/E MEAs can produce similar power density at a lower Pt loading compared to conventional MEAs due to the unique nanofiber-nanoparticle structures. An optimum total Nafion content of 62 wt% in the E/E electrodes, which differs from the optimum 30 wt% in conventional electrodes, produced the highest power density, suggesting that there is a balance between ion transfer (proton transport) and mass transfer (oxygen gas transport) within the catalyst particle aggregates to achieve the highest maximum power density.

To advance the development of low-cost fuel cells, a needleless electrospinning technique was developed in this study (in order to increase the production rate of E/E electrodes). Fiber mats with different Nafion content using needle electrospinning and needleless electrospinning techniques were compared. Overall, needleless electrospun fibers also had higher Young's modulus and proton conductivity compared to needle electrospun fibers. Moreover, needleless

electrospinning can produce nanofibers at an order of magnitude higher than needle electrospinning, suggesting that needleless electrospinning can be used for commercial purposes. Preliminary testing of these needleless electrospun nanofibers as fuel cell electrodes demonstrated that needleless electrospun nanofibers can produce similar power densities as E/E electrodes. Thus, needleless electrospun nanofibers can be applied in fuel cells, suggesting that needleless electrospinning, combined with a high catalyst particle deposition rate technique, could be developed into a novel process for high production rate of nanofiber-nanoparticle electrodes.

To lower fuel cell costs even further, NEXAR (a commercial sulfonated pentablock terpolymer) with different ion exchange capacities (1.0, 1.5, and 2.0) was investigated and tested as membranes and ionomers in this study. These NEXAR materials demonstrated higher conductivities than the commercial perfluorinated membrane (Nafion) at all temperatures studied, suggesting promising application in PEMFCs. NEXAR-1.0 proved to be the most durable as evidenced by fuel cell performance tests and *post mortem* images. Analysis of the electrochemical impedance spectra revealed that there was a two-fold increase in membrane resistance for the NEXAR-1.0 MEA compared to the Nafion MEA, despite higher *ex situ* conductivity results. Thus, NEXAR materials demonstrate potential as membranes and ionomers in PEMFC; however, further improvements in the MEA are needed.

The unsulfonated version of the pentablock terpolymer (PTP) was used as a precursor for a brominated PTP that was functionalized with methylpyrrolidinium cations for the AFC. The PTP with methylpyrrolidinium cations was used as the anion exchange membrane (AEM) and ionomer for AFCs. In comparison with commercial AEMs (Fumapem), the PTP demonstrated better stability and performance, suggesting that PTP can be applied in AFCs. Studies in

optimizing the solids and solvent compositions in the electrodes further improved the performance of PTP MEAs. The PTP MEA demonstrated a durability of 100 h, which suggests promising application of PTP in long-term durable AFCs. E/E electrodes were also fabricated, characterized, and applied in AFCs using PTP nanofibers. Preliminary testing of E/E electrodes in AFCs reveals lower iR resistance, suggesting that the nanofiber-nanoparticle network lowers electrolyte membrane-electrode resistance. These results suggest that PTP can be used as membranes, ionomers, and nanofibers for AFCs.

8.2 Future Directions

The work presented in this dissertation can be expanded into multiple directions to further progress the commercialization of low-cost hydrogen fuel cells. A novel needleless electrospinning/ultrasonic spraying apparatus is proposed to develop low-cost fuel cell electrodes at a high production rate. Further exploration using the E/E technique to study nanofiber-nanoparticle electrodes focus on the nanofiber properties and ultra-thin catalyst layers. To improve future block copolymers for AFC applications, a better understanding of the membrane-electrode interfaces would be of interest, as well as alternative polymer compositions based on the results from the PTP studies.

8.2.1 High Production Rate of Nanofiber-Nanoparticle Electrodes

For the development of a low-cost PEMFC, the development of a needleless electrospinning and ultrasonic spraying apparatus, shown in Figure 8.1, can lead to high production rate of nanofiber-nanoparticle electrodes with highly uniform nanofibers and uniformly distributed particles, similar to the electrodes shown in Chapter 2, for commercial use. The needleless

electrospinning is similar to the one in Chapter 3 and is placed directly below a rotating grounded collector. Polymer foam is generated by passing compressed air through a glass fritted funnel. The rotating collector is supported by two stands that allow the adjustment of the height of the collector from the ground, offering versatile polymer foam-to-collector distances. An ultrasonic spraying nozzle is placed directly above the rotating collector, where catalyst ink solution is fed into and sonicated using compressed air, to distribute catalyst particles onto the collector. The simultaneous operation of needleless electrospinning and ultrasonic spraying should generate similar nanofiber-nanoparticle mats as the ones in Chapter 2; however, the production rate should theoretically be higher based on the results from Chapter 3.

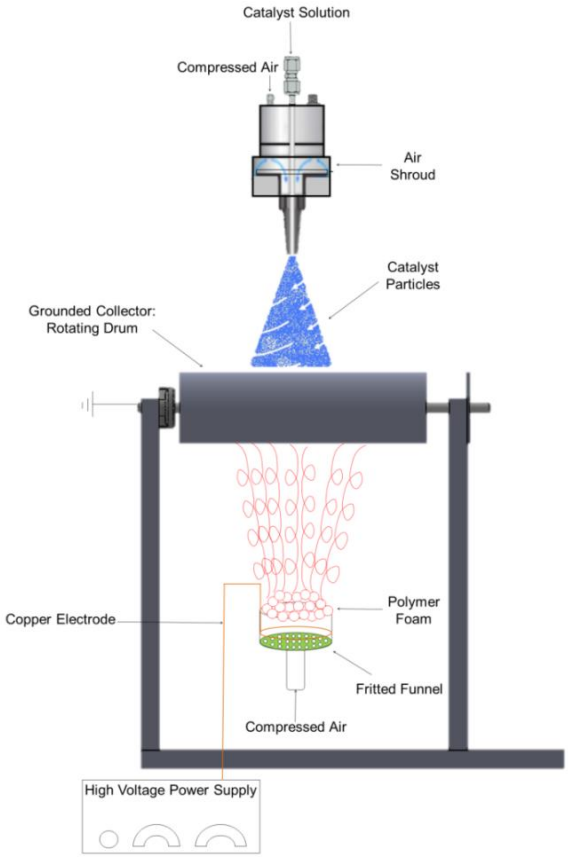

Figure 8.1 Schematic of simultaneous needleless electrospinning and ultrasonic spraying. Ultrasonic spraying is adapted from ref. [191].

8.2.2 Nanofiber Purity, Size, and Durability

In addition, the results from Chapter 3 introduced the potential to use high-purity Nafion nanofibers in fuel cell electrodes using the needleless electrospinning technique. Dong *et al.*[140] demonstrated that higher purity and thinner Nafion nanofibers can increase the proton conductivity by an order of magnitude. Therefore, optimizing Nafion nanofibers (*e.g.*, purity and size) could enhance fuel cell performance by improving the proton conductivity in the catalyst layers. Several investigators have demonstrated electrospinning of Nafion nanofibers with different carrier polymers (*e.g.*, poly(ethylene oxide), poly(acrylic acid), poly(vinylidene fluoride)). However, the effect of the carrier polymer on the properties of the Nafion nanofibers has yet to be determined. It would be of interest to do a systematic study of the effect of carrier polymer on Nafion nanofiber properties (*e.g.*, proton conductivity, Young's modulus, elongation-at-break, nanofiber morphology) and their performance in fuel cells (*e.g.*, power density, catalyst layer resistance) to determine if a specific carrier polymer has benefits due to its molecular structure (*i.e.*, synergistic effect between Nafion and carrier polymer). Moreover, the durability of these nanofiber-nanoparticle electrodes have yet to be determined; therefore, dynamic fuel cell tests (*i.e.*, cycling between different voltages) for long periods of time (*e.g.*, >10,000 h) will demonstrate the life cycle of these nanofiber-nanoparticle electrodes under practical environments (*e.g.*, daily fuel cell vehicle operation). The results from this study could further emphasize the promise and use of nanofiber-nanoparticle electrodes in commercial fuel cells.

8.2.3 Ultra-Thin Catalyst Layers

Another potential area of interest is in the development of ultra-thin (<1 μm) nanofiber-nanoparticle catalyst layers using the E/E technique. Multiple studies have developed thin catalyst layers (1 – 10 μm) as a potential method to reduce Pt loading and fuel cell resistance without significant losses in fuel cell performance.[13, 98, 192-194] Recently, Zeng *et al.*[195] developed an ionomer-free ultra-thin catalyst layer using PtCo bimetallic nanotube arrays with comparable power densities to and better durability than a commercial catalyst-coated membrane at half the Pt loading, suggesting that for nanostructured ultra-thin catalyst layers, water serves as a proton conductor. These results suggest that ultra-thin (<1 μm) catalyst layers could open new opportunities to study transport mechanisms on a nanoscale level. Using the E/E technique, ultra-thin catalyst layers could be developed using thinner nanofibers and shorter deposition times. The dispersion of the catalyst particles as well as nanofiber/particle ratio would be of interest to further explore the impact of the morphology of E/E electrodes on fuel cell performance. Cross-section of the electrodes by freeze-fracturing the electrode in liquid nitrogen, then quickly cutting the electrode with a sharp blade will allow for analysis of the thickness of the E/E catalyst layers *via* SEM. The results of this study can provide insight into developing super-low Pt loadings (<0.01 mg Pt cm^{-2}).

8.2.4 Membrane Gas Crossover

Further exploration of the PTP as a membrane in PEMFCs and AFCs includes an in-depth study on the effect of membrane thickness on membrane resistances (*e.g.*, gas crossover), analogous to the study conducted by Jiang *et al.*[45] Testing different membrane thicknesses can identify the minimum thickness for PTP membranes before gas crossover significantly affects

fuel cell power performance. To further investigate the interface between the membrane and electrode, SEM of the MEA cross-sections can provide visual information on the physical bonding between the electrode and membrane before and after fuel cell operation. MEA cross-sections can be obtained by freeze-fracturing the MEA in liquid nitrogen for several hours, then quickly cutting the MEA with a sharp blade or by embedding the MEA in an epoxy resin and cryo-microtoming to create several thin sections. The results from this study will give insight in the gas permeability of PTP membranes for PEMFCs and AFCs.

8.2.5 Anion Exchange Ionomer-Catalyst Interactions

Studies in AFCs are continuing to grow and with few studies in understanding the ionomer-catalyst interactions in AFC electrodes, the results presented in this dissertation is a starting point to understand the role of the ionomer and catalyst in AFC electrodes using PTP. Omasta *et al.*[196] employed carbon monoxide stripping to measure the electrochemical surface area of AFC electrodes. Therefore, cyclic voltammetry tests using carbon monoxide can reveal information about the triple phase boundaries by quantifying the electrochemical surface area. Moreover, detailed analysis of the Tafel slopes from linear sweep voltammetry experiments may reveal information about the effect of the ionomer on the kinetics of the hydrogen oxidation or oxygen reduction reactions. In addition, investigating different ionomer/catalyst ratios and different catalysts in with these electrochemical techniques can provide insight towards an optimal ionomer/catalyst combination. The results from this study will determine the affinity of the PTP ionomer with different catalysts and give insight into how the PTP ionomer interacts with different catalysts.

8.2.6 Degradation Mechanisms

Investigating the degradation mechanisms of these new PTP materials under alkaline fuel cell operation is also of interest. Rotating disk electrode (three-electrode) experiments can provide further insight in the compatibility of these new PTP materials as an ionomer with different catalysts in highly basic environments. Multiple linear sweep voltammetry tests at different time points for an extended period of time (*e.g.*, 500 h) in solutions of different basicity levels may also determine the durability of the PTP as an ionomer. Identifying new electrochemical reduction/oxidation peaks in cyclic voltammetry tests and correlating them with specific electrochemical reactions can give insight into possible degradation mechanisms. These *ex situ* experiments will provide guidance and support in developing cyclic voltammetry experiments for AFCs to understand degradation mechanisms occurring within the fuel cell. Mass spectroscopy of the fuel cell effluent may also provide information in regards to the chemical byproducts from degradation. The results from this study will provide information on possible degradation mechanisms using PTP as an ionomer and membrane in AFC applications.

8.2.7 Alternative Polymer Compositions

New polymer backbone and cation combinations are another area of exploration to develop high-performing long-lasting membranes for AFC operation. In addition, different compositions of the blocks of the PTP presented in this dissertation could lead to better AFC performance. Reducing the amount of rubber content (*i.e.*, ethylene-propylene block) could improve performance at higher temperatures; however, the membrane will become more brittle. Water may act as a plasticizer while casting the polymer solution under humidified solution and prevent cracks in the film. Moreover, embedding the lower rubber content PTP into a porous material,

such as a nanofiber mat, may provide mechanical support. Therefore, casting the polymer solution on top of a porous support material under humidified conditions may result in a reinforced membrane that can be used in AFC applications. Other modifications to the PTP include covalently attaching multiple cation side groups. Recently, several investigators have developed polymer materials with multiple cation side groups as a way to increase the IEC *i.e.*, (increase ion conductivity) without increasing the degree of functionalization to lessen undesirable AEM properties (*e.g.*, higher swelling ratio), typically associate with high IEC.[197-200] Therefore, attaching multiple cation side groups in PTPs may improve the mechanical properties and develop well-segregated phases in the morphology (*i.e.*, better ionic networks) due to a higher density of ion groups in one block. The results from this study will guide future modifications of PTPs as membranes and ionomers in AFC applications.

REFERENCES

1. Agency, U. S. E. P., Inventory of Us Greenhouse Emissions and Sinks: 1990-2015. **2018**, 10.

2. Energy, U. S. D. o., Comparison of Fuel Cell Technologies. **2016**.

3. Wilson, A. K., G.; Papageorgopoulos, D., Fuel Cell System Cost - 2017. *DOE Hydrogen and Fuel Cells Program Record* **2017**, 10.

4. Orfanidi, A.; Madkikar, P.; El-Sayed, H. A.; Harzer, G. S.; Kratky, T.; Gasteiger, H. A., The Key to High Performance Low Pt Loaded Electrodes. *J Electrochem Soc* **2017,** *164* (4), F418-F426.

5. Sung, M. T.; Chang, M. H.; Ho, M. H., Investigation of Cathode Electrocatalysts Composed of Electrospun Pt Nanowires and Pt/C for Proton Exchange Membrane Fuel Cells. *J Power Sources* **2014,** *249*, 320-326.

6. Wang, F.; Yang, D.; Li, B.; Zhang, H.; Hao, C.; Chang, F.; Ma, J., Investigation of the Recoverable Degradation of Pem Fuel Cell Operated under Drive Cycle and Different Humidities. *International Journal of Hydrogen Energy* **2014,** *39* (26), 14441-14447.

7. Wasterlain, S.; Candusso, D.; Hissel, D.; Harel, F.; Bergman, P.; Menard, P.; Anwar, M., Study of Temperature, Air Dew Point Temperature and Reactant Flow Effects on Proton Exchange Membrane Fuel Cell Performances Using Electrochemical Spectroscopy and Voltammetry Techniques. *J Power Sources* **2010,** *195* (4), 984-993.

8. Kim, K. H.; Lee, K. Y.; Lee, S. Y.; Cho, E.; Lim, T. H.; Kim, H. J.; Yoon, S. P.; Kim, S. H.; Lim, T. W.; Jang, J. H., The Effects of Relative Humidity on the Performances of Pemfc Meas with Various Nafion (R) Ionomer Contents. *International Journal of Hydrogen Energy* **2010,** *35* (23), 13104-13110.

9. Pedroza, O. J. O.; Dutra, J. C.; Picciani, P. H. S.; Dias, M. L., Morphology and Proton Conductivity of Composite Membranes Based on Poly(Styrene Sulfonic Acid-Maleic Anhydride) Nanofibers Prepared by Electrospinning. *Ionics* **2015,** *21* (3), 755-764.

10. Subramanian, C.; Giotto, M.; Weiss, R. A.; Shaw, M. T., Chemical Cross-Linking of Highly Sulfonated Polystyrene Electrospun Fibers. *Macromolecules* **2012,** *45* (7), 3104-3111.

11. Peng, K. J.; Lai, J. Y.; Liu, Y. L., Nanohybrids of Graphene Oxide Chemically-Bonded with Nafion: Preparation and Application for Proton Exchange Membrane Fuel Cells. *J Membrane Sci* **2016,** *514*, 86-94.

12. O'Hayre, R.; Prinz, F. B., The Air/Platinum/Nafion Triple-Phase Boundary: Characteristics, Scaling, and Implications for Fuel Cells. *J Electrochem Soc* **2004,** *151* (5), A756-A762.

13. Wilson, M. S.; Gottesfeld, S., Thin-Film Catalyst Layers for Polymer Electrolyte Fuel-Cell Electrodes. *J Appl Electrochem* **1992,** *22* (1), 1-7.

14. Suzuki, T.; Kudo, K.; Morimoto, Y., Model for Investigation of Oxygen Transport Limitation in a Polymer Electrolyte Fuel Cell. *J Power Sources* **2013,** *222*, 379-389.

15. Suzuki, T.; Hashizume, R.; Hayase, M., Effect of Blending Carbon Nanoparticles and Nanotubes on the Formation of Porous Structure and the Performance of Proton Exchange Membrane Fuel Cell Catalyst Layers. *J Power Sources* **2015,** *286*, 109-117.

16. Jung, C. Y.; Yi, S. C., Improved Polarization of Mesoporous Electrodes of a Proton Exchange Membrane Fuel Cell Using N-Methyl-2-Pyrrolidinone. *Electrochim Acta* **2013,** *113*, 37-41.

17. Ngo, T. T.; Yu, T. L.; Lin, H. L., Influence of the Composition of Isopropyl Alcohol/Water Mixture Solvents in Catalyst Ink Solutions on Proton Exchange Membrane Fuel Cell Performance. *J Power Sources* **2013,** *225*, 293-303.

18. Gode, P.; Jaouen, F.; Lindbergh, G.; Lundblad, A.; Sundholm, G., Influence of the Composition on the Structure and Electrochemical Characteristics of the Pefc Cathode. *Electrochim Acta* **2003,** *48* (28), 4175-4187.

19. Passalacqua, E.; Lufrano, F.; Squadrito, G.; Patti, A.; Giorgi, L., Nafion Content in the Catalyst Layer of Polymer Electrolyte Fuel Cells: Effects on Structure and Performance. *Electrochim Acta* **2001,** *46* (6), 799-805.

20. Sun, C. N.; More, K. L.; Veith, G. M.; Zawodzinski, T. A., Composition Dependence of the Pore Structure and Water Transport of Composite Catalyst Layers for Polymer Electrolyte Fuel Cells. *J Electrochem Soc* **2013,** *160* (9), F1000-F1005.

21. Uchida, M.; Aoyama, Y.; Eda, N.; Ohta, A., Investigation of the Microstructure in the Catalyst Layer and Effects of Both Perfluorosulfonate Ionomer and Ptfe-Loaded Carbon on the Catalyst Layer of Polymer Electrolyte Fuel Cells. *J Electrochem Soc* **1995,** *142* (12), 4143-4149.

22. Lee, S. J.; Mukerjee, S.; McBreen, J.; Rho, Y. W.; Kho, Y. T.; Lee, T. H., Effects of Nafion Impregnation on Performances of Pemfc Electrodes. *Electrochim Acta* **1998,** *43* (24), 3693-3701.

23. Davis, E. M.; Stafford, C. M.; Page, K. A., Elucidating Water Transport Mechanisms in Nafion Thin Films. *Acs Macro Lett* **2014,** *3* (10), 1029-1035.

24. Kongkanand, A., Interfacial Water Transport Measurements in Nafion Thin Films Using a Quartz-Crystal Microbalance. *J Phys Chem C* **2011,** *115* (22), 11318-11325.

25. Singh, R. K.; Devivaraprasad, R.; Kar, T.; Chakraborty, A.; Neergat, M., Electrochemical Impedance Spectroscopy of Oxygen Reduction Reaction (Orr) in a Rotating Disk Electrode Configuration: Effect of Ionomer Content and Carbon-Support. *J Electrochem Soc* **2015,** *162* (6), F489-F498.

26. Shinozaki, K.; Zack, J. W.; Pylypenko, S.; Pivovar, B. S.; Kocha, S. S., Oxygen Reduction Reaction Measurements on Platinum Electrocatalysts Utilizing Rotating Disk Electrode Technique Ii. Influence of Ink Formulation, Catalyst Layer Uniformity and Thickness. *J Electrochem Soc* **2015,** *162* (12), F1384-F1396.

27. Kudo, K.; Jinnouchi, R.; Morimoto, Y., Humidity and Temperature Dependences of Oxygen Transport Resistance of Nafion Thin Film on Platinum Electrode. *Electrochim Acta* **2016,** *209*, 682-690.

28. Ono, Y.; Nagao, Y., Interfacial Structure and Proton Conductivity of Nafion at the Pt-Deposited Surface. *Langmuir* **2016,** *32* (1), 352-358.

29. Zhang, X. Y.; Ding, Y. H., Thickness-Dependent Structural and Transport Behaviors in the Platinum-Nafion Interface: A Molecular Dynamics Investigation. *Rsc Adv* **2014,** *4* (83), 44214-44222.

30. Lin, R. B.; Shih, S. M., Effects of Mass Transfer on Kinetics of Hydrogen Oxidation Reaction at Nafion/Pt-Black Thin-Film Electrodes. *J Taiwan Inst Chem E* **2013,** *44* (3), 393-401.

31. Lin, R.-B.; Shih, S.-M., Kinetics of Hydrogen Oxidation Reaction on Nafion-Coated Pt/C Electrodes under High Overpotentials. *Journal of the Chinese Institute of Chemical Engineers* **2007,** *38* (5), 365-370.

32. Sambandam, S.; Parrondo, J.; Ramani, V., Estimation of Electrode Ionomer Oxygen Permeability and Ionomer-Phase Oxygen Transport Resistance in Polymer Electrolyte Fuel Cells. *Phys Chem Chem Phys* **2013,** *15* (36), 14994-15002.

33. Malevich, D.; Halliop, E.; Peppley, B. A.; Pharoah, J. G.; Karan, K., Investigation of Charge-Transfer and Mass-Transport Resistances in Pemfcs with Microporous Layer Using Electrochemical Impedance Spectroscopy. *J Electrochem Soc* **2009,** *156* (2), B216-B224.

34. Jinnouchi, R.; Kudo, K.; Kitano, N.; Morimoto, Y., Molecular Dynamics Simulations on O 2 Permeation through Nafion Ionomer on Platinum Surface. *Electrochim Acta* **2016,** *188*, 767-776.

35. Moore, M.; Wardlaw, P.; Dobson, P.; Boisvert, J. J.; Putz, A.; Spiteri, R. J.; Secanell, M., Understanding the Effect of Kinetic and Mass Transport Processes in Cathode Agglomerates. *J Electrochem Soc* **2014,** *161* (8), E3125-E3137.

36. Weber, A. Z.; Kusoglu, A., Unexplained Transport Resistances for Low-Loaded Fuel-Cell Catalyst Layers. *J Mater Chem A* **2014,** *2* (41), 17207-17211.

37. Hickner, M. A.; Ghassemi, H.; Kim, Y. S.; Einsla, B. R.; McGrath, J. E., Alternative Polymer Systems for Proton Exchange Membranes (Pems). *Chem Rev* **2004,** *104* (10), 4587-4611.

38. Smitha, B.; Sridhar, S.; Khan, A. A., Solid Polymer Electrolyte Membranes for Fuel Cell Applications - a Review. *J Membrane Sci* **2005,** *259* (1-2), 10-26.

39. Sone, Y.; Ekdunge, P.; Simonsson, D., Proton Conductivity of Nafion 117 as Measured by a Four-Electrode Ac Impedance Method. *J Electrochem Soc* **1996,** *143* (4), 1254-1259.

40. Anantaraman, A.; Gardner, C., Studies on Ion-Exchange Membranes. Part 1. Effect of Humidity on the Conductivity of Nafion®. *Journal of Electroanalytical Chemistry* **1996,** *414* (2), 115-120.

41. Paddison, S. J.; Paul, R., The Nature of Proton Transport in Fully Hydrated Nafion (R). *Phys Chem Chem Phys* **2002,** *4* (7), 1158-1163.

42. Bernard, L.; Fitch, A.; Wright, A. F.; Fender, B. E. F.; Howe, A. T., Mechanisms of Hydrogen Diffusion and Conduction in Duo2aso4.4d2o as Inferred from Neutron-Diffraction Evidence. *Solid State Ionics* **1981,** *5* (Oct), 459-462.

43. Kreuer, K. D.; Rabenau, A.; Weppner, W., Vehicle Mechanism, a New Model for the Interpretation of the Conductivity of Fast Proton Conductors. *Angew Chem Int Edit* **1982,** *21* (3), 208-209.

44. Cooper, K. R., Characterizing through-Plane and in-Plane Ionic Conductivity of Polymer Electrolyte Membranes. *Polymer Electrolyte Fuel Cells 11* **2011,** *41* (1), 1371-1380.

45. Jiang, R.; Mittelsteadt, C. K.; Gittleman, C. S., Through-Plane Proton Transport Resistance of Membrane and Ohmic Resistance Distribution in Fuel Cells. *J Electrochem Soc* **2009,** *156* (12), B1440-B1446.

46. Alberti, G.; Casciola, M.; Massinelli, L.; Bauer, B., Polymeric Proton Conducting Membranes for Medium Temperature Fuel Cells (110-160 Degrees C). *J Membrane Sci* **2001,** *185* (1), 73-81.

47. Abe, T.; Shima, H.; Watanabe, K.; Ito, Y., Study of Pefcs by Ac Impedance, Current Interrupt, and Dew Point Measurements - I. Effect of Humidity in Oxygen Gas. *J Electrochem Soc* **2004,** *151* (1), A101-A105.

48. Marsh, G., Membranes Fit for a Revolution. *Materials Today* **2003,** *6* (3), 38-43.

49. Peighambardoust, S. J.; Rowshanzamir, S.; Amjadi, M., Review of the Proton Exchange Membranes for Fuel Cell Applications. *International Journal of Hydrogen Energy* **2010,** *35* (17), 9349-9384.

50. Sengul, E.; Erdener, H.; Akay, R. G.; Yucel, H.; Bac, N.; Eroglu, I., Effects of Sulfonated Polyether-Etherketone (Speek) and Composite Membranes on the Proton Exchange Membrane Fuel Cell (Pemfc) Performance. *International Journal of Hydrogen Energy* **2009,** *34* (10), 4645-4652.

51. Jiang, R. C.; Kunz, H. R.; Fenton, J. M., Investigation of Membrane Property and Fuel Cell Behavior with Sulfonated Poly(Ether Ether Ketone) Electrolyte: Temperature and Relative Humidity Effects. *J Power Sources* **2005,** *150*, 120-128.

52. Nguyen, M. D. T.; Yang, S.; Kim, D., Pendant Dual Sulfonated Poly(Arylene Ether Ketone) Proton Exchange Membranes for Fuel Cell Application. *J Power Sources* **2016,** *328*, 355-363.

53. Parnian, M. J.; Rowshanzamir, S.; Gashoul, F., Comprehensive Investigation of Physicochemical and Electrochemical Properties of Sulfonated Poly (Ether Ether Ketone) Membranes with Different Degrees of Sulfonation for Proton Exchange Membrane Fuel Cell Applications. *Energy* **2017,** *125*, 614-628.

54. Kobayashi, T.; Rikukawa, M.; Sanui, K.; Ogata, N., Proton-Conducting Polymers Derived from Poly(Ether-Etherketone) and Poly(4-Phenoxybenzoyl-1,4-Phenylene). *Solid State Ionics* **1998,** *106* (3-4), 219-225.

55. Noshay, A.; Robeson, L. M., Sulfonated Polysulfone. *J Appl Polym Sci* **1976,** *20* (7), 1885-1903.

56. Lee, J. K.; Li, W.; Manthiram, A., Poly(Arylene Ether Sulfone)S Containing Pendant Sulfonic Acid Groups as Membrane Materials for Direct Methanol Fuel Cells. *J Membrane Sci* **2009,** *330* (1-2), 73-79.

57. Wang, F.; Hickner, M.; Ji, Q.; Harrison, W.; Mecham, J.; Zawodzinski, T. A.; McGrath, J. E., Synthesis of Highly Sulfonated Poly(Arylene Ether Sulfone) Random (Statistical) Copolymers Via Direct Polymerization. *Macromol Symp* **2001,** *175*, 387-395.

58. Lee, S. W.; Chen, J. C.; Wu, J. A.; Chen, K. H., Synthesis and Properties of Poly(Ether Sulfone)S with Clustered Sulfonic Groups for Pemfc Applications under Various Relative Humidity. *Acs Appl Mater Inter* **2017,** *9* (11), 9805-9814.

59. Dai, H.; Zhang, H. M.; Luo, Q. T.; Zhang, Y.; Bi, C., Properties and Fuel Cell Performance of Proton Exchange Membranes Prepared from Disulfonated Poly(Sulfide Sulfone). *J Power Sources* **2008,** *185* (1), 19-25.

60. Miyake, J.; Taki, R.; Mochizuki, T.; Shimizu, R.; Akiyama, R.; Uchida, M.; Miyatake, K., Design of Flexible Polyphenylene Proton-Conducting Membrane for Next-Generation Fuel Cells. *Sci Adv* **2017,** *3* (10).

61. Wang, X. H.; Richey, F. W.; Wujcik, K. H.; Elabd, Y. A., Ultra-Low Platinum Loadings in Polymer Electrolyte Membrane Fuel Cell Electrodes Fabricated Via Simultaneous Electrospinning/Electrospraying Method. *J Power Sources* **2014,** *264*, 42-48.

62. Oh, K.; Ketpang, K.; Kim, H.; Shanmugam, S., Synthesis of Sulfonated Poly(Arylene Ether Ketone) Block Copolymers for Proton Exchange Membrane Fuel Cells. *J Membrane Sci* **2016,** *507*, 135-142.

63. Yoon, K. S.; Lee, J. Y.; Kim, T. H.; Yu, D. M.; Hong, S. K.; Hong, Y. T., Multiblock Copolymers Based on Poly(P-Phenylene)-Co-Poly(Arylene Ether Sulfone Ketone) with Sulfonated Multiphenyl Pendant Groups for Polymer Electrolyte Fuel Cell (Pemfc) Application. *Eur Polym J* **2015,** *66*, 1-11.

64. Kim, K.; Jung, B. K.; Ko, T.; Kim, T. H.; Lee, J. C., Comb-Shaped Polysulfones Containing Sulfonated Polytriazole Side Chains for Proton Exchange Membranes. *J Membrane Sci* **2018,** *554*, 232-243.

65. Lin, B. Y. S.; Kirk, D. W.; Thorpe, S. J., Performance of Alkaline Fuel Cells: A Possible Future Energy System? *J Power Sources* **2006,** *161* (1), 474-483.

66. Merle, G.; Wessling, M.; Nijmeijer, K., Anion Exchange Membranes for Alkaline Fuel Cells: A Review. *J Membrane Sci* **2011,** *377* (1-2), 1-35.

67. Varcoe, J. R.; Slade, R. C. T., An Electron-Beam-Grafted Etfe Alkaline Anion-Exchange Membrane in Metal-Cation-Free Solid-State Alkaline Fuel Cells. *Electrochem Commun* **2006,** *8* (5), 839-843.

68. Mamlouk, M.; Horsfall, J. A.; Williams, C.; Scott, K., Radiation Grafted Membranes for Superior Anion Exchange Polymer Membrane Fuel Cells Performance. *International Journal of Hydrogen Energy* **2012,** *37* (16), 11912-11920.

69. Yoshimura, K.; Koshikawa, H.; Yamaki, T.; Shishitani, H.; Yamamoto, K.; Yamaguchi, S.; Tanaka, H.; Maekawa, Y., Imidazolium Cation Based Anion-Conducting Electrolyte Membranes Prepared by Radiation Induced Grafting for Direct Hydrazine Hydrate Fuel Cells. *J Electrochem Soc* **2014,** *161* (9), F889-F893.

70. Nykaza, J. R.; Benjamin, R.; Meek, K. M.; Elabd, Y. A., Polymerized Ionic Liquid Diblock Copolymer as an Ionomer and Anion Exchange Membrane for Alkaline Fuel Cells. *Chem Eng Sci* **2016,** *154*, 119-127.

71. Zhao, C. J.; Ma, W. J.; Sun, W. M.; Na, H., Preparation of Anion Exchange Membrane Based on Homogeneous Quaternization of Bromomethylated Poly(Arylene Ether Sulfone). *J Appl Polym Sci* **2014,** *131* (10).

72. Gopi, K. H.; Peera, S. G.; Bhat, S. D.; Sridhar, P.; Pitchumani, S., Preparation and Characterization of Quaternary Ammonium Functionalized Poly(2,6-Dimethyl-1,4-Phenylene Oxide) as Anion Exchange Membrane for Alkaline Polymer Electrolyte Fuel Cells. *International Journal of Hydrogen Energy* **2014,** *39* (6), 2659-2668.

73. Hibbs, M. R.; Fujimoto, C. H.; Cornelius, C. J., Synthesis and Characterization of Poly(Phenylene)-Based Anion Exchange Membranes for Alkaline Fuel Cells. *Macromolecules* **2009,** *42* (21), 8316-8321.

74. Li, N. W.; Leng, Y. J.; Hickner, M. A.; Wang, C. Y., Highly Stable, Anion Conductive, Comb-Shaped Copolymers for Alkaline Fuel Cells. *J Am Chem Soc* **2013,** *135* (27), 10124-10133.

75. Jiang, L. H.; Lin, X. C.; Ran, J.; Li, C. R.; Wu, L.; Xu, T. W., Synthesis and Properties of Quaternary Phosphonium-Based Anion Exchange Membrane for Fuel Cells. *Chinese J Chem* **2012,** *30* (9), 2241-2246.

76. Hamada, T.; Yoshimura, K.; Hiroki, A.; Maekawa, Y., Synthesis and Characterization of Aniline-Containing Anion-Conducting Polymer Electrolyte Membranes by Radiation-Induced Graft Polymerization. *J Appl Polym Sci* **2018,** *135* (48).

77. Noonan, K. J. T.; Hugar, K. M.; Kostalik, H. A.; Lobkovsky, E. B.; Abruna, H. D.; Coates, G. W., Phosphonium-Functionalized Polyethylene: A New Class of Base-Stable Alkaline Anion Exchange Membranes. *J Am Chem Soc* **2012,** *134* (44), 18161-18164.

78. Arges, C. G.; Kulkarni, S.; Baranek, A.; Pan, K.-J.; Jung, M.-S.; Patton, D.; Mauritz, K. A.; Ramani, V., Quarternary Ammonium and Phosphonium Based Anion Exchange Membranes for Alkaline Fuel Cells. *Ecs Transactions* **2010,** *33* (1), 1903-1913.

79. Ye, Y. S.; Stokes, K. K.; Beyer, F. L.; Elabd, Y. A., Development of Phosphonium-Based Bicarbonate Anion Exchange Polymer Membranes. *J Membrane Sci* **2013,** *443*, 93-99.

80. Jangu, C.; Long, T. E., Phosphonium Cation-Containing Polymers: From Ionic Liquids to Polyelectrolytes. *Polymer* **2014,** *55* (16), 3298-3304.

81. He, Y. B.; Wu, L.; Pan, J. F.; Zhu, Y.; Ge, X. L.; Yang, Z. J.; Ran, J.; Xu, T. W., A Mechanically Robust Anion Exchange Membrane with High Hydroxide Conductivity. *J Membrane Sci* **2016,** *504*, 47-54.

82. Fujimoto, C.; Kim, D. S.; Hibbs, M.; Wrobleski, D.; Kim, Y. S., Backbone Stability of Quaternized Polyaromatics for Alkaline Membrane Fuel Cells. *J Membrane Sci* **2012,** *423*, 438-449.

83. Wang, L. Q.; Brink, J. J.; Liu, Y.; Herring, A. M.; Ponce-Gonzalez, J.; Whelligan, D. K.; Varcoe, J. R., Non-Fluorinated Pre-Irradiation-Grafted (Peroxidated) Ldpe-Based Anion-Exchange Membranes with High Performance and Stability. *Energ Environ Sci* **2017,** *10* (10), 2154-2167.

84. Meek, K. M.; Elabd, Y. A., Alkaline Chemical Stability of Polymerized Ionic Liquids with Various Cations. *Macromolecules* **2015,** *48* (19), 7071-7084.

85. Dekel, D. R., Review of Cell Performance in Anion Exchange Membrane Fuel Cells. *J Power Sources* **2018,** *375*, 158-169.

86. Lu, W. T.; Shao, Z. G.; Zhang, G.; Zhao, Y.; Yi, B. L., Cross Linked Poly(Vinylbenzyl Chloride) with a Macromolecular Crosslinker for Anion Exchange Membrane Fuel Cells. *J Power Sources* **2014,** *248*, 905-914.

87. Luo, Y. T.; Guo, J. C.; Wang, C. S.; Chu, D., Tunable High-Molecular-Weight Anion-Exchange Membranes for Alkaline Fuel Cells. *Macromol Chem Phys* **2011,** *212* (19), 2094-2102.

88. Biancolli, A. L. G.; Herranz, D.; Wang, L. Q.; Stehlikova, G.; Bance-Soualhi, R.; Ponce-Gonzalez, J.; Ocon, P.; Ticianelli, E. A.; Whelligan, D. K.; Varcoe, J. R.; Santiago, E. I., Etfe-Based Anion-Exchange Membrane Ionomer Powders for Alkaline Membrane Fuel Cells: A First

Performance Comparison of Head-Group Chemistry. *J Mater Chem A* **2018,** *6* (47), 24330-24341.

89. Zeng, L.; Zhao, T. S.; An, L., A High-Performance Supportless Silver Nanowire Catalyst for Anion Exchange Membrane Fuel Cells. *J Mater Chem A* **2015,** *3* (4), 1410-1416.

90. Lu, W. T.; Zhang, G.; Li, J.; Hao, J. K.; Wei, F.; Li, W. H.; Zhang, J. Y.; Shao, Z. G.; Yi, B. L., Polybenzimidazole-Crosslinked Poly(Vinylbenzyl Chloride) with Quaternary 1,4-Diazabicyclo (2.2.2) Octane Groups as High-Performance Anion Exchange Membrane for Fuel Cells. *J Power Sources* **2015,** *296*, 204-214.

91. Peng, H. G.; Li, Q. H.; Hu, M. X.; Xiao, L.; Lu, J. T.; Zhuang, L., Alkaline Polymer Electrolyte Fuel Cells Stably Working at 80 Degrees C. *J Power Sources* **2018,** *390*, 165-167.

92. Lin, X. C.; Liu, Y. B.; Poynton, S. D.; Ong, A. L.; Varcoe, J. R.; Wu, L.; Li, Y.; Liang, X. H.; Li, Q. H.; Xu, T. W., Cross-Linked Anion Exchange Membranes for Alkaline Fuel Cells Synthesized Using a Solvent Free Strategy. *J Power Sources* **2013,** *233*, 259-268.

93. Zhao, Y.; Yu, H. M.; Yang, D. L.; Li, J.; Shao, Z. G.; Yi, B. L., High-Performance Alkaline Fuel Cells Using Crosslinked Composite Anion Exchange Membrane. *J Power Sources* **2013,** *221*, 247-251.

94. Piana, M.; Boccia, M.; Filpi, A.; Flammia, E.; Miller, H. A.; Orsini, M.; Salusti, F.; Santiccioli, S.; Ciardelli, F.; Pucci, A., H2/Air Alkaline Membrane Fuel Cell Performance and Durability, Using Novel Ionomer and Non-Platinum Group Metal Cathode Catalyst. *J Power Sources* **2010,** *195* (18), 5875-5881.

95. Leng, Y. J.; Wang, L. Z.; Hickner, M. A.; Wang, C. Y., Alkaline Membrane Fuel Cells with in-Situ Cross-Linked Ionomers. *Electrochim Acta* **2015,** *152*, 93-100.

96. Gao, X. Q.; Yu, H. M.; Jia, J.; Hao, J. K.; Xie, F.; Chi, J.; Qin, B. W.; Fu, L.; Song, W.; Shao, Z. G., High Performance Anion Exchange Ionomer for Anion Exchange Membrane Fuel Cells. *Rsc Adv* **2017,** *7* (31), 19153-19161.

97. De Bruijn, F.; Dam, V.; Janssen, G., Durability and Degradation Issues of Pem Fuel Cell Components. *Fuel cells* **2008,** *8* (1), 3-22.

98. Owejan, J. P.; Owejan, J. E.; Gu, W. B., Impact of Platinum Loading and Catalyst Layer Structure on Pemfc Performance. *J Electrochem Soc* **2013,** *160* (8), F824-F833.

99. Greszler, T. A.; Caulk, D.; Sinha, P., The Impact of Platinum Loading on Oxygen Transport Resistance. *J Electrochem Soc* **2012,** *159* (12), F831-F840.

100. Egetenmeyer, A.; Radev, I.; Durneata, D.; Baumgartner, M.; Peinecke, V.; Natter, H.; Hempelmann, R., Pulse Electrodeposited Cathode Catalyst Layers for Pem Fuel Cells. *International Journal of Hydrogen Energy* **2017,** *42* (19), 13649-13660.

101. Fofana, D.; Natarajan, S. K.; Bénard, P.; Hamelin, J., High Performance Pem Fuel Cell with Low Platinum Loading at the Cathode Using Magnetron Sputter Deposition. *ISRN Electrochemistry* **2012,** *2013*.

102. Martin, S.; Martinez-Vazquez, B.; Garcia-Ybarra, P. L.; Castillo, J. L., Peak Utilization of Catalyst with Ultra-Low Pt Loaded Pem Fuel Cell Electrodes Prepared by the Electrospray Method. *J Power Sources* **2013,** *229*, 179-184.

103. Oh, J. W.; Na, H.; Nahm, S.; Kim, Y.; Choi, H., Multi-Layered Membrane Electrode Assembly Fabrication by Electro-Spraying. *Ecs Transactions* **2013,** *58* (1), 1075-1083.

104. Brodt, M.; Han, T.; Dale, N.; Niangar, E.; Wycisk, R.; Pintauro, P., Fabrication, in-Situ Performance, and Durability of Nanofiber Fuel Cell Electrodes. *J Electrochem Soc* **2015,** *162* (1), F84-F91.

105. Brodt, M.; Wycisk, R.; Pintauro, P.; Han, T.; Dale, N.; Adjemian, K., Nanofiber Fuel Cell Electrodes I. Fabrication and Performance with Commercial Pt/C Catalysts. *Ecs Transactions* **2013,** *58* (1), 381-390.

106. Si, D.; Zhang, S.; Huang, J.; Wang, C.; Liu, Y.; Zhang, J., Electrochemical Characterization of Pre-Conditioning Process of Electrospun Nanofiber Electrodes in Polymer Electrolyte Fuel Cells. *Fuel Cells* **2018,** *18* (5), 576-585.

107. Hwang, D. S.; Park, C. H.; Yi, S. C.; Lee, Y. M., Optimal Catalyst Layer Structure of Polymer Electrolyte Membrane Fuel Cell. *International Journal of Hydrogen Energy* **2011,** *36* (16), 9876-9885.

108. Shukla, S.; Domican, K.; Karan, K.; Bhattacharjee, S.; Secanell, M., Analysis of Low Platinum Loading Thin Polymer Electrolyte Fuel Cell Electrodes Prepared by Inkjet Printing. *Electrochim Acta* **2015,** *156*, 289-300.

109. Wang, X. H.; Richey, F. W.; Wujcik, K. H.; Ventura, R.; Mattson, K.; Elabd, Y. A., Effect of Polytetrafluoroethylene on Ultra-Low Platinum Loaded Electrospun/Electrosprayed Electrodes in Proton Exchange Membrane Fuel Cells. *Electrochim Acta* **2014,** *139*, 217-224.

110. Bett, J.; Kinoshita, K.; Routsis, K.; Stonehart, P., A Comparison of Gas-Phase and Electrochemical Measurements for Chemisorbed Carbon Monoxide and Hydrogen on Platinum Crystallites. *Journal of Catalysis* **1973,** *29* (1), 160-168.

111. Paasch, G.; Micka, K.; Gersdorf, P., Theory of the Electrochemical Impedance of Macrohomogeneous Porous Electrodes. *Electrochimica Acta* **1993,** *38* (18), 2653-2662.

112. Sudoh, M.; Kondoh, T.; Kamiya, N.; Ueda, T.; Okajima, K., Impedance Analysis of Gas-Diffusion Electrode Coated with a Thin Layer of Fluoro Ionomer to Enhance Its Stability in Oxygen Reduction. *J Electrochem Soc* **2000,** *147* (10), 3739-3744.

113. Paul, D. K.; McCreery, R.; Karan, K., Proton Transport Property in Supported Nafion Nanothin Films by Electrochemical Impedance Spectroscopy. *J Electrochem Soc* **2014,** *161* (14), F1395-F1402.

114. Springer, T. E.; Zawodzinski, T. A.; Wilson, M. S.; Gottesfeld, S., Characterization of Polymer Electrolyte Fuel Cells Using Ac Impedance Spectroscopy. *J Electrochem Soc* **1996,** *143* (2), 587-599.

115. Eikerling, M.; Kornyshev, A. A., Electrochemical Impedance of the Cathode Catalyst Layer in Polymer Electrolyte Fuel Cells. *J Electroanal Chem* **1999,** *475* (2), 107-123.

116. Ciureanu, M.; Roberge, R., Electrochemical Impedance Study of Pem Fuel Cells. Experimental Diagnostics and Modeling of Air Cathodes. *J Phys Chem B* **2001,** *105* (17), 3531-3539.

117. Guo, Q. Z.; Cayetano, M.; Tsou, Y. M.; De Castro, E. S.; White, R. E., Study of Ionic Conductivity Profiles of the Air Cathode of a Pemfc by Ac Impedance Spectroscopy. *J Electrochem Soc* **2003,** *150* (11), A1440-A1449.

118. Saab, A. P.; Garzon, F. H.; Zawodzinski, T. A., Determination of Ionic and Electronic Resistivities in Carbon/Polyelectrolyte Fuel-Cell Composite Electrodes. *J Electrochem Soc* **2002,** *149* (12), A1541-A1546.

119. Lefebvre, M. C.; Martin, R. B.; Pickup, P. G., Characterization of Ionic Conductivity Profiles within Proton Exchange Membrane Fuel Cell Gas Diffusion Electrodes by Impedance Spectroscopy. *Electrochemical and solid-state letters* **1999,** *2* (6), 259-261.

120. Makharia, R.; Mathias, M. F.; Baker, D. R., Measurement of Catalyst Layer Electrolyte Resistance in Pefcs Using Electrochemical Impedance Spectroscopy. *J Electrochem Soc* **2005,** *152* (5), A970-A977.

121. Thepkaew, J.; Therdthianwong, A.; Therdthianwong, S., Key Parameters of Active Layers Affecting Proton Exchange Membrane (Pem) Fuel Cell Performance. *Energy* **2008,** *33* (12), 1794-1800.

122. Qi, Z. G.; Kaufman, A., Low Pt Loading High Performance Cathodes for Pem Fuel Cells. *J Power Sources* **2003,** *113* (1), 37-43.

123. Sasikumar, G.; Ihm, J. W.; Ryu, H., Dependence of Optimum Nafion Content in Catalyst Layer on Platinum Loading. *J Power Sources* **2004,** *132* (1-2), 11-17.

124. Wang, X.; Richey, F. W.; Wujcik, K. H.; Elabd, Y. A., Ultra-Low Platinum Loadings in Polymer Electrolyte Membrane Fuel Cell Electrodes Fabricated Via Simultaneous Electrospinning/Electrospraying Method. *J Power Sources* **2014,** *264*, 42-48.

125. Wang, X.; Richey, F. W.; Wujcik, K. H.; Ventura, R.; Mattson, K.; Elabd, Y. A., Effect of Polytetrafluoroethylene on Ultra-Low Platinum Loaded Electrospun/Electrosprayed Electrodes in Proton Exchange Membrane Fuel Cells. *Electrochimica Acta* **2014,** *139*, 217-224.

126. Brodt, M.; Wycisk, R.; Dale, N.; Pintauro, P., Power Output and Durability of Electrospun Fuel Cell Fiber Cathodes with Pvdf and Nafion/Pvdf Binders. *J Electrochem Soc* **2016,** *163* (5), F401-F410.

127. Brodt, M.; Wycisk, R.; Pintauro, P. N., Nanofiber Electrodes with Low Platinum Loading for High Power Hydrogen/Air Pem Fuel Cells. *J Electrochem Soc* **2013,** *160* (8), F744-F749.

128. Ballengee, J. B.; Pintauro, P. N., Preparation of Nanofiber Composite Proton-Exchange Membranes from Dual Fiber Electrospun Mats. *J Membrane Sci* **2013,** *442*, 187-195.

129. Lee, K. M.; Choi, J.; Wycisk, R.; Pintauro, P. N.; Mather, P. T., Nafion Nanofiber Membranes. *Proton Exchange Membrane Fuel Cells 9* **2009,** *25* (1), 1451-1458.

130. Hasani-Sadrabadi, M. M.; Shabani, I.; Soleimani, M.; Moaddel, H., Novel Nanofiber-Based Triple-Layer Proton Exchange Membranes for Fuel Cell Applications. *J Power Sources* **2011,** *196* (10), 4599-4603.

131. Shabani, I.; Hasani-Sadrabadi, M. M.; Haddadi-Asl, V.; Soleimani, M., Nanofiber-Based Polyelectrolytes as Novel Membranes for Fuel Cell Applications. *J Membrane Sci* **2011,** *368* (1-2), 233-240.

132. Laforgue, A.; Robitaille, L.; Mokrini, A.; Ajji, A., Fabrication and Characterization of Ionic Conducting Nanofibers. *Macromol Mater Eng* **2007,** *292* (12), 1229-1236.

133. Ballengee, J. B.; Pintauro, P. N., Composite Fuel Cell Membranes from Dual-Nanofiber Electrospun Mats. *Macromolecules* **2011,** *44* (18), 7307-7314.

134. Simotwo, S.; Kalra, V., Dual Nafion/Polyaniline Nanofibers Architecture for Applications in Fuel Cells Electrodes. *Ecs Transactions* **2015,** *69* (17), 943-953.

135. Park, J. W.; Wycisk, R.; Pintauro, P. N.; Yarlagadda, V.; Nguyen, T. V., Electrospun Nafion (R)/Polyphenylsulfone Composite Membranes for Regenerative Hydrogen Bromine Fuel Cells. *Materials* **2016,** *9* (3).

136. Tran, C.; Kalra, V., Fabrication of Porous Carbon Nanofibers with Adjustable Pore Sizes as Electrodes for Supercapacitors. *J Power Sources* **2013,** *235*, 289-296.

137. Sheng, L.; Dajing, C.; Yuquan, C., A Surface Acoustic Wave Humidity Sensor with High Sensitivity Based on Electrospun Mwcnt/Nafion Nanofiber Films. *Nanotechnology* **2011,** *22* (26), 265504.

138. Okafor, C.; Maaza, M.; Mokrani, T., Nafion Nanofiber Composite Membrane Fabrication for Fuel Cell Applications. *Int J Chem Nucl Mater Metall Eng* **2014,** *8*, 389-392.

139. Lee, J.-W.; Yoo, Y.-T., Preparation and Performance of Ipmc Actuators with Electrospun Nafion®–Mwnt Composite Electrodes. *Sensors and Actuators B: Chemical* **2011,** *159* (1), 103-111.

140. Dong, B.; Gwee, L.; Salas-de la Cruz, D.; Winey, K. I.; Elabd, Y. A., Super Proton Conductive High-Purity Nafion Nanofibers. *Nano Lett* **2010,** *10* (9), 3785-3790.

141. Zhang, F.; Zhang, Z.; Liu, Y.; Leng, J., Shape Memory Properties of Electrospun Nafion Nanofibers. *Fibers and Polymers* **2014,** *15* (3), 534-539.

142. Zhang, F.; Zhang, Z.; Liu, Y.; Lu, H.; Leng, J., The Quintuple-Shape Memory Effect in Electrospun Nanofiber Membranes. *Smart Mater Struct* **2013,** *22* (8), 085020.

143. Snyder, J. D.; Elabd, Y. A., Nafion (R) Nanofibers and Their Effect on Polymer Electrolyte Membrane Fuel Cell Performance. *J Power Sources* **2009,** *186* (2), 385-392.

144. Bajon, R.; Balaji, S.; Guo, S. M., Electrospun Nafion Nanofiber for Proton Exchange Membrane Fuel Cell Application. *J Fuel Cell Sci Tech* **2009,** *6* (3).

145. Zhang, W. J.; Pintauro, P. N., High-Performance Nanofiber Fuel Cell Electrodes. *Chemsuschem* **2011,** *4* (12), 1753-1757.

146. Pan, C.; Wu, H.; Wang, C.; Wang, B.; Zhang, L.; Cheng, Z.; Hu, P.; Pan, W.; Zhou, Z.; Yang, X., Nanowire-Based High-Performance "Micro Fuel Cells": One Nanowire, One Fuel Cell. *Advanced Materials* **2008,** *20* (9), 1644-1648.

147. Park, J. W.; Wycisk, R.; Lin, G. Y.; Chong, P. Y.; Powers, D.; Van Nguyen, T.; Dowd, R. P.; Pintauro, P. N., Electrospun Nafion/Pvdf Single-Fiber Blended Membranes for Regenerative H-2/Br-2 Fuel Cells. *J Membrane Sci* **2017,** *541*, 85-92.

148. Ballengee, J. B.; Pintauro, P. N., Morphological Control of Electrospun Nafion Nanofiber Mats. *J Electrochem Soc* **2011,** *158* (5), B568-B572.

149. Song, T. D.; Chen, Z. Y.; He, H.; Liu, Y. X.; Liu, Y.; Ramakrishna, S., Orthogonal Design Study on Factors Affecting the Diameter of Perfluorinated Sulfonic Acid Nanofibers During Electrospinning. *J Appl Polym Sci* **2015,** *132* (14).

150. Chen, H.; Snyder, J. D.; Elabd, Y. A., Electrospinning and Solution Properties of Nafion and Poly(Acrylic Acid). *Macromolecules* **2008,** *41* (1), 128-135.

151. Welch, C.; Labouriau, A.; Hjelm, R.; Orler, B.; Johnston, C.; Kim, Y. S., Nafion in Dilute Solvent Systems: Dispersion or Solution? *Acs Macro Lett* **2012,** *1* (12), 1403-1407.

152. Varabhas, J. S.; Chase, G. G.; Reneker, D. H., Electrospun Nanofibers from a Porous Hollow Tube. *Polymer* **2008,** *49* (19), 4226-4229.

153. Salem, D., Electrospinning of Nanofibers and the Charge Injection Method. In *Nanofibers and Nanotechnology in Textiles*, Elsevier: 2007; pp 3-21.

154. Yarin, A. L.; Zussman, E., Upward Needleless Electrospinning of Multiple Nanofibers. *Polymer* **2004,** *45* (9), 2977-2980.

155. Liu, Y.; He, J. H.; Yu, J. Y., Bubble-Electrospinning: A Novel Method for Making Nanofibers. *J Phys Conf Ser* **2008,** *96*.

156. Yang, R. R.; He, J. H.; Xu, L.; Yu, J. Y., Bubble-Electrospinning for Fabricating Nanofibers. *Polymer* **2009,** *50* (24), 5846-5850.

157. Dosunmu, O. O.; Chase, G. G.; Kataphinan, W.; Reneker, D. H., Electrospinning of Polymer Nanofibres from Multiple Jets on a Porous Tubular Surface. *Nanotechnology* **2006,** *17* (4), 1123-1127.

158. Higham, A. K.; Tang, C.; Landry, A. M.; Pridgeon, M. C.; Lee, E. M.; Andrady, A. L.; Khan, S. A., Foam Electrospinning: A Multiple Jet, Needle-Less Process for Nanofiber Production. *Aiche J* **2014,** *60* (4), 1355-1364.

159. McKee, M. G.; Hunley, M. T.; Layman, J. M.; Long, T. E., Solution Rheological Behavior and Electrospinning of Cationic Polyelectrolytes. *Macromolecules* **2006,** *39* (2), 575-583.

160. Chen, L.; Hallinan, D. T.; Elabd, Y. A.; Hillmyer, M. A., Highly Selective Polymer Electrolyte Membranes from Reactive Block Polymers. *Macromolecules* **2009,** *42* (16), 6075-6085.

161. El-hadi, A. M.; Al-Jabri, F. Y., Influence of Electrospinning Parameters on Fiber Diameter and Mechanical Properties of Poly(3-Hydroxybutyrate) (Phb) and Polyanilines (Pani) Blends. *Polymers-Basel* **2016,** *8* (3).

162. Elabd, Y. A.; Hickner, M. A., Block Copolymers for Fuel Cells. *Macromolecules* **2011,** *44* (1), 1-11.

163. Griffin, P. J.; Salmon, G. B.; Ford, J.; Winey, K. I., Predicting the Solution Morphology of a Sulfonated Pentablock Copolymer in Binary Solvent Mixtures. *J Polym Sci Pol Phys* **2016,** *54* (2), 254-262.

164. Choi, J. H.; Kota, A.; Winey, K. I., Micellar Morphology in Sulfonated Pentablock Copolymer Solutions. *Ind Eng Chem Res* **2010,** *49* (23), 12093-12097.

165. Wang, D. H.; Fan, Y. F.; Zhang, M. Q.; Moore, R. B.; Cornelius, C. J., Ionomer Solution to Film Solidification Dependence Upon Solvent Type and Its Impact Upon Morphology and Ion Transport. *Eur Polym J* **2017,** *97*, 169-177.

166. Fan, Y. F.; Zhang, M. Q.; Moore, R. B.; Cornelius, C. J., Structure, Physical Properties, and Molecule Transport of Gas, Liquid, and Ions within a Pentablock Copolymer. *J Membrane Sci* **2014,** *464*, 179-187.

167. Choi, J. H.; Willis, C. L.; Winey, K. I., Structure-Property Relationship in Sulfonated Pentablock Copolymers. *J Membrane Sci* **2012,** *394*, 169-174.

168. Truong, P. V.; Shingleton, S.; Kummoun, M.; Black, R. L.; Charendoff, M.; Willis, C.; Ardebili, H.; Stein, G. E., Structure and Properties of Sulfonated Pentablock Terpolymer Films as a Function of Wet-Dry Cycles. *Macromolecules* **2018,** *51* (6), 2203-2215.

169. Zheng, W.; Cornelius, C. J., Solvent Tunable Multi-Block Ionomer Morphology and Its Relationship to Modulus, Water Swelling, Directionally Dependent Ion Transport, and Actuator Performance. *Polymer* **2016,** *103*, 104-111.

170. Akhtar, F. H.; Vovushua, H.; Villalobos, L. F.; Shevate, R.; Kumar, M.; Nunes, S. P.; Schwingenschlogl, U.; Peinemann, K. V., Highways for Water Molecules: Interplay between Nanostructure and Water Vapor Transport in Block Copolymer Membranes. *J Membrane Sci* **2019,** *572*, 641-649.

171. Huang, F.; Largier, T. D.; Zheng, W. J.; Cornelius, C. J., Pentablock Copolymer Morphology Dependent Transport and Its Impact Upon Film Swelling, Proton Conductivity, Hydrogen Fuel Cell Operation, Vanadium Flow Battery Function, and Electroactive Actuator Performance. *J Membrane Sci* **2018,** *545*, 1-10.

172. Suzuki, A.; Sen, U.; Hattori, T.; Miura, R.; Nagumo, R.; Tsuboi, H.; Hatakeyama, N.; Endou, A.; Takaba, H.; Williams, M. C.; Miyamoto, A., Ionomer Content in the Catalyst Layer of Polymer Electrolyte Membrane Fuel Cell (Pemfc): Effects on Diffusion and Performance. *International Journal of Hydrogen Energy* **2011,** *36* (3), 2221-2229.

173. Nykaza, J.; Sharick, S.; Davis, E.; Ye, Y. s.; Page, K.; Jackson, A.; Beyer, F.; Winey, K.; Elabd, Y., Impact of Alkyl Chain Length on Ion Conduction and Morphology in Polymerized Ionic Liquid Diblock Copolymers. *Abstr Pap Am Chem S* **2015,** *249*.

174. Nykaza, J. R.; Ye, Y. S.; Elabd, Y. A., Polymerized Ionic Liquid Diblock Copolymers with Long Alkyl Side-Chain Length. *Polymer* **2014,** *55* (16), 3360-3369.

175. Nykaza, J. R.; Ye, Y. S.; Elabd, Y. A., Synthesis of Long Side-Chain Polymerized Ionic Liquid Diblock Copolymers with High Ion Conductivity. *Abstr Pap Am Chem S* **2014,** *247*.

176. Nykaza, J. R.; Ye, Y. S.; Nelson, R. L.; Jackson, A. C.; Beyer, F. L.; Davis, E. M.; Page, K.; Sharick, S.; Winey, K. I.; Elabd, Y. A., Polymerized Ionic Liquid Diblock Copolymers: Impact of Water/Ion Clustering on Ion Conductivity. *Soft Matter* **2016,** *12* (4), 1133-1144.

177. Price, S. C.; Ren, X. M.; Jackson, A. C.; Ye, Y. S.; Elabd, Y. A.; Beyer, F. L., Bicontinuous Alkaline Fuel Cell Membranes from Strongly Self-Segregating Block Copolymers. *Macromolecules* **2013,** *46* (18), 7332-7340.

178. Meek, K. M.; Nykaza, J. R.; Elabd, Y. A., Alkaline Chemical Stability and Ion Transport in Polymerized Ionic Liquids with Various Backbones and Cations. *Macromolecules* **2016,** *49* (9), 3382-3394.

179. Meek, K. M.; Sun, R.; Willis, C.; Elabd, Y. A., Hydroxide Conducting Polymerized Ionic Liquid Pentablock Terpolymer Anion Exchange Membranes with Methylpyrrolidinium Cations. *Polymer* **2018,** *134*, 221-226.

180. Ertem, S. P.; Caire, B. R.; Tsai, T. H.; Zeng, D.; Vandiver, M. A.; Kusoglu, A.; Seifert, S.; Hayward, R. C.; Weber, A. Z.; Herring, A. M.; Coughlin, E. B.; Liberatore, M. W., Ion Transport Properties of Mechanically Stable Symmetric Abcba Pentablock Copolymers with Quaternary Ammonium Functionalized Midblock. *J Polym Sci Pol Phys* **2017,** *55* (7), 612-622.

181. Meek, K. M.; Elabd, Y. A., Polymerized Ionic Liquid Block Copolymers for Electrochemical Energy. *J Mater Chem A* **2015,** *3* (48), 24187-24194.

182. Ye, Y. S.; Sharick, S.; Davis, E. M.; Winey, K. I.; Elabd, Y. A., High Hydroxide Conductivity in Polymerized Ionic Liquid Block Copolymers. *Acs Macro Lett* **2013,** *2* (7), 575-580.

183. Ponce-Gonzalez, J.; Whelligan, D. K.; Wang, L. Q.; Bance-Soualhi, R.; Wang, Y.; Peng, Y. Q.; Peng, H. Q.; Apperley, D. C.; Sarode, H. N.; Pandey, T. P.; Divekar, A. G.; Seifert, S.; Herring, A. M.; Zhuang, L.; Varcoe, J. R., High Performance Aliphatic-Heterocyclic Benzyl-Quaternary Ammonium Radiation-Grafted Anion-Exchange Membranes. *Energ Environ Sci* **2016,** *9* (12), 3724-3735.

184. Hwang, M.; Sun, R.; Willis, C.; Morgan, B.; Beyer, F. L.; Elabd, Y. A., Hydroxide Conducting Polymerized Ionic Liquid Pentablock Terpolymer Anion Exchange Membranes with Various Cations. **2018**.

185. Gu, F. L.; Dong, H. L.; Li, Y. Y.; Sun, Z.; Yan, F., Base Stable Pyrrolidinium Cations for Alkaline Anion Exchange Membrane Applications. *Macromolecules* **2014,** *47* (19), 6740-6747.

186. Reshetenko, T.; Odgaard, M.; Schlueter, D.; Serov, A., Analysis of Alkaline Exchange Membrane Fuel Cells Performance at Different Operating Conditions Using Dc and Ac Methods. *Journal of Power Sources* **2018,** *375*, 185-190.

187. Omasta, T. J.; Peng, X.; Lewis, C. A.; Varcoe, J. R.; Mustain, W. E., Improving Performance in Alkaline Membrane Fuel Cells through Enhanced Water Management. *Ecs Transactions* **2016,** *75* (14), 949-954.

188. Cooper, K. R.; Smith, M., Electrical Test Methods for on-Line Fuel Cell Ohmic Resistance Measurement. *Journal of Power Sources* **2006,** *160* (2), 1088-1095.

189. Omasta, T. J.; Wang, L.; Peng, X.; Lewis, C. A.; Varcoe, J. R.; Mustain, W. E., Importance of Balancing Membrane and Electrode Water in Anion Exchange Membrane Fuel Cells. *J Power Sources* **2018,** *375*, 205-213.

190. Gazdzicki, P.; Mitzel, J.; Dreizler, A. M.; Schulze, M.; Friedrich, K. A., Impact of Platinum Loading on Performance and Degradation of Polymer Electrolyte Fuel Cell Electrodes Studied in a Rainbow Stack. *Fuel Cells* **2018,** *18* (3), 270-278.

191. Microspray, Ultrasonic Vortex Nozzle. **2018**.

192. Ralph, T. R.; Hards, G. A.; Keating, J. E.; Campbell, S. A.; Wilkinson, D. P.; Davis, M.; StPierre, J.; Johnson, M. C., Low Cost Electrodes for Proton Exchange Membrane Fuel Cells - Performance in Single Cells and Ballard Stacks. *J Electrochem Soc* **1997,** *144* (11), 3845-3857.

193. Wilson, M. S.; Gottesfeld, S., High-Performance Catalyzed Membranes of Ultra-Low Pt Loadings for Polymer Electrolyte Fuel-Cells. *J Electrochem Soc* **1992,** *139* (2), L28-L30.

194. Saha, M. S.; Paul, D. K.; Malevich, D.; Peppley, B. A.; Karan, K., Preparation of Ultra-Thin Catalyst Layers by Piezo-Electric Printer for Pemfcs Applications. *Proton Exchange Membrane Fuel Cells 9* **2009,** *25* (1), 2049-2059.

195. Zeng, Y. C.; Shao, Z. G.; Zhang, H. J.; Wang, Z. Q.; Hong, S. J.; Yu, H. M.; Yi, B. L., Nanostructured Ultrathin Catalyst Layer Based on Open-Walled Ptco Bimetallic Nanotube Arrays for Proton Exchange Membrane Fuel Cells. *Nano Energy* **2017,** *34*, 344-355.

196. Omasta, T. J.; Zhang, Y. F.; Park, A. M.; Peng, X.; Pivovar, B.; Varcoe, J. R.; Mustain, W. E., Strategies for Reducing the Pgm Loading in High Power Aemfc Anodes. *J Electrochem Soc* **2018,** *165* (9), F710-F717.

197. Pan, J.; Chen, C.; Li, Y.; Wang, L.; Tan, L. S.; Li, G. W.; Tang, X.; Xiao, L.; Lu, J. T.; Zhuang, L., Constructing Ionic Highway in Alkaline Polymer Electrolytes. *Energ Environ Sci* **2014,** *7* (1), 354-360.

198. Pan, J.; Li, Y.; Han, J. J.; Li, G. W.; Tan, L. S.; Chen, C.; Lu, J. T.; Zhuang, L., A Strategy for Disentangling the Conductivity-Stability Dilemma in Alkaline Polymer Electrolytes. *Energ Environ Sci* **2013,** *6* (10), 2912-2915.

199. Zhu, L.; Pan, J.; Hickner, M., Multi-Cation Side Chain Anion-Exchange Membranes. *Abstr Pap Am Chem S* **2016,** *251*.

200. Zhu, L.; Yu, X. D.; Hickner, M. A., Exploring Backbone-Cation Alkyl Spacers for Multi-Cation Side Chain Anion Exchange Membranes. *J Power Sources* **2018,** *375*, 433-441.